Correlation Wavefront Sensing and Turbulence Profiling for Solar Adaptive Optics

MATTHEW JAMES TOWNSON

Correlation Wavefront Sensing and Turbulence Profiling for Solar Adaptive Optics

Matthew J. Townson

A thesis presented for the degree of

Doctor of Philosophy

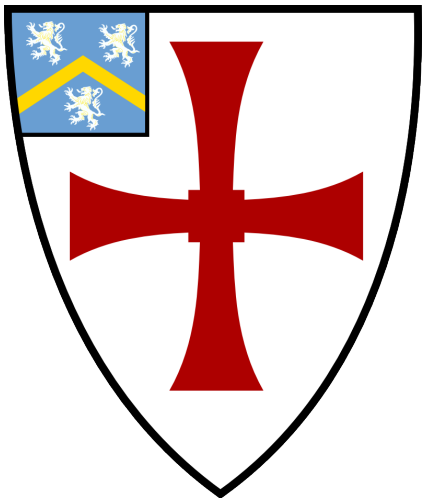

Centre for Advanced Instrumentation

The University of Durham

United Kingdom

March 2016

Correlation Wavefront Sensing and Turbulence Profiling for Solar Adaptive Optics

Matthew J. Townson

Abstract

Ground based telescopes suffer from degraded resolution due to aberrations induced by the atmosphere which prevent them from reaching the diffraction limit. Adaptive Optics (AO) is a technology which corrects for this effect in real-time, restoring the resolution of a telescope. However, it only corrects for a very narrow field of view (FOV) around the guide source. Tomographic AO uses multiple guide sources to increase the size of the corrected FOV, however, these forms of AO are affected by the vertical distribution of turbulence in the atmosphere (turbulence profile). This thesis presents work to develop turbulence profiling instruments for daytime astronomy and improve centroiding techniques for correlating wavefront sensors (WFS) which are used in slope based turbulence profiling instruments.

The development of centroiding techniques for use on extended objects is based on cross-correlation techniques. Two methods are presented, one for optimising centroiding parameters on cross-correlation images and another for improving the signal to noise in cross-correlation images created from images with large relative shifts by using supersized reference images. Choosing optimal centroiding parameters for correlating WFSs is demonstrated in simulation, optimising a windowed, thresholded center of mass. The creation and use of supersized reference images is also demonstrated in simulation, where they are created from WFS data and shown to drastically improve the accuracy of centroiding for centroiding extended objects which have continuous structure across the whole field.

So-SLODAR (solar-slope detection and ranging) was developed as a slope based instrument for measuring the turbulence profile on the Swedish Solar Telescope (SST), La Palma. The technique is based on SLODAR, with developments to take advantage of the continuous structure of the solar surface offering multiple guide sources. A full description of the technique and its data reduction is presented, along with the first results from on-sky tests on the SST.

Supervisors: Dr. Christopher Saunter and Prof. Gordon D. Love

Acknowledgements

Initially I would like to thank my supervisors, Gordon Love and Christopher Saunter, as well as Aglaè Kellerer, Tim Butterley and Richard Wilson. Their help, advice and insights helped enormously and guided me through my PhD. I am also grateful for the financial support from the Science and Technology Faclilites Council.

I would like to thank Göran Scharmer and Pit Sutterlin for allowing me to use the SST. They also helped out hugely during my trips to La Palma in fun, advice and logistics, without them I would have been completely unable to test So-SLODAR on-sky. During my time in La Palma Tim Morris, James Osborn and Tim Butterley have also been a great help. They also were more than happy to provide whisky and beer, which I suspect did not help so much.

My general interest in science and technology has continued to grow thanks to everyone in CfAI. I have had an incredibly fun three and a half years thanks to the friendly atmosphere they have created. On a day to day basis constant encouragement, advice and procrastination have been provided by my office mates, the main offenders being Scott Silburn, Tom Mitchell, Saavi Perera and Dora Föhring. During the write-up my sanity has been preserved by Fiona Nì Chionnaoith, James Osborn and Andrew Reeves, for which I am extremely grateful.

I would also like to thank the continuous support of my parents and sister, for as long as I can remember they have encouraged me to pursue my interests. Last but not least, I would like to thank Charlotte for sticking with me through these last few years. She has always been there with tea and a freshly baked cake to take my mind off things.

Contents

Declaration

The work in this thesis is based on research carried out at the Centre for Advanced Instrumentation, Department of Physics, University of Durham, England. No part of this thesis has been submitted elsewhere for any other degree or qualification, and it is the sole work of the author unless referenced to the contrary in the text.

Some of the work presented in this thesis has been published in journals and conference proceedings - the relevant publications are listed below.

Publications

M. J. Townson, C. D. Saunter, and A. Kellerer, "Improved shift estimates on extended Shack-Hartmann wavefront sensor images," *Monthly Notices of the Royal Astronomical Society.* 7(April), 1–7 (2015).

M. J. Townson, A. Kellerer, J. Osborn, T. Butterley, T. Morris, and R. W. Wilson, "Daytime site characterisation of La Palma, and its relation to night-time conditions," In *Proceedings of SPIE* 9147, 91473E (2014).

M. J. Townson, A. Kellerer, J. Osborn, T. Butterley, T. Morris, and R. W. Wilson, "Characterising daytime atmospheric conditions on La Palma," In *Journal of Physics: Conference Series* 595, 012035 (2015).

List of Figures

List of Tables

Nomenclature

AO adaptive optics

CCD charge-coupled device

DIMM differential image motion monitor

DKIST Daniel K. Inouye Solar Telescope

DST Dunn solar telescope

ELT extremely large telescopes

E-ELT European extremely large telescope

EST european solar telescope

FFT fast fourier transform

FFTW fastest fourier transform in the west

FOV field of view

LGS laser guide star

MASP multiple aperture seeing profiler

MASS multi-aperture scintillation sensor

MCAO multi-conjugate adaptive optics

MOAO multi-object adaptive optics

NSO national solar observatory

PSD power spectral density

PSF point spread function

S-DIMM+ solar-differential image motion monitor +

SCAO single conjugate adaptive optics

SCIDAR scintillation detection and ranging

SH-WFS Shack-Hartmann wavefront sensor

SHABAR shadow band ranger

SLODAR slope detection and ranging

So-SLODAR solar slope detection and ranging

SNR signal to noise ratios

SST swedish solar telescope

WFS wavefront sensor

WF-WFS wide-field wavefront sensor

Chapter 1

Introduction

1.1 Adaptive Optics Overview

1.1.1 Brief History of Astronomy

The main problem facing astronomers is the extreme distances between them and the objects they measure. This manifests itself as making the objects appear both very faint and very small. It is the job of the telescope to remove these problems, allowing these dim objects to be observed in detail at high resolution.

The first telescopes enabled astronomers to observe objects at higher resolution than with the naked eye. This allowed, amongst others, the observation of the structure on the surface of the Sun, leading to the confirmation of the rotation of the Sun by Galilei (1632). As technology developed the eye became a redundant observing instrument, being replaced initially by photographic plates before reaching the current standard of electronic charge-coupled device (CCD) detectors (Karttunen et al., 2007). These developments allowed for much fainter objects to be observed, as exposure times could be increased to collect more photons. CCDs have also become extremely sensitive (Howell, 2006), allowing them to detect individual photons, with minimal noise.

As telescopes increased in size to accommodate the requirements of astronomers

supporting technologies also developed. However, large telescopes are unable to reach their diffraction limit due to the effects the atmosphere on light passing through it. This has been known since the 18^{th} century, with Newton (1730) talking of the "confusion of the Rays which arises from the Tremors of the atmosphere".

One solution to this problem is to place the telescope outside the atmosphere by placing it in space. In orbit above the atmosphere space telescopes can reach resolution which is unattainable on Earth, with the most notable example being the Hubble Space Telescope (Trauger et al., 1994). However, there are serious disadvantages to placing a telescope in orbit. These include the cost of placing the telescope in orbit and the inability to easily modify or change instruments or elements on the telescope.

1.1.2 Adaptive Optics

In recent times advances in technology have allowed for systems which can correct for the effects of the atmosphere in real-time, adaptive optics (AO), allowing near diffraction-limited capabilities for ground based telescopes which employ these methods. The concept of correcting for the aberrations induced by the atmosphere was first introduced by Babcock (1953), where a layer of oil could be manipulated on a mirror for the "correction of seeing". However it wasn't until Hardy et al. (1977) that this was realised with the first AO system capable of correcting for atmospheric turbulence in real-time. An example of an aberrated point spread function (PSF) shown alongside a corrected PSF taken from Hardy et al. (1977) is given in Fig. 1.1.

The atmosphere is a continuously evolving entity, in order to correct for it continuously the corrections applied need to be continuously updated. This mandates the use of a bright light source to act as a reference from which the aberrations induced by the atmosphere can be measured. As the changes are continuous a system to correct for it can benefit from operating in closed-loop, where only the changes in

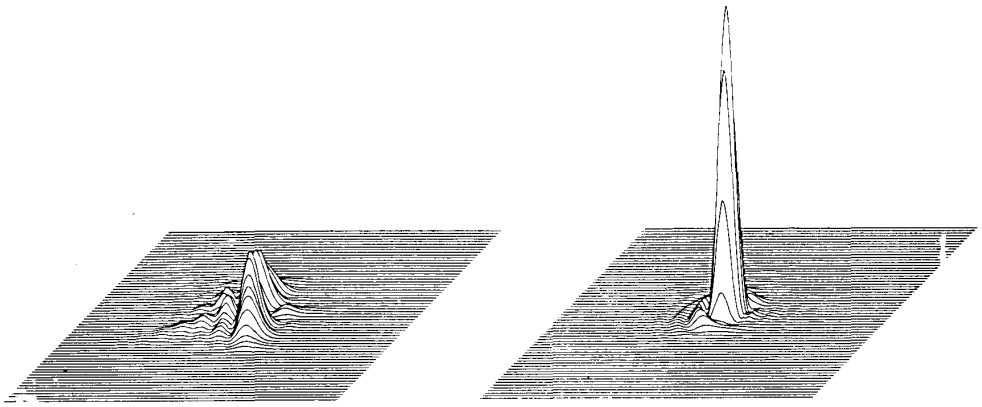

Figure 1.1: Example aberrated wavefront (left) and AO corrected wavefront (right) taken from Hardy et al. (1977). These images are of a He-Ne laser source after passing through static turbulence.

aberrations are measured and the correction adjusted accordingly. A schematic of a typical closed-loop AO system is given in Fig. 1.2.

Traditional AO relies on a bright source in order to sense the aberrations with a WFS. For a Shack-Hartmann wavefront sensor (SH-WFS) this is done by splitting the telescope pupil into sub-pupils which measure the gradient of local turbulence. Short exposure times are required, as the whole system is required to update in the range of 100-1000Hz in order to maintain the correction with the changes in the turbulence. The requirement for a bright guide star limits the regions of the sky that are accessible for AO corrected astronomy. This has been overcome to a certain extent with the development of LGS, where a laser beacon is launched and used as the guide source for wavefront sensing. This was first developed by J. Feinlieb and R. Hunter independently (Benedict et al., 1994) and has brought nearly all-sky coverage for AO systems which employ LGS, with these systems being used consistently in many observatories, such as Gemini (Neichel et al., 2014).

With the development of more complex AO techniques which use tomography, such as multi-conjugate adaptive optics (MCAO) and multi-object adaptive optics (MOAO), the vertical distribution of atmospheric turbulence has become important, as the total integrated strength of the turbulence alone doesn't provide

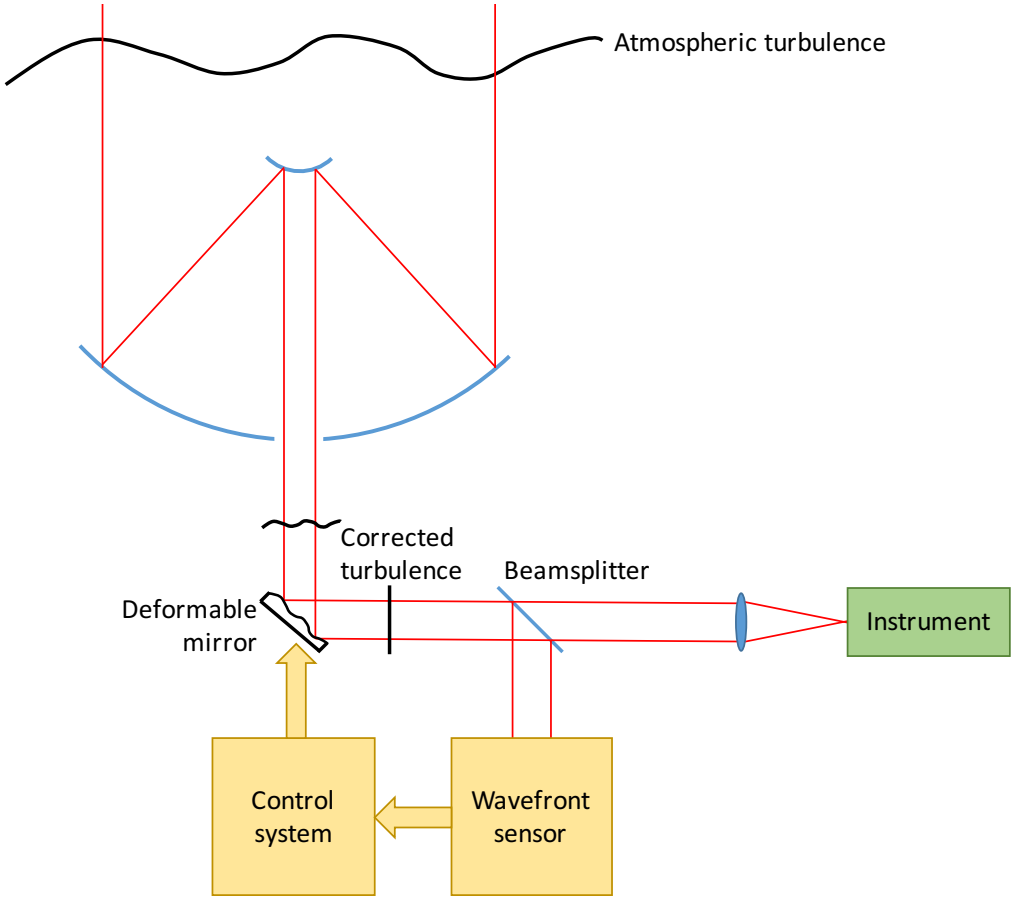

Figure 1.2: Cartoon of a closed-loop AO system. Aberrated wavefronts incident to the telescope are corrected with a deformable mirror before passing through to the science instrument and WFS. The WFS measures the residual of the turbulence after correction, then feeds back this to the control system, where the deformable mirror's shape is updated. This enables the long exposure on the science image to maintain near diffraction-limited performance.

enough information to operate these systems. For the European extremely large telescope (E-ELT) the turbulence profile is important as many of the proposed instruments use these types of AO correction, including EAGLE (Cuby et al., 2010) and MAORY (Diolaiti, 2010).

These systems require the use of multiple LGSs in order to perform tomography. Some of the images on the LGS WFSs will show elongated images of the laser plume, but the slopes from these sub-apertures are required in order to estimate the volume of turbulence properly. There has been much work on the subject of how to best estimate the slopes using an elongated LGS image, including work by

Thomas et al. (2008a, 2010), but there is currently no system which observes LGS with the elongations expected on the edge of the E-ELT pupil on-sky. The next phase of the CANARY experiment is designed to observe LGS at these extreme elongations (Rousset et al., 2014) and test techniques for wavefront sensing and the general operation of AO systems with highly elongated laser spots.

1.1.3 Solar Adaptive Optics

AO is also used in many solar telescopes and follows similar designs to their night-time counterparts. However, they face challenges which are not experienced in night-time AO (Rimmele, 2004). The main difficulties solar AO faces are the typically poor day-time seeing conditions, the preferred observation wavelengths (visible, often down to the blue) and the WFS. Solar WFSs observe some part of the solar surface, so are required to work on low contrast, extended, time-varying objects.

The first solar AO experiments were performed on the Dunn solar telescope (DST) by Hardy (1980) using a shearing interferometer. SH-WFS were first used in solar AO by Acton and Smithson (1992) on the DST. The next breakthrough in solar WFS was the development of the correlating SH-WFS, with it first being demonstrated by the national solar observatory (NSO) and is described in Rimmele and Radick (1998a). This allowed solar granulation to be used in the WFS where previously small, high contrast regions were required for centroiding in WFSs for simple centroiding techniques to work.

A major limitation in solar AO is that single conjugate adaptive optics (SCAO) can only correct the aberrations within the isoplanatic patch of the order of a few arcseconds (Beckers, 1988). Typically sunspots or other active regions of the Sun extend over $1-2'$ and ideally a solar AO system would correct over the whole field. To achieve this many solar telescopes propose using MCAO systems to acieve this correction, such as the MCAO system at the DST (Rimmele et al., 2010). Solar

MCAO systems tend to follow similar architectures, a high order WFS which is used to measure the ground layer of turbulence and a lower order WFS with a large field of view (FOV) for tomography.

Future large solar telescopes, such as the Daniel K. Inouye Solar Telescope (DKIST) (Elmore et al., 2014) and the european solar telescope (EST) (Collados et al., 2010) are likely to operate with MCAO. Like night-time tomographic AO, the performance of these systems will depend greatly on the turbulence profile.

1.2 Profiling Atmospheric Turbulence

As has been mentioned previously, the turbulence profile effects the performance of tomographic AO systems. The turbulence profile is an important factor for the functioning of wide-field AO, such as MCAO and MOAO (Fusco and Costille, 2010). The turbulence profile is also important for site-characterisation for telescopes operating in both the day-time and night-time. The design of MCAO systems requires knowledge of the turbulence profile (Rigaut et al., 2000) and site-characterisation with a profiling instrument enables the optimal conjugate heights for the deformable mirrors to be chosen for MCAO. The turbulence profile, as measured with a profiling instrument, can also be used to optimise an AO system to improve the tomographic performance, as demonstrated by CANARY (Vidal et al., 2010).

There are many methods for measuring the turbulence profile at night, including slope detection and ranging (SLODAR) (Wilson, 2002), scintillation detection and ranging (SCIDAR) (Rocca et al., 1974) and multi-aperture scintillation sensor (MASS) (Kornilov et al., 2003; Tokovinin and Kornilov, 2007). SLODAR and SCIDAR are triangulation techniques which require multiple sources, SLODAR measures the correlation between the gradient of the wavefront across a pupil for two sources and SCIDAR measures the correlation between scintillation images. MASS probes the spatial structure of scintillation of a single star through ob-

serving concentric rings of a pupil image. These techniques have been further developed by instruments such as Surface-Layer SLODAR (Masciadri et al., 2010) and Stereo-SCIDAR (Shepherd et al., 2014).

For day-time turbulence profiling there are fewer instruments available. There are slope based, solar-differential image motion monitor + (S-DIMM+) (Scharmer and van Werkhoven, 2010), and scintillation based, shadow band ranger (SHABAR) (Beckers, 2001), turbulence profilers, both of which offer low resolution measurements of the turbulence profiles. S-DIMM+ is capable of resolving 10 different altitudes up to 30km and SHABAR can resolve the turbulence close to the ground, but is unable to resolve high altitude turbulence.

1.3 Thesis Motivation and Synopsis

High resolution turbulence profiles during the day are required for the development of advanced tomographic AO systems for solar telescopes. Measurements from these instruments can shape the design of the AO systems for future solar telescopes and potentially be used in tandem with AO systems, as has been demonstrated for night-time astronomy.

The solar slope detection and ranging (So-SLODAR) instrument measures the gradient of the phase across a telescope pupil using a wide-field SH-WFS. Like S-DIMM+, So-SLODAR operates in open-loop, so the shifts of the sub-aperture field measured are larger than in closed-loop AO systems. In order to perform these centroiding measurements on an extended source cross-correlation and centroiding algorithms are required. Noise on these measurements propagate into noise in the measured turbulence profile, making accurate centroids important for profiling instruments.

In this thesis I describe a wavefront gradient based method for measuring the turbulence profile during the day, So-SLODAR, based on SLODAR, and methods for improving the centroids measured from wide-field WFS measurements. A descrip-

tion of how SH-WFSs operate, along with WF-WFSs is given in chapter 2 with descriptions of how noise propagates through a correlating WFS to centroid measurements. The statistics and measurements of atmospheric turbulence are given in chapter 3 where the SLODAR technique is also explained. I describe a method for estimating optimal center of mass parameters for a correlating WFS in chapter 4. In chapter 5 I describe a technique for increasing the FOV of the reference image for correlating WFS in order to improve the centroid estimates for open-loop WFSs. I present the So-SLODAR method in chapter 6, including the data reduction technqiue, how it differs from the SLODAR technique and present the first measured turbulence profiles using the instrument on the swedish solar telescope (SST) on La Palma. Finally in chapter 7 I summarise the results of the improvements to centroiding techniques for correlating WFS and the first results from So-SLODAR.

Chapter 2

Shack-Hartmann Wavefront Sensing Theory

WFSs are required in AO systems to sense the wavefront aberrations incident to the telescope. They are an area of active research, with many different types available , including the Pyramid WFS (Ragazzoni, 1996), curvature WFS (Roddier and Roddier, 1988), and the SH-WFS (Shack and Platt, 1971). Each of these different WFSs have their own set of advantages and disadvantages. In this thesis I concentrate on the SH-WFS, as this is the most commonly employed in both solar and LGS WFSs, being used in SPHERE (Fusco et al., 2006) and planned for use in EAGLE (Cuby et al., 2008) and EPICS (Kasper et al., 2008). In this chapter I describe how a SH-WFS can be used to measure wavefronts using extended sources, specifically solar granulation and elongated LGSs, using a WF-WFS and cross-correlation techniques.

2.1 Shack-Hartmann Wavefront Sensor

The SH-WFS works by measuring the gradient of the wavefront in different locations across a pupil plane. In order to do this a lenslet array is placed in the pupil plane, effectively splitting it up into many separate sub-pupils. The motion of the

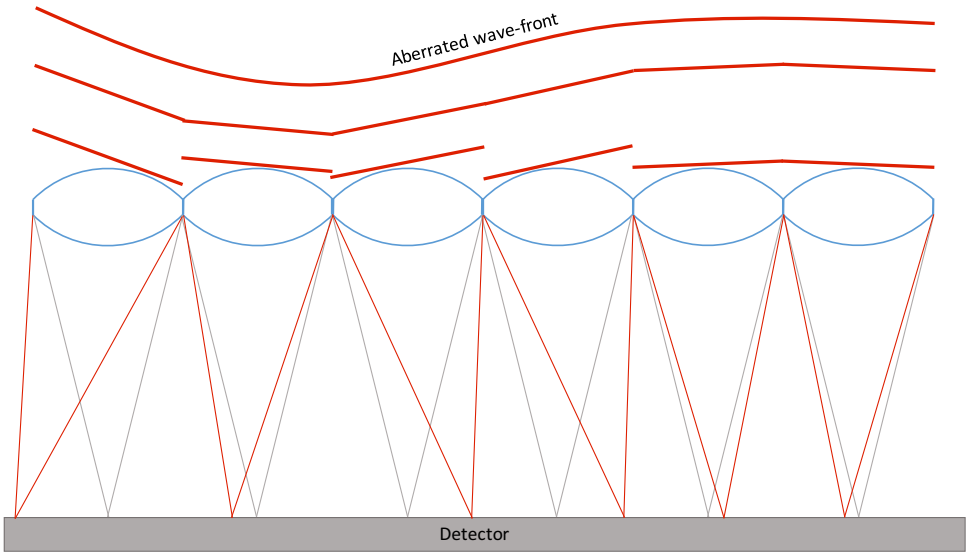

Figure 2.1: One dimensional cut-through of a SH-WFS. The Incident wavefront is sectioned by the lenslets (shown in blue). Their gradients then move the location of the image formed from the on-axis position (shown in grey), to a new position (shown in red). The displacement of the images is proportional to the gradient of the wavefront incident to the lenslet.

spots formed on the detector by each of these lenslets can then be measured, and is proportional to the gradient of the wavefront incident on them. A one dimensional cartoon of a SH-WFS is shown in Fig. 2.1. The location of the images formed by each lenslet is measured, then the displacement from the positions for a flat wavefront calculated. This displacement can be converted back into the wavefront gradient for each sub-aperture using the pixel scale. From here an estimate of the incident wavefront can be reconstructed, then corrected in a full AO system.

A similar design of SH-WFS is used in most solar AO systems. However, there are no point sources available to observe during the day, so instead granular features on the photosphere are observed. This causes images to be formed on the detector rather than spots, so more pixels are used in each sub-aperture and a field-stop is used to stop the different sub-apertures from overlapping on the detector. These images move in the same way as spots from a point source, so if their motion is tracked the shifts can be used in the same way as the positions of spots to measure the gradient on the incident wavefront. However, the method for measuring the

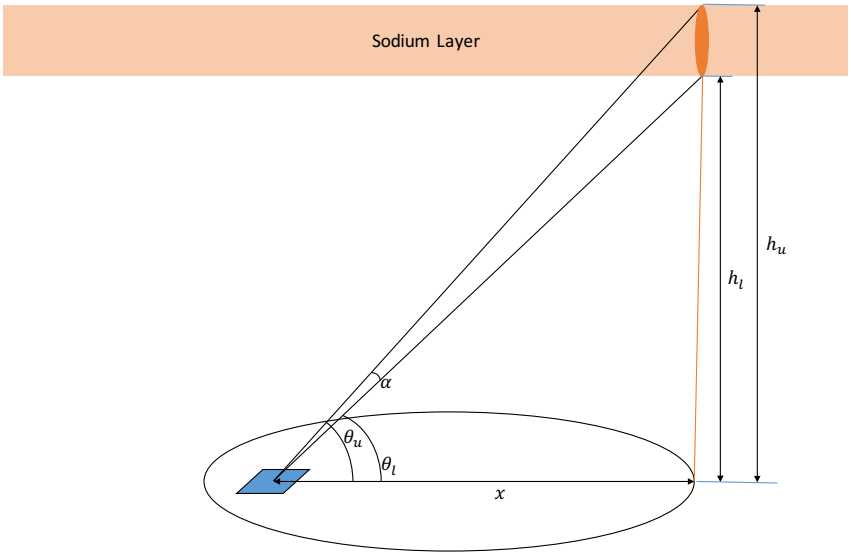

Figure 2.2: One dimensional cartoon showing the formation of an elongated LGS spot on a sub-aperture. In this example the laser (shown in orange) is launched from the side of the telescope pupil, and illuminates a plume in the sodium layer of the atmosphere between h_l and h_u. A single sub-aperture is highlighted in blue. The elongation for the sub-aperture, α, can be calculated using the position of the sub-aperture in the pupil, and the height of the laser plume in the Sodium layer (h_u and h_l).

displacements of the images requires more complex centroiding techniques.

2.1.1 Laser Guide Star Elongation

For extremely large telescopes (ELT), which use LGS, the images of the LGS in the sub-apertures of the WFS will appear extended instead of spot like. This elongation of the LGS spot is due to the laser illuminating a plume in the extended layer of sodium atoms in the mesosphere (typically $80 - 105$km) (Pfrommer and Hickson, 2014). When viewing this plume off-axis an elongated spot image is formed on the detector. This is illustrated in one dimension in Fig. 2.2. From this diagram the elongation, α, seen by the sub-aperture can be found using;

$$\alpha = \theta_u - \theta_l \tag{2.1}$$

where θ_u is the angle from the telescope pupil to the upper limit of the sodium plume, h_u, and θ_l is the angle from the telescope pupil to the lower limit of the

Sodium plume, h_l. These θ values can be calculated using;

$$\begin{aligned} \theta_u &= \arctan\left(\frac{h_u}{x}\right) \\ \theta_l &= \arctan\left(\frac{h_l}{x}\right), \end{aligned} \tag{2.2}$$

and can be substituted back into equation 2.1, which becomes;

$$\alpha = \arctan\left(\frac{h_u}{x}\right) - \arctan\left(\frac{h_l}{x}\right). \tag{2.3}$$

If we take a simplified E-ELT, where the laser is launched from the edge of the telescope pupil, the elongation of the LGS on the WFS varies dramatically. The sub-apertures next to the laser launch site observe very little elongation and the opposite side of the pupil observes the maximal elongation seen on the WFS. Using a typical sodium profile, as measured by Pfrommer and Hickson (2014), we get measured values of $h_u = 100$km and $h_l = 85$km. Using a value of $x = 39$m (McPherson et al., 2012), for the most elongated sub-aperture on an E-ELT the elongation measured will be $\sim 15''$.

On top of this effect the orientation of the plume on the WFS detector will be different for each sub-aperture, due to the projection of the laser in two dimensions. To calculate this elongation along the x and y dimensions can be treated separately using equation 2.3, and a vector, $\boldsymbol{\theta}_e$, created;

$$\boldsymbol{\theta}_e = \begin{bmatrix} \theta_x \\ \theta_y \end{bmatrix}, \tag{2.4}$$

where θ_x and θ_y are the x and y components of the elongation respectively, calculated separately with equation 2.3. This geometry is shown in Fig. 2.3, with a cartoon of a single, elongated, sub-aperture image in a WFS given in Fig. 2.4.

The vector, $\boldsymbol{\theta}_e$ can be converted into a size and angle using;

$$\begin{aligned} |\boldsymbol{\theta}_e| &= \sqrt{\theta_x^2 + \theta_y^2} \\ \theta &= \arctan\left(\frac{\theta_y}{\theta_x}\right). \end{aligned} \tag{2.5}$$

where $|\boldsymbol{\theta}_e|$ is the elongation size and θ is the rotation angle of the laser plume (as shown in Fig. 2.4). Combining this with data from Pfrommer and Hickson (2014)

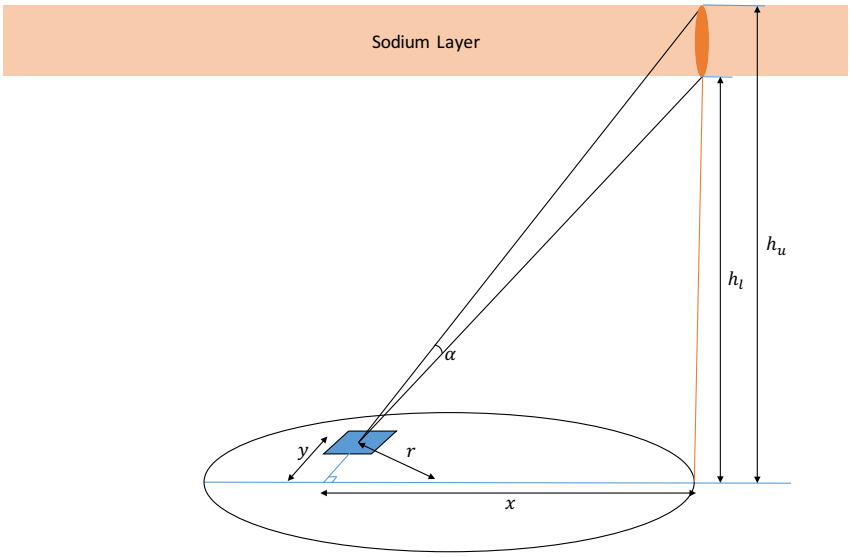

Figure 2.3: Cartoon showing the formation of an elongated laser spot to two dimensions. If the elongation is split into x and y dimensions, a vector $\boldsymbol{\theta}_e$ can be calculated using equation 2.3 for each dimension independently. This gives the elongation, and orientation, seen by a sub-aperture in a WFS in any location on the telescope pupil, as shown in Fig. 2.4.

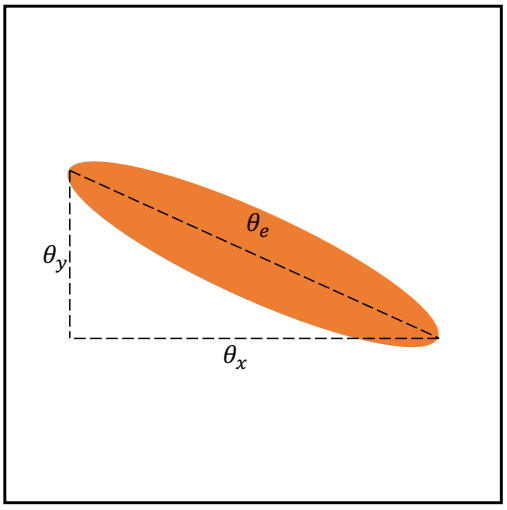

Figure 2.4: Cartoon of the image in a WFS for a single sub-aperture observing an elongated LGS. The laser plume is elongated in an arbitrary direction, which can be calculated from the elongation if the x and y dimensions, θ_x and θ_y respectively.

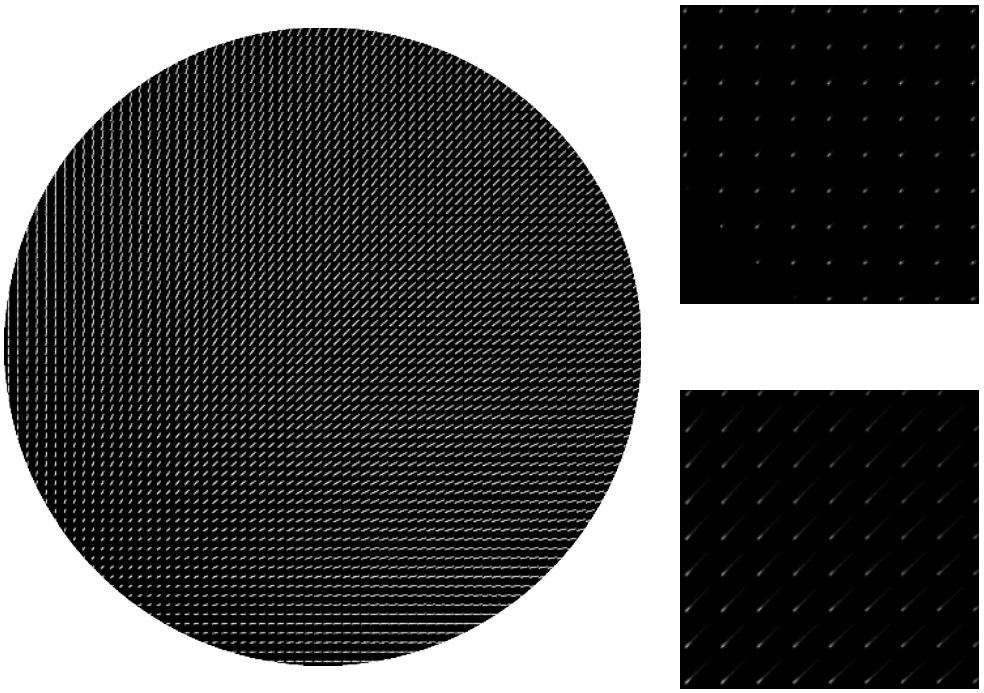

Figure 2.5: Simulated LGS WFS image for the E-ELT with no noise or turbulence. The upper right section shows the lest elongated part of the WFS, and the lower right section shows the most elongated part of the WFS. The full WFS image is shown on a log scale to make the elongated sub-apertures easier to see.

it is possible to create simulated WFS frames for the E-ELT, for a given sodium profile. A simulated LGS WFS frame for an ELT is shown in Fig. 2.5, for no atmospheric turbulence. These "perfect" WFS images can then be perturbed with the effects of atmospheric turbulence and different levels of noise added to create realistic WFS images expected for the LGS WFS on the E-ELT.

2.1.2 Solar Granulation

WFSs on solar telescopes require a large FOV to capture enough solar structure to allow reliable image shift measurements. Solar WFSs typically observe the solar granulation in the photosphere (Michau et al., 1993), which are visible around 500nm and use small small bandwidth, less than 10nm, to reduce chromatic effects. For SCAO the FOV used is $\sim 5 - 10$arcseconds (Soltau et al., 2013; Rimmele

and Radick, 1998b; Rimmele and Marino, 2011). This is a compromise between including as much structure as possible, for reliable image shift measurements, and minimizing the effect of averaging the wavefront information (Lühe, 1983).

High resolution, processed, images of solar granules are readily available *e.g.* Carlsson et al. (2003). For this thesis simulations of solar WFS use one such high resolution image, taken from Carlsson et al. (2003). This chosen image was taken at 430.5nm, by Mats Carlsson, Viggo Hansteen, Luc Rouppe van der Voort, Astrid Fossum, and Elin Marthinussen, with the image processing performed by Mats Löfdahl. It has a pixel scale of $0.04''$/pixel. The full resolution image, along with one which has been resampled to the resolution and FOV typical of a solar WFS ($0.4''$/pixel) is shown in Fig. 2.6. The contrast seen in Fig. 2.6 is representative of solar granulation used in solar AO ($\sim 10\%$).

2.2 Centroiding Extended Objects

In solar AO the only available source for WFSs is the sun itself. This poses a problem in that the solar disk is an extended object, which is continuous and has a low contrast value ($\sim 10\%$). This problem has been overcome to some degree, with a number of different solar AO systems currently in operation (Scharmer et al., 2003; Rimmele and Radick, 1998b; Michau et al., 1993). These instruments all use some form of Shack-Hartmann WFS (Shack and Platt, 1971) with a large FOV, to image a region of granules on the solar surface. The images of the granules are then correlated with a reference image, which is typically taken to be one of the sub-aperture images from the WFS frame. The generated cross-correlation images then need to be centroided in order to determine the relative shifts of the sub-apertures with respect to the reference image. For solar AO the global tip/tilt term is typically not measured by the WFS, so is removed from the WFS measurement, giving relative shifts of all of the sub-apertures, including the one used as the reference image.

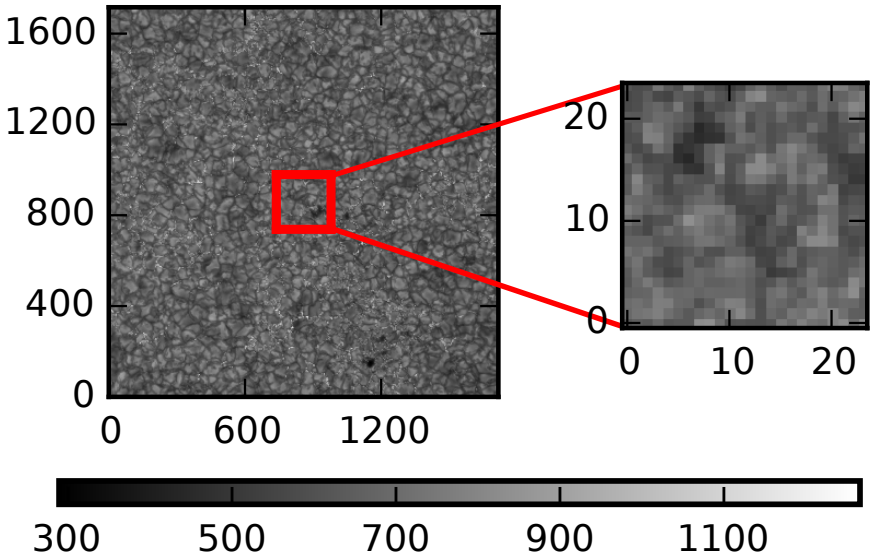

Figure 2.6: Image of solar granulation used as the input image in simulations for this thesis. The full image is $75 \times 75''$. This image is re-sampled and windowed to simulate images of solar WFS, with an example shown on the right. It has been re-sampled from the original resolution of $0.04''$/pixel to $0.4''$/pixel. The high resolution, full image was obtained from the SST on-line Gallery (Carlsson et al., 2003).

The location of the peak of a cross-correlation image is usually performed in a two-step process (Michau et al., 2006). Initially an integer shift measurement is performed by locating the region of peak intensity in the cross-correlation image and secondly the sub-pixel shift is estimated. The determination of the peak location to sub-pixel accuracy limits the accuracy to which the shift measurement can be performed, assuming the correct part of the cross-correlation image has been selected. Alternative approaches exist, such as simply performing a center of mass measurement on the entire cross-correlation image, to more complicated fitting, such as matched-filter (Gilles and Ellerbroek, 2006). However the accuracy of the resultant centroid position depends greatly on the parameters chosen for the centroiding algorithm and cannot be predicted.

2.2.1 Cross Correlation Image Generation

There are a number of methods for generating cross-correlation images between sub-aperture images. These have been compared many times, and a synopsis of the most popular methods is given by Löfdahl (2010). Here I give an outline of these methods, all descriptions follow a similar nomenclature with the misalignment between images being described with i and j for the x and y directions respectively. This means that i and j also represent the pixel locations in the cross-correlation image, with the origin at the center of the cross-correlation image. The methods are described for each pixel in the cross-correlation image, i, j.

2.2.1.1 Square Difference Function

The square difference function is simply calculated for each pixel, i, j, using;

$$\sum_{x,y}(Im(x,y) - Ref(x+i, y+j))^2, \tag{2.6}$$

where Im represents the sub-aperture image, and Ref represents the reference image. It corresponds to a least squares exploration of the possible alignments of the two images. If we expand out the squared term;

$$\sum_{x,y}(Im^2(x,y) + Ref^2(x+i, y+j) - 2Im(x,y)Ref(x+i, y+j)), \tag{2.7}$$

we get three terms, two corresponding to the square of the intensity in the two images, and the cross term between the two images. The cross term contains the information on the displacement between the images, and forms the basis of the covariance function, calculated in the image domain, used by the Dunn Telescope (Rimmele and Radick, 1998b).

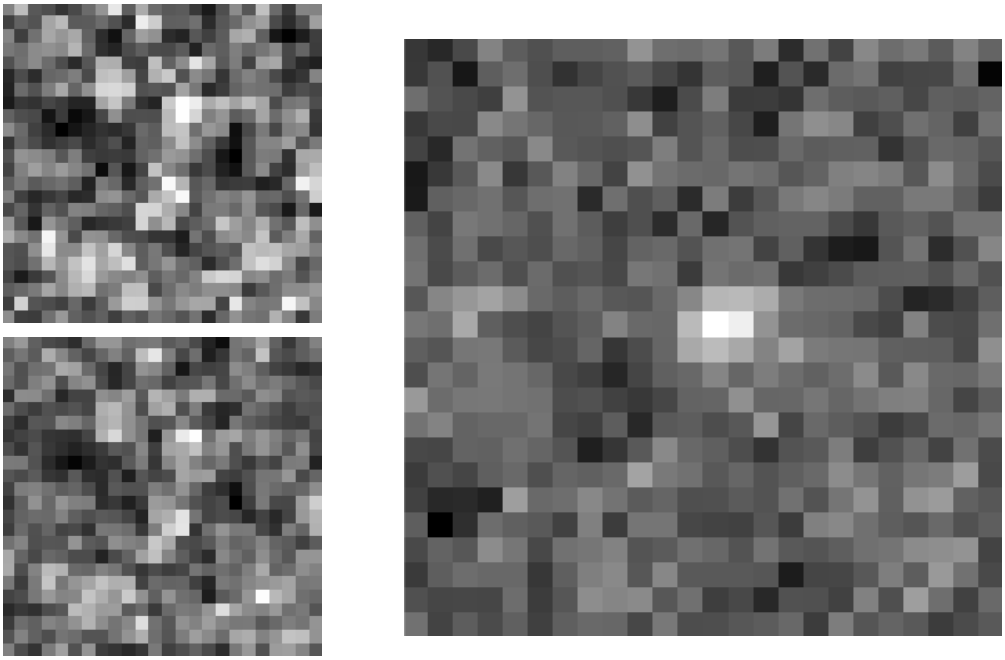

Figure 2.7: Example solar sub-aperture images, with their cross-correlation image. The left side shows two simulated sub-aperture images from a WFS observing solar granulation. The image on the right shows the cross-correlation image generated using the covariance function on the two images. The peak of the cross-correlation image is visible, as is the noise, which arises from the noise on the sub-aperture images.

2.2.1.2 Covariance Function

This method of generating the covariance function uses the Fourier transform to generate the cross-correlation image, as proposed by Lühe (1983).

$$\mathscr{F}^{-1}\left\{\mathscr{F}\{Im(x,y)\}.\mathscr{F}^{*}\{Ref(x,y)\}\right\}, \tag{2.8}$$

where $\mathscr{F}$ represents a Fourier transform. These calculations can be performed quickly with the use of Fast Fourier Transforms (Frigo and Johnson, 2001), and the fastest fourier transform in the west (FFTW) (Frigo, 1999), so are simple to implement. For these reasons this method was selected for the generation of cross-correlation images in this thesis. An example of two sub-aperture images of solar granulation with noise and the cross-correlation image generated from them using this technique is shown in Fig. 2.7.

2.2.1.3 Absolute Difference Function

This algorithm can be very fast, as it can be implemented efficiently in many CPU architectures, especially for 8-bit data (Keller et al., 2003). It is similar to the square difference function described previously (§2.2.1.1), with the modification of taking the absolute value of the difference rather than the squares;

$$\sum_{x,y} |Im(x,y) - Ref(s+i, y+j)|. \tag{2.9}$$

This method was developed further by Scharmer et al. (2000) in order to perform better with quadratic fitting around the correlation peak, described in §2.2.2.3, creating the "absolute difference function, squared";

$$\left(\sum_{x,y} |Im(x,y) - Ref(x+i, y+j)| \right)^2, \tag{2.10}$$

and is in use on the SST (Scharmer et al., 2003).

2.2.2 Centroiding Cross-Correlation Images

The position of the peak of a cross-correlation image from the center gives the shift between the sub-aperture and the reference image. Standard centroiding techniques can be used to measure the location of the correlation peak to sub-pixel accuracy. For point sources and the resultant Airy functions they produce on WFSs there are analytical methods to determine optimal parameters for peak location, at a given SNR (Pan et al., 2008). However, no such analytical treatment exists for images of arbitrary content, such as cross-correlation images.

There are a number of different methods for measuring the location of the peak in cross-correlation images, with the most commonly employed ones described below. The centroid vector is defined as;

$$\mathbf{R}^{i,ref} = \begin{bmatrix} x_0 \\ y_0 \end{bmatrix}, \tag{2.11}$$

where $\mathbf{R}^{i,ref}$ is the vector representing the shift between sub-aperture image, i, and the reference image, ref, with x_0 and y_0 corresponding to the x and y components of the centroid respectively.

2.2.2.1 Center of Mass

A simple method to determine the location of the peak of the cross-correlation image is to use a center of mass such as the one described by Stone (1989);

$$\mathbf{R}^{i,ref} = \frac{1}{I} \sum_{y=1}^{y_{\max}} \sum_{x=1}^{x_{\max}} C_{x,y} \mathbf{r}_{x,y}^{i,ref}, \tag{2.12}$$

where I represents the total intensity in the cross-correlation image, $C_{x,y}$ represents the intensity in pixel x, y in the cross-correlation image and $\mathbf{r}_{x,y}^{i,ref}$ is the vector between pixel x, y and the center of the cross-correlation image. This method allows for a sub-pixel estimation of the location of the cross-correlation image, but is susceptible to noise in the cross-correlation image.

2.2.2.2 Windowed, Thresholded Center of Mass

The simple center of mass measurement utilises all of the information in the cross-correlation image, including the noise from the two input images. This is not necessarily the best case, as outside of the peak of the cross-correlation pixels only introduce noise into the center of mass measurement. The contribution of these pixels can be removed by placing a window around the cross-correlation peak, and by using a threshold level to remove the contribution of pixels which aren't contributing to the cross-correlation peak. One method of performing a windowed, thresholded center of mass is described here.

Initially the cross-correlation image, C, has its background removed by subtracting the minimal value, $C_{\min}$, from all pixels, forming C_0;

$$C_0 = C - C_{\min}. \tag{2.13}$$

A threshold value can then be calculated using;

$$I_{thresh} = C_{0,\max} \times \alpha, \qquad 0 \leq \alpha \leq 1. \tag{2.14}$$

I_{thresh} is the threshold intensity, $C_{0,\max}$ is the maximum intensity in the background subtracted correlation image C_0, and α is the threshold value. When $\alpha = 0$ all data in the cross-correlation image is retained, and when $\alpha = 1$ only the brightest pixel is retained. The threshold is applied to C_0 by setting all pixel values where $C_{i,j} < I_{\text{thresh}}$ to the background value, 0. This creates the thresholded cross-correlation image, C_{thresh}.

The threshold intensity, I_{thresh}, is calculated for each cross-correlation image, so it is sympathetic to the magnitude of the cross-correlation peak. This ensures that proportionally the same amount of the core of the cross-correlation peak is used in every cross-correlation image. This reduces differential effects between cross-correlation images, and possible effects from scintillation, which would cause intensity differences between different sub-aperture images, resulting in a different cross-correlation peak intensity.

C_{thresh}, is then masked to the chosen window size, centered around the peak of the cross-correlation image, $C_{w,thresh}$. The center of mass measurement is then made on the windowed, thresholded cross-correlation image, as given in equation 2.12. The centroid is then calculated by combining the location of the windowed region in the full cross-correlation image, and the center of mass measurement of the windowed region, for the x and y dimensions using;

$$\begin{aligned} x_0 &= i_{\min} + x_{\text{com}} \\ y_0 &= j_{\min} + y_{\text{com}}, \end{aligned} \tag{2.15}$$

where x_{com} and y_{com} are the x and y center of mass measurements, and $i_{\min}$ $j_{\min}$ are the locations of the peak in the cross-correlation image.

If we take the cross-correlation image from Fig. 2.7 and apply the threshold and window the generated cross-correlation image appears like the one shown in Fig. 2.8. Here we see the threshold value has removed a large number of pixels from the cross-

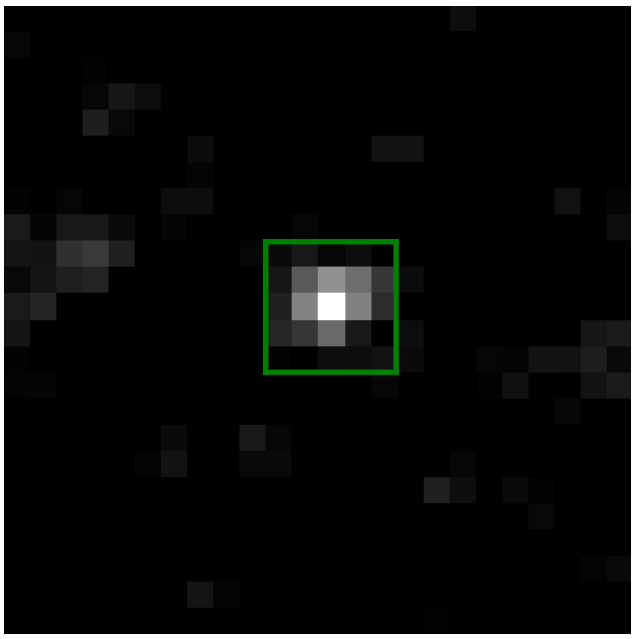

Figure 2.8: Example thresholded, windowed cross-correlation image. The threshold value has removed a large number of pixels which would add noise to a center of mass measurement. By only performing the center of mass in the green windowed region, the effect of the remaining pixels outside of the window are removed. This further reduces the noise on the center of mass measurement.

correlation image, which would add noise to the center of mass measurement. Also the window, shown in green, further removes pixels which would add noise far away from the cross-correlation peak.

2.2.2.3 Two-Dimensional Quadratic Interpolation

It has been found by November and Simon (1988) that the best interpolation methods for measuring the peak of a cross-correlation image generated from images of solar granules are polynomial fits of second order. Higher order fits tend so underestimate the shift when the displacement is small, and linear fits systematicallly overestimate the shift. A two-dimensional quadratic fit can perform as well as a Gaussian fitting algorithm, but is substantially less computationally expensive (Löf-

dahl, 2010). The parabolic fitting occurs on a small 3×3 pixel region, s, centered on the peak of the cross-correlation image, as described by Löfdahl (2010);

$$s_{i,j} = C_{i+i_{\max},j+j_{\max}}, \qquad i,j = -1,0,1 \tag{2.16}$$

where i and j go from -1 to 1 around the cross-correlation peak in the x and y directions respectively. $s_{0,0}$ corresponds to the peak of the cross-correlation image, in the center of the region. The parabola fitted to s is of the form;

$$f(x,y) = a_1 + a_2 x + a_3 x^2 + a_4 y + a_5 y^2 + a_6 xy. \tag{2.17}$$

The prefactors for the powers of x and y are then given by;

$$\begin{aligned} a_2 &= (s_{1,0} - s_{-1,0})/2 \\ a_3 &= (s_{1,0} - 2s_{0,0} + s_{-1,0})/2 \\ a_4 &= (s_{0,1} - s_{0,-1})/2 \\ a_5 &= (s_{0,1} - 2s_{0,0} + s_{0,-1})/2 \\ a_6 &= (s_{1,1} - s_{-1,1} - s_{1,-1} + s_{-1,-1})/4 \end{aligned} \quad . \tag{2.18}$$

The location of the minima can be found analytically from the above formulae in x and y using;

$$\begin{aligned} x_{\text{poly}} &= (2a_2a_5 - a_4a_6)/(a_6^2 - 4a_3a_5) \\ y_{\text{poly}} &= (2a_3a_4 - a_2a_6)/(a_6^2 - 4a_3a_5), \end{aligned} \tag{2.19}$$

where the values of $a_1 - a_6$ are given by equation 2.18. Then, in a similar manner as was done for the windowed, thresholded center of mass, this is combined with the location of the region in the full cross-correlation image, $i_{\min}$ and $j_{\min}$, to give an estimate of the centroid;

$$\begin{aligned} x_0 &= i_{\min} + x_{\text{poly}} \\ y_0 &= j_{\min} + y_{\text{poly}}. \end{aligned} \tag{2.20}$$

In high signal to noise ratios (SNR) the limiting factor of this technique arises from the biased sampling of the core of the cross-correlation peak, shown in Fig. 2.9. The under-sampling of the cross-correlation peak results in a systematic rounding effect, which biases the shift estimates towards integer values. This is especially

obvious in Fig. 2.9b, where both the x and y directions follow the same sawtooth pattern of residual error, with the error increasing as the cross-correlation peak moves away from being centered on a pixel.

The cause of the bias is illustrated in Fig. 2.10. Here we see the regions windowed for use in the 2D parabolic fit to the cross-correlation peak highlighted in red. This is a good mask for Fig. 2.10a, where the cross-correlation is well centered on a single pixel. However, this approach does not work as well in Fig. 2.10b, where centering around the brightest pixel in the cross-correlation image causes a bias towards the brightest pixel. This occurs because the areas around the "true" location of the peak are not being sampled equally. This leads to the parabolic fit estimating the location of the peak to be closer to the brightest pixel in the cross-correlation image than it actually is.

2.3 Noise in Cross-Correlation Images

There are two main ways noise enters a cross-correlation image. The noise in the images used to create the cross-correlation images manifest themselves in the cross-correlation image, described in § 2.3.1. The other major source of noise is from the correlation of regions of the images which are not common to both images, described in § 2.3.2.

2.3.1 Noise from correlation images

A major sources of noise in cross-correlation images arises from noise in the sub-aperture images and the reference image. These images can be described as containing both a signal, and noise part;

$$\begin{aligned} Im &= Im_s + Im_\sigma \\ Ref &= Ref_s + Ref_\sigma \end{aligned}, \tag{2.21}$$

where Im represents the overall sub-aperture image, Im_s describes the signal in the image, and Im_σ describes the noise associated with the image. In a similar way,

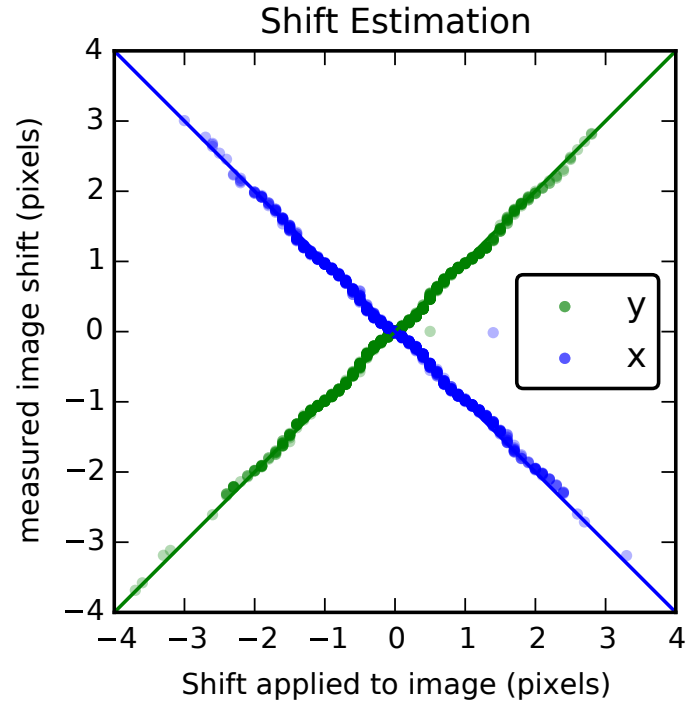

a

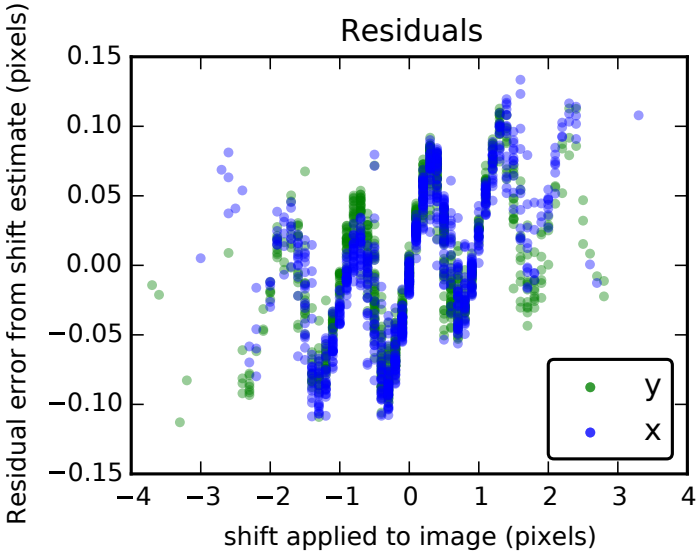

b

Figure 2.9: Residual errors from using a parabolic fit around an under-sampled correlation peak. Subfigure a shows the centroids for images, with the shifts applied. The negative of the y shifts is plotted to make them easier to distinguish from the x shifts. There is a "wobble" apparent in the two lines from under-sampling the correlation peak. This is more clearly visible as a systematic effect in Subfig. b, where the residuals are plotted. Here we see the under-sampling of the correlation peak as a "sawtooth" like pattern, with the best centroid estimates around integer pixel shifts.

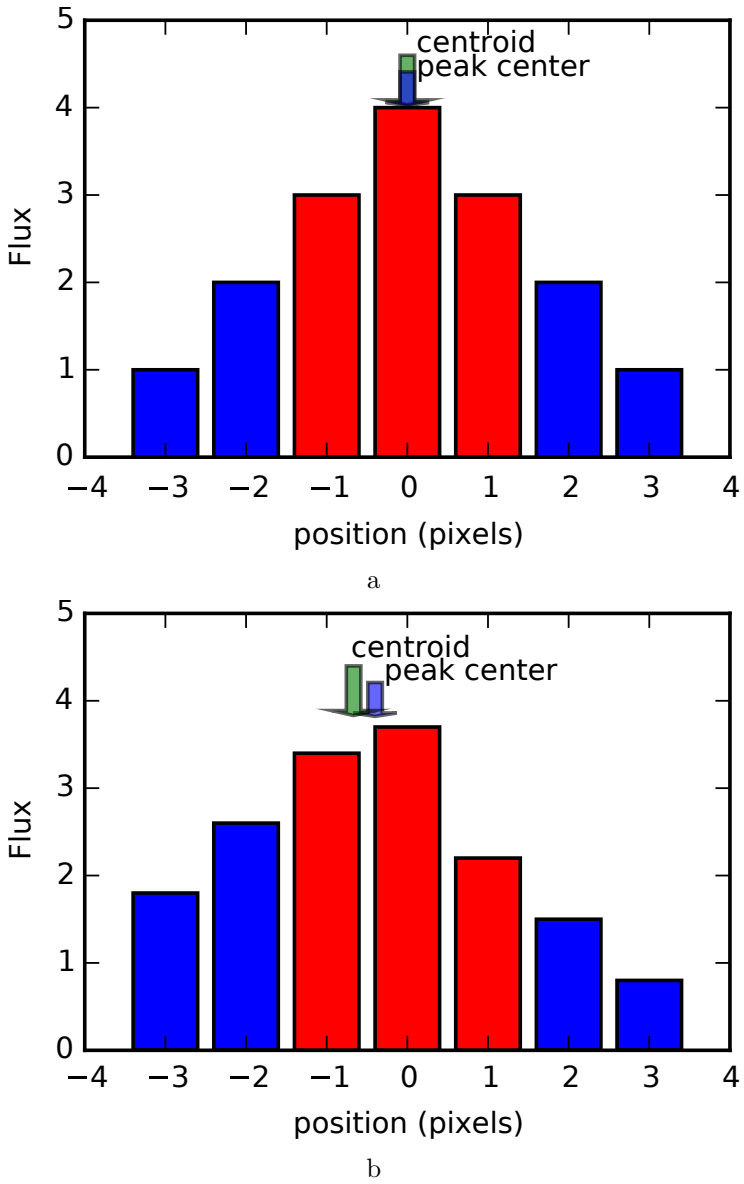

Figure 2.10: An illustrative one dimensional cut through a cross-correlation image, with the region used by the parabolic fit highlighted in red. The locations of the actual peak are shown by the green arrows labelled "centroid", and the parabolic fit location shown with the blue arrows labelled "peak center". Using only the 3 pixels around the center of the cross-correlation peak, the shift estimate can be biased away from the true location of the peak due to the uneven sampling. While Subfig. a shows the ideal case for using this method, where both sides of the peak are well sampled, there are some cases where the shift differs from the measured position due to the limited size of the region used, as shown in Subfig. b.

Ref represents the full reference image, Ref_s represents the signal in the reference image, and Ref_σ describes the noise in the reference image. When these images are combined using a cross-correlation technique, assuming a linear regime, the resulting cross-correlation image contains four terms;

$$C = C_{Im_s Ref_s} + C_{Im_s Ref_\sigma} + C_{Im_\sigma Ref_s} + C_{Im_\sigma Ref_\sigma}, \tag{2.22}$$

where C is the total signal in the cross-correlation image, $C_{Im_s Ref_s}$ corresponds to the sub-aperture image signal combined with the reference image signal, $C_{Im_s Ref_\sigma}$ represents the sub-aperture image signal combined with the reference image noise, $C_{Im_\sigma Ref_s}$ is the sub-aperture image noise combined with the reference image signal and $C_{Im_\sigma Ref_\sigma}$ is the sub-aperture image noise combined with the reference image noise. Noise in the cross-correlation image carries forward to errors on centroid measurements, as the the noise can change the apparent location of the cross-correlation peak.

It is not obvious how each of these terms affect the measured centroid, so I show here how adding and removing noise to the sub-aperture images, and reference image changes the error on the measured centroids in Fig. 2.11. This shows how the noise terms in equation 2.22 contribute towards the error on the measured centroid for various different Poisson SNR levels on images of solar granulation. To ensure there was no non-common image noise (see § 2.3.2), there was no shift added between any of the sub-aperture images, or the reference image.

Each line in Fig. 2.11 represents a different combination of noise in sub-aperture and reference images. The effect of global tip/tilt in each data set is negligible, apart from where noise is present only in the reference image (green lines), where two lines are shown, one for tip/tilt included and another after removing the global tip/tilt term. This difference demonstrates the effect of noise in the reference image to add a global offset to the centroid estimates, as the noise is common to all of the individual centroid estimates. Noise in the reference image can largely be ignored in WFSs as global tip/tilt is usually subtracted from the WFS measurements and

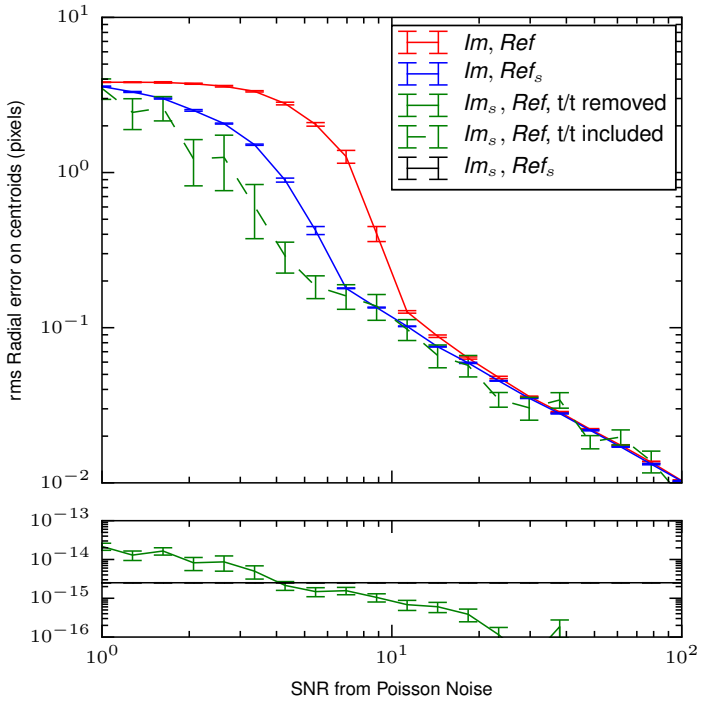

Figure 2.11: Noise contributions of sub-aperture and reference images to centroid error. The coloured lines represent how noise in each of the images combined in the cross-correlation affect the centroid estimate. The red line shows the error when noise is included in both the reference and sub-aperture images, the blue line when noise is included in the sub-aperture images only, the green lines when noise is included only on the reference image and the black line when no noise is included in either of the images. The green lines show two different cases, the dashed line for including the global tip/tilt term in the error and the solid line for removing the global tip/tilt term in the error, the other cases showed negligable difference between the two regimes.

measured by some other means.

The blue, red and dashed green lines in Fig. 2.11 follow similar trends. At the higher SNR levels the error on the centroid estimates all follow the same power law, while at lower SNR levels the effect of the different noise sources separate. There is a drop in the error on centroids from noise being present on both the reference and sub-aperture images (red line) compared to noise only being present on the sub-aperture images (blue line). This shows the effect of noise on both the sub-aperture and reference images combined. The effect of noise in the reference image is also apparent at low SNR when the effect of global tip/tilt is removed,

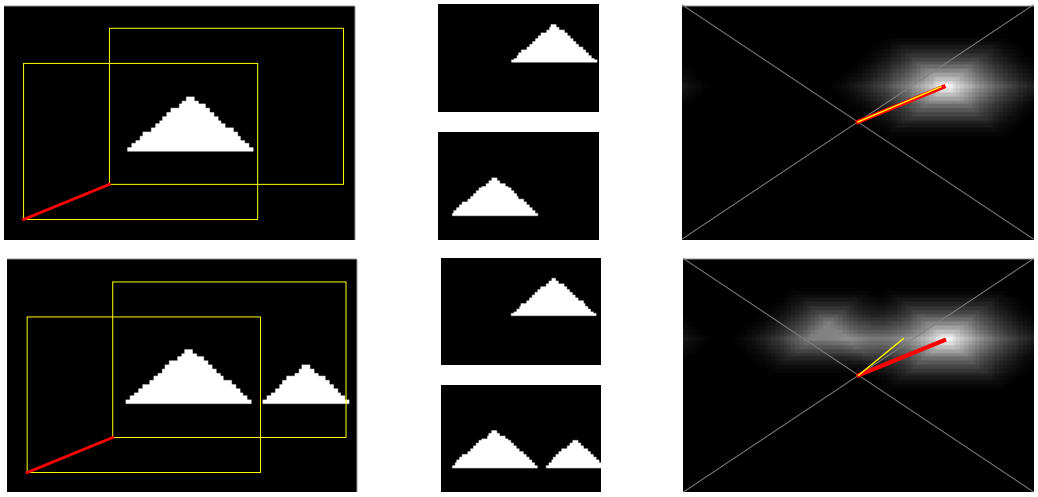

Figure 2.12: This simplified cartoon shows the effect on non-common image noise. The two yellow boxes represent sub-aperture images with relative shifts sampling the same large FOV, and are shown separately in the middle. The right side shows the cross-correlation image generated from the two sub-aperture images. The upper plot shows a single example structure, along with the two sub-aperture images, and the generated cross-correlation image. The location of the centroid on the correlation image is denoted by the yellow line, and the location of the actual shift is denoted with a red line. The lower plot shows an example with two structures of similar size and shape in the FOV, which affects the cross-correlation image and adds noise to the shift estimate.

as the error on centroid estimate in the green line seperates from the other noise sources. So while there is nothing to be gained at high SNR from removing noise in the reference image, it will have an effect in reducing this term for lower SNR images.

2.3.2 Non-Common Image Noise

The effect of misalignment, through differential tilt, of individual sub-aperture images changes the location of the sub-aperture FOV on the object being observed. This changes the structure visible in each of the sub-aperture images. The differing structure between sub-aperture images and the reference image can add noise into the cross-correlation images refered to from here as “non-common image noise” and is illustrated in Fig. 2.12.

The upper region of Fig. 2.12 shows the regime where a normal correlating WFS gives an accurate centroid estimate for the shift in position between the two sub-apertures. The "feature" is present in both of the sub-aperture images and the cross-correlation image generated from this contains one peak. This allows for an accurate centroid estimate, the red and yellow lines overlaid onto the cross-correlation image overlap well.

The lower part of Fig. 2.12 shows the regime where a normal correlating WFS no longer gives accurate centroid estimates. The new feature is only visible in one of the sub-apertures and adds spurious signal to the cross-correlation image, as can be seen by the extra peak visible in the cross-correlation image. While the peak is not as large as the one peak from the common feature overlapping, the extra peak adds an error to the centroid measurements, shifting the location of the centroid away from the true centroid position.

While the case shown in Fig. 2.12 is a simplified cartoon, this effect is present in cross-correlation images of solar granules. In the solar granule case the size and shape of the granules is very similar across the whole FOV, meaning that all granules correlate, to some degree, with all other ones. As there are many granules in a WFS image the effect isn't just a single extra cross-correlation peak, but rather a large background, which appears to have many lumps and bumps where the granules overlap.

2.4 Summary

In this chapter I described some of the methods currently used for centroiding images in WFSs observing extended objects. Noise on the centroid estimates come from two major locations, noise inherent in the individual images, and noise from non-common structure. Centroiding techniques attempt to minimise the impact of the noise inherent on the images through fitting to the correlation peak and there is no attempt to remove the effect of non-common image noise.

I investigate another method for minimising the effect of noise in the sub-aperture and reference images in chapter 4, by estimating optimal window and threshold parameters, which effectively remove the influence of noise from the centroid estimate. I also look at a method for reducing non-common image noise by using supersized reference images in chapter 5, where I also discuss methods of generating these supersized reference images using only the data from WFS frames.

Chapter 3

Atmospheric Turbulence and Turbulence Profiling Theory

A detailed understanding of the processes behind turbulence enables more precise measurement and correction of that turbulence. An understanding of the vertical distribution of turbulence is important for tomographic AO. To measure the vertical turbulence the spatial distribution and geometry of the system making the measurements need to be understood. In this chapter I outline the statistics underlying the structure of atmospheric turbulence in § 3.1 and § 3.2. I then go on to explain how the statistical properties of atmospheric turbulence can be measured through the motions it induces on images of astronomical objects in § 3.3. This is extended to describe instruments capable of measuring the vertical distribution of turbulence in the atmosphere with SLODAR in § 3.4, S-DIMM+ in § 3.5 and other profiling methods in § 3.6. The SLODAR technique is used in Chapter 6 as a basis for the development of So-SLODAR.

3.1 Atmospheric Turbulence

Atmospheric turbulence is induced from energy being added to the atmosphere, predominantly through solar heating. This heated air then mixes with air of dif-

ferent temperatures causing optical turbulence, due to the air masses of different temperatures having different refractive indices. The spatial de-correlation of the temperature leads to de-correlation of the refractive index, which cause variations in the optical path length to a telescope pupil, adding aberrations to any images formed by the telescope.

The optical properties of atmospheric turbulence occur on scales which are of the order mm − m. Visible light has a wavelength of ~ 500 nm, a substantially different scale to the structure of atmospheric turbulence. This means that atmospheric diffraction effects can be largely ignored for the size of pupils employed by our WFSs, and simple geometrical propagation of the wavefronts employed in propagating light from one turbulent region to another in simulation. The temporal evolution of the turbulence is also relatively slow when compared to the transit time of light through the turbulence. This allows for the assumption of frozen flow (Hardy, 1998) to be used.

3.1.1 Kolmogorov Turbulence

The processes involved in generating atmospheric turbulence are largely random, as such the best way to describe it is through statistical properties. Kolmogorov (1941) proposed a mathematical description of turbulence, which was further developed by Klyatskin and Tatarskii (1972). A flow is considered turbulent if the Reynolds number, Re, defined by;

$$Re = \frac{V_0 L_0}{\nu_0}, \tag{3.1}$$

where V_0 is the characteristic velocity of the flow, L_0 is the characteristic size, and ν_0 is the viscosity of the fluid, exceeds a critical value (Reynolds, 1894). For a moderately sized atmospheric disturbance in air, with $L_0 = 15\text{m}$, $\nu_0 = 15 \times 10^{-6}\text{m}^2\text{s}^{-1}$, and a flow velocity of 1ms^{-1}, $Re = 1 \times 10^6$, which greatly exceeds the critical value for air, $\approx 2500 - 5000$ (Vinnichenko, 2013). Velocities in the

atmosphere are expected to be greater than 1ms^{-1}, so all atmospheric disturbances can be assumed to be turbulent.

The turbulence is bound by the region where the energy is added to the atmosphere, called the "outer scale", L_0. This then breaks down, until eventually an "inner scale", l_0, is reached, where the energy is dissipated by friction between the molecules and Re drops below its critical value. For this to happen continuously, the rate of dissipation of the energy to heating the atmosphere must be the same as the rate of input of energy to the region of atmosphere. If we consider a region of turbulence between the inner and outer scale, the velocity fluctuations from the turbulence, V (ms^{-1}) are determined only by the scale size, l(m) , and the rate of energy transport through the turbulent region, ϵ ($\text{kgm}^2\text{s}^{-3}$). Dimensional analysis gives the relation;

$$V \propto \epsilon^{1/3} l^{1/3}, \tag{3.2}$$

which implies the fluctuational energy in perturbations of size l is proportional to $l^{2/3}$ (Hardy, 1998).

The atmosphere is a non-stationary entity, which is continuously evolving. When considering the light cone of a telescope, we are only concerned with the differences between different regions of the atmosphere, rather than its absolute properties. The structure function gives the intensity of fluctuations over different scales. There are a number of other reasons why structure functions are used, which are discussed in Roddier (1981). The structure function of velocity, $D_V(\mathbf{r})$, over the spatial seperation $\mathbf{r}$, is defined as;

$$D_V(\mathbf{r}) = \langle |V(\mathbf{x}) - V(\mathbf{x}+\mathbf{r})|^2 \rangle = C_V^2 \mathbf{r}^{2/3}, \tag{3.3}$$

where $\langle\rangle$ represents the average over all positions $\mathbf{x}$, $V(\mathbf{x})$ denotes the velocity at a point, $\mathbf{x}$, and $V(\mathbf{x}+\mathbf{r})$ the velocity at a point $\mathbf{r}$ away from $\mathbf{x}$. C_V^2 is the structure function for velocity, a parameter that depends on the energy flowing through the region of atmosphere. In astronomy we are interested in the perturbations to a wavefront of light caused by the changes in refractive index of the atmosphere.

In a similar definition (Schmidt, 2010), the structure function for the refractive index, $D_n(r)$, can be defined;

$$D_n(r) = C_n^2 r^{2/3}, \qquad l_0 < r < L_0 \tag{3.4}$$

where C_n^2 is the refractive-index structure parameter. This is only valid in regions between the inner scale, l_0, and the outer scale L_0 of turbulence. We can attain the refractive-index power spectral density (PSD) of the turbulence, Φ_n^κ;

$$\Phi_n^\kappa = 0.033 C_n^2 \kappa^{-11/3}, \qquad \frac{1}{L_0} \ll \kappa \ll \frac{1}{l_0} \tag{3.5}$$

where $\kappa = 2\pi/l$ and l is the spatial scale of turbulence.

3.1.2 Von-Kàrmàn Turbulence

There are other models for the refractive-index power spectrum density, one such is the von Kàrmàn PSD. This is a modified Kolmogorov spectrum, which takes into account the outer scale;

$$\Phi_n^{vK} = \frac{0.033 C_n^2}{(\kappa^2 + \kappa_0^2)^{11/6}}, \qquad 0 \leq \kappa \ll \frac{1}{l_0} \tag{3.6}$$

where $\kappa_0 = 2\pi/L_0$. A comparison between the refractive-index power spectrum densities of Kolmogorov and von Kàrmàn turbulence are shown in Fig. 3.1. The chosen value for the outer scale in the von Kàrmàn spectrum was 100m. The value of the outer scale of turbulence has been measured to be anywhere between 10m − 300m (Coulman et al., 1988; Agabi et al., 1995; Lukin et al., 1999; Ziad et al., 2000; Dali Ali et al., 2010).

3.2 Imaging Through the Atmosphere

Light passing through a turbulent layer in the atmosphere will be perturbed by the refractive-index variations. Light in astronomy can be assumed to come from infinity, meaning it is a plane wave when it reaches the atmosphere;

$$\Psi_h(\mathbf{x}) = A e^{i\phi(\mathbf{x})}, \tag{3.7}$$

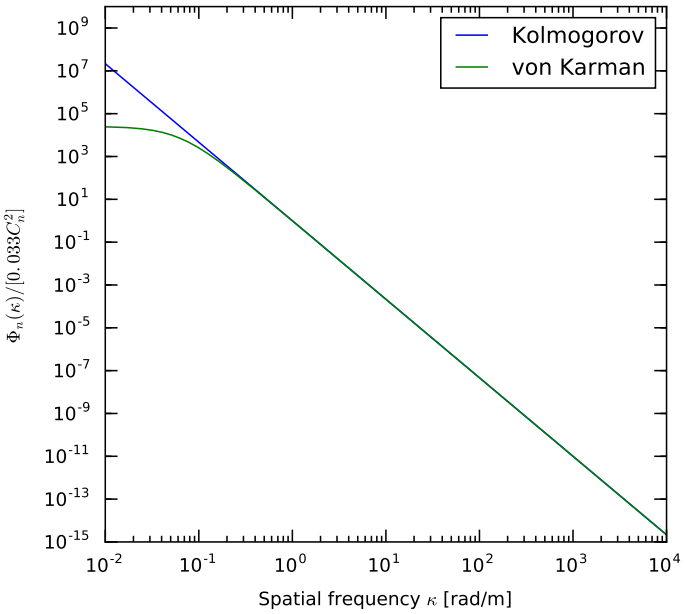

Figure 3.1: The refractive-index power spectrum of Kolmogorov and von Kàrmàn turbulence. Both follow the same power law for high spatial frequencies, of -11/3. However they start to differ at low spatial frequencies, where the von Kàrmàn spectrum has an outer scale defined, removing power at larger scales.

where $\Psi_h(\mathbf{x})$ is the wavefront, with phase $\phi(\mathbf{x})$ and amplitude A, over the spatial co-ordinate $\mathbf{x}$. After passing through a turbulent layer of the atmosphere, the phase is perturbed by $d\Phi(\mathbf{x})$;

$$d\Phi(\mathbf{x}) = k \int_{h}^{h+\delta h} \mathrm{n}(\mathbf{x}, z) dz, \tag{3.8}$$

where $k = 2\pi/\lambda$, the turbulent layer is at height h, has thickness δh and $\mathrm{n}(\mathbf{x}, z)$ is the refractive index. The wavefront perturbations will not be achromatic, due to dispersion, making the optical effects of atmospheric turbulence worse towards the blue end of the spectrum. As previously stated, we are not interested in absolute phase, but rather the difference in phase between points, $\phi(\mathbf{x})$ and $\phi(\mathbf{x}+\mathbf{r})$, where $\mathbf{r}$ is the displacement (ξ, η). Hence, we use the structure function for ϕ, $D_\phi(\mathbf{r})$;

$$D_\phi(\mathbf{r}) = \langle |\phi(\mathbf{x}) - \phi(\mathbf{x}+\mathbf{r})|^2 \rangle. \tag{3.9}$$

Roddier (1999) showed that equation 3.4 can be used with equation 3.8 and equation 3.9 to give the structure function as;

$$D_\phi(\mathbf{r}) = 2.91k^2r^{5/3}\int C_n^2(z)dz. \tag{3.10}$$

Turbulent layers are typically taken to be parallel horizontal layers, with z corresponding to distance orthogonal to the turbulent layer. Equation 3.10 can be modified so instead of the direction z, the turbulence is defined at height above the ground h;

$$D_\phi(\mathbf{r}) = 2.91k^2r^{5/3}\cos^{-1}(\gamma)\int C_n^2(h)dh, \tag{3.11}$$

where γ is the angular distance from zenith to the observed source.

3.2.1 Fried's Parameter

Equation 3.11 can be written as

$$D_\phi(\mathbf{r}) = 6.88(r/r_0)^{5/3}, \tag{3.12}$$

where r_0 is the Fried parameter (Fried, 1966), and is given by;

$$r_0 = \left[0.423k^2(\cos(\gamma))^{-1}\int C_n^2(h).\mathrm{d}h\right]^{-3/5}, \tag{3.13}$$

and characterises the integrated turbulence for a particular direction through the atmosphere, at a given wavelength. It describes the largest diameter of a telescope which will produce diffraction limited images, above this diamter the performance will begin to be limited by the effects of atmospheric turbulence (Young, 1974). Equation 3.13 gives the wavelength dependance of r_0 as;

$$r_0 \propto \left(k^2\right)^{-3/5} \propto \lambda^{6/5}. \tag{3.14}$$

If the resolution is limited by the atmosphere, the r_0 value can be related to a "seeing" value using;

$$\Delta\theta \sim \frac{\lambda}{r_0}, \tag{3.15}$$

where $\Delta\theta$ is the smallest resolvable distance between two objects. This is a modified version of the Rayleigh Criterion (Rayleigh, 1874) where instead of the telescope diameter limiting the resolution the atmosphere is the limiting factor taking the form of Fried's parameter.

3.3 Seeing Measurements

For observing sites one of the site-statistics that can be measured is the integrated turbulence along the line of sight of the telescope. This is critical in the choice of site for a telescope to achieve the highest resolution and usually takes the form of the width of the PSF seen on a detector. If the airmass is taken into account, this can converted into a value for r_0.

3.3.1 Differential Image Motion Monitor

A differential image motion monitor (DIMM) measures the relative motion of two images in order to get a measure of r_0 (Sarazin and Roddier, 1990). For a plane wave of light traveling normal to a turbulent layer, the component α of the angle-of-arrival fluctuation in the x direction induced by the turbulence is described by;

$$\alpha(x, y) = -\frac{\partial}{\partial x} z(x, y), \tag{3.16}$$

where;

$$z(x, y) = \frac{\lambda}{2\pi} \phi(x, y), \tag{3.17}$$

$z(x, y)$ is the wavefront phase $\phi(x, y)$. The angle of arrival of the rays from a star is linearly linked to the motion of the image of the star of the detector by the plate scale, which can be measured though centroiding the image. The covariance of the angle-of-arrival is then given by;

$$B_\alpha(\xi, \eta) = \langle \alpha(x, y), \alpha(x + \xi, y + \eta) \rangle, \tag{3.18}$$

for a point (ξ, η) away from (x, y). This can be related to the covariance of the phase fluctuations using equation 3.16;

$$B_\alpha(\xi,\eta) = -\frac{\lambda^2}{4\pi^2}\frac{\partial^2}{\partial\xi^2}B_\phi(\xi,\eta). \tag{3.19}$$

The structure function, defined in equation 3.9, can be written as;

$$D_\phi(x,y) = 2\left[B_\phi(0,0) - B_\phi(\xi,\eta)\right]. \tag{3.20}$$

This can be combined with equation 3.19 to give;

$$B_\alpha(\xi,\eta) = \frac{\lambda}{8\pi^2}\frac{\partial^2}{\partial\xi^2}D_\phi(\xi,\eta). \tag{3.21}$$

The relation between the phase structure function and r_0 given in equation 3.12, and using $r = \sqrt{\xi^2+\eta^2}$ can then be combined;

$$\begin{aligned} B_\alpha(\xi,\eta) &= 0.087\lambda^2 r_0^{-5/3}\tfrac{\partial^2}{\partial\xi^2}\left[\xi^2+\eta^2\right]^{5/6} \\ &= 0.145\lambda^2 r_0^{-5/3}\left[(\xi^2+\eta^2)^{-1/6} - \tfrac{1}{3}\xi^2(\xi^2+\eta^2)^{-7/6}\right], \end{aligned} \tag{3.22}$$

which gives the covariance of the angle-of-arrival fluctuations. This general equation can be simplified greatly if we set ξ or η to 0, corresponding to latitudinal and longitudinal separations;

$$\begin{aligned} B_l(d) &= B_l(d,0) &&= 0.097\lambda^2 r_0^{-5/3} d^{-1/3} \\ B_t(d) &= B_t(0,d) &&= 0.145\lambda^2 r_0^{-5/3} d^{-1/3}, \end{aligned} \tag{3.23}$$

where d is the magnitude of the separation. These equations form the basis of SLODAR, which triangulates the altitude of turbulence using the covariances of sub-apertures which are separated across a telescope pupil, however, this description fails at the origin. In reality the origin is limited by the averaging over the aperture, and is given by Fried (1966); Fried and Mevers (1974); Tokovinin (2002);

$$B_\alpha(0,0) = 0.179\lambda^2 r_0^{-5/3} D^{-1/3}, \tag{3.24}$$

where D is the diameter of the aperture. This is only true for the motion in one dimension. The two dimensional variance for the motion in a single aperture, σ_c^2, is given by;

$$\sigma_c^2 = 2B_\alpha(0,0) = 0.358\lambda^2 r_0^{-5/3} D^{-1/3}. \tag{3.25}$$

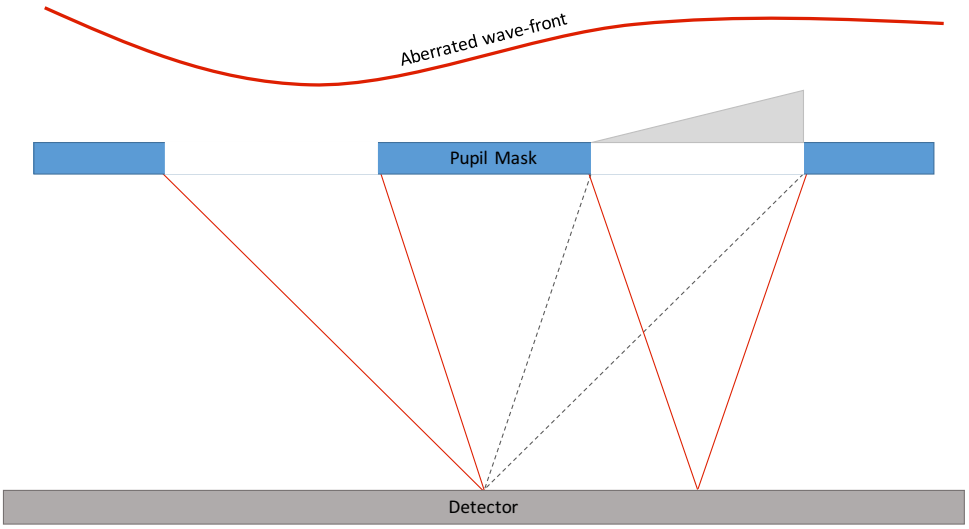

Figure 3.2: Example DIMM instrument. A mask is placed over the pupil, with two holes. One hole has a wedge plate placed over it, to separate the images formed by the two sub-pupils. The relative motions of the stars on the detector can be related to r_0 through equation 3.23.

These calculations can also be performed for a square aperture (such as the sub-apertures in a SH-WFS), for one dimension (Saint-Jacques, 1998), which yields;

$$\sigma_c^2 = 0.162\lambda^2 r_0^{-5/3} d^{-1/3}. \tag{3.26}$$

A typical DIMM consists of a small telescope with a pupil mask with two apertures, one of which has a wedge plate over it. This adds a tilt to the light entering one of the apertures, moving the position of the spot formed when observing a star. The detector plane then images two separate spots, one from each aperture. An example of this is given in Fig. 3.2. Over a series of short exposures, the covariance of the motion of the two spots can be measured. This can then be used with equations 3.23 to estimate r_0.

3.4 Slope Detection and Ranging

SLODAR was proposed by Wilson (2002) as a method for estimating the altitude distribution of turbulence (from here on known as turbulence profile) in the atmosphere. The turbulence profile is calculated by fitting the measured covariances of slopes for different sub-aperture in a SH-WFS to response functions, the response of the SLODAR to a single turbulent layer at a given altitude. Knowledge of the profile of atmospheric turbulence is especially important, with the advent of tomographic AO systems, such as CANARY (Gendron et al., 2011), and MCAO systems (Louarn et al., 2000), including the Dunn Solar Telescope (Langlois et al., 2004).

SLODAR splits a telescope pupil into many sub-pupils, referred to as sub-apertures, and observes two stars simultaneously through them. The covariances of the motion of the stars observed in these different sub-apertures can be used to estimate the strength of the atmospheric turbulence, and its height distribution. An example of how the height of a layer of turbulence can be sensed is given in Fig. 3.3.

Considering the example in Fig. 3.3, with two stars separated by angle θ, a turbulent layer at altitude H and two sub-apertures separated by distance Δw, where w is the sub-aperture width and Δ is the separation in units of sub-apertures. The star separation produces "copies" of the turbulence at the ground, shifted by;

$$\Delta w = H\theta. \tag{3.27}$$

There should be a peak in the cross-correlation at the separation Δ if the turbulence is at altitude H. The maximum number of sub-apertures across the telescope pupil, n_{sub}, is effectively limited by diffraction and signal, as the sub-aperture images need to be smaller than the sub-aperture pitch, giving a minimum sub-aperture size of $5 - 10$cm. The vertical resolution of a SLODAR with n_{sub} sub-apertures is then given by;

$$\delta H = \frac{D}{n_{\text{sub}}\theta}, \tag{3.28}$$

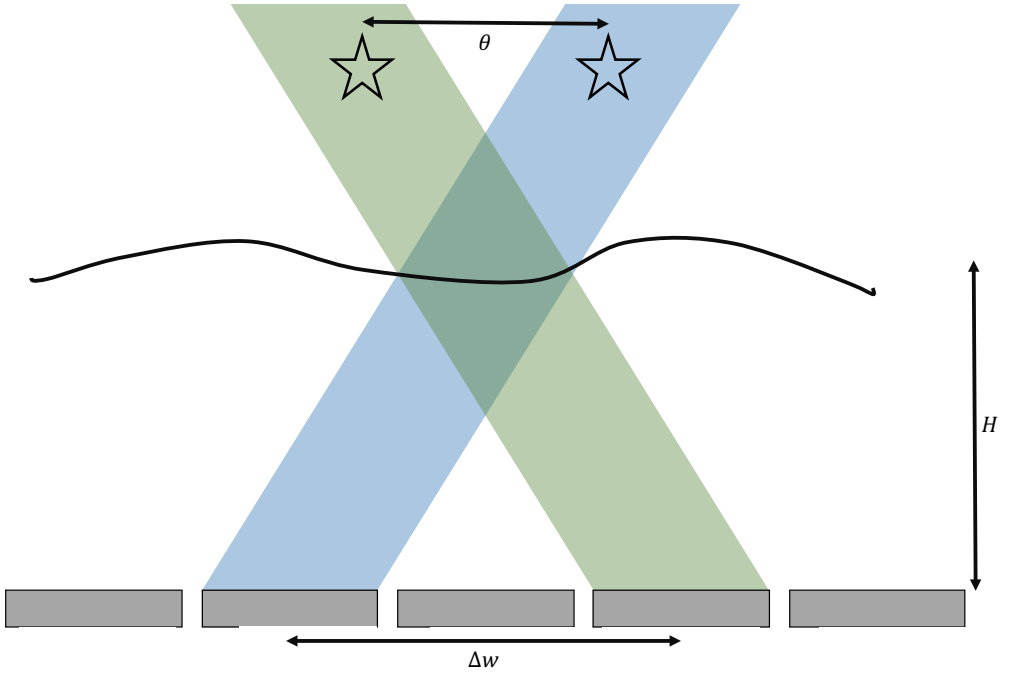

Figure 3.3: The turbulent layer shown will induce the same spot motions in both the blue and green sub-apertures. This peak in correlation of the motions can be seen in the covariances, and the altitude derived from the geometry of the system.

where δH is the altitude resolution of the SLODAR and D is the diameter of the telescope, assuming the pupil has exactly n_{sub} sub-apertures across it. The maximum altitude that can be sensed, H_{max}, is given by;

$$H_{\text{max}} = n_{\text{sub}} \delta H. \tag{3.29}$$

The full altitude resolution of SLODAR is illustrated by Fig. 3.4. The number of sub-apertures across the pupil sets the limit on the number of resolution elements the SLODAR will have. The altitude resolution, and the maximum sensed altitude of resolution is then defined by the angular separation of the observed stars. For stars which are close together, the altitude bins are large, but the maximum sensed altitude is high. Conversely, for stars with a large separation, the altitude bins are small, but the maximum sensed altitude is low. The measured covariances are fitted to a series of response functions, functions which describe the response of the system to a single layer of turbulence at a given altitude, in order to determine the turbulence profile.

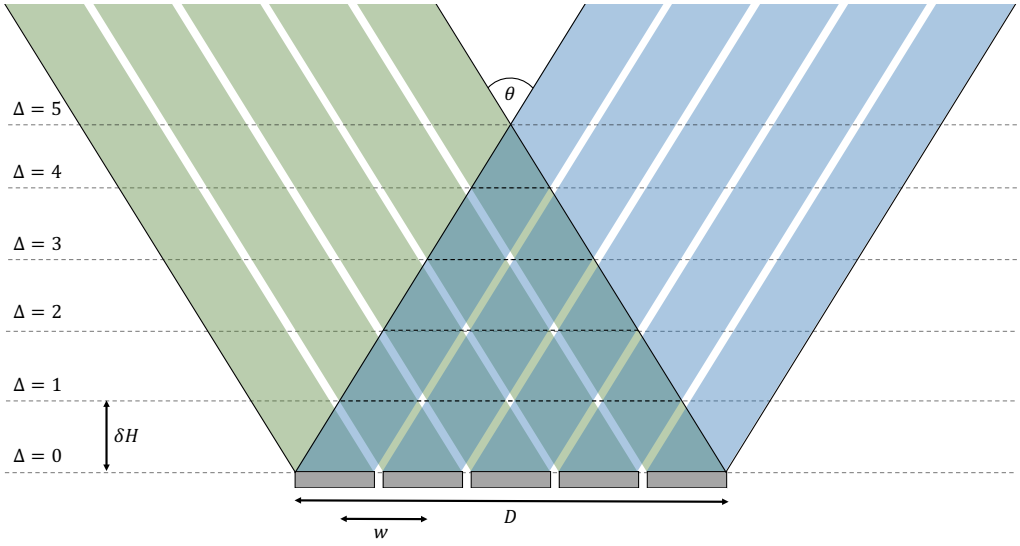

Figure 3.4: The altitude resolution of a SLODAR is determined by the number of sub-apertures across the pupil, and the angular separation of the observed stars. The number of sub-apertures across the pupil defines the number of resolution elements of a SLODAR. The spacing of the stars defines the altitude resolution, and the maximum sensed altitude of the system.

3.4.1 Response Functions

The cross-covariance functions of the WFS slopes for each of these sensed altitudes can be calculated and used for fitting the measured cross-covariances of a SLODAR to estimate the turbulence profile, as described by Butterley et al. (2006). This method uses the fact that the measured cross-covariance is simply the sum of the individual layer responses, thus we can consider each layer independently. If we label the sub-apertures on a telescope pupil with i, j across the x, y directions respectively, and define the tilt in the x direction for the first star as $s_{i,j}^{x[1]}$;

$$s_{i,j}^{x[1]} = \int \phi(w\mathbf{r}_{i,j}^{[1]}) F_x(\mathbf{r}_{i,j}^{[1]}) W(\mathbf{r}_{i,j}^{[1]}) d\mathbf{r}_{i,j}^{[1]}, \tag{3.30}$$

where $\mathbf{r}_{i,j}^{[1]}$ is the spatial co-ordinate, defined in units of the sub-aperture width, w, with the origin being the centre of sub-aperture $[i, j]$, and $\phi(\mathbf{r}_{i,j}^{[1]})$ is the phase in the plane of the sub-aperture. The sub-aperture is constrained by the pupil function;

$$\begin{aligned} W(\mathbf{r}) &= 1 \qquad \text{for } |x|, |y| < 1/2 \\ &= 0 \qquad \text{otherwise.} \end{aligned} \tag{3.31}$$

Finally F_x is the linear slope function in one direction (in this case x), normalised such that;

$$\int F_x^2(\mathbf{r})W(\mathbf{r})d\mathbf{r} = 1. \tag{3.32}$$

Similar definitions hold for the second star, $s^{x[2]}_{i',j'}$.

The cross-covariance of the x slopes in two sub-apertures observing different stars are given by;

$$C^x_{i,j,i',j'} = \langle s^{x[1]}_{i,j} s^{x[2]}_{i',j'} \rangle, \tag{3.33}$$

where $s^{x[1]}_{i,j}$ is the slope measured for star [1] in sub-aperture i,j, and $s^{x[2]}_{i',j'}$ is the slope measured for star [2] in sub-aperture i',j'. The angular brackets denote an average over a large number of independent realisations of the turbulence. The spatial offset of the two sub-apertures, in units of w, is then simply;

$$\mathbf{u} = (\delta i, \delta j) = (i' - i, j' - j). \tag{3.34}$$

Equation 3.30 can be substituted into equation 3.33 to give;

$$C^x_{i,j,i',j'} = \int\int \langle \phi^{[1]}_{i,j}(w\mathbf{r}^{[1]}_{i,j}) \phi^{[2]}_{i',j'}(w\mathbf{r}^{[2]}_{i',j'}) \rangle F_x(\mathbf{r}^{[1]}_{i,j}) F_x(\mathbf{r}^{[2]}_{i',j'}) \times W(\mathbf{r}^{[1]}_{i,j} W(\mathbf{r}^{[2]}_{i',j'}) d\mathbf{r}^{[1]}_{i,j} d\mathbf{r}^{[2]}_{i',j'}. \tag{3.35}$$

As the gradient of the phase is measured in each sub-aperture, the mean phase (or piston term) over the full telescope aperture is not sensed. The piston term needs to be removed from the phase, as it it not sensed. The covariance of the slopes, with piston removed, across two apertures has been shown by Wilson and Jenkins (1996) to be;

$$\begin{aligned} \langle \Phi^{[1]}_{i,j}(w\mathbf{r}^{[1]}_{i,j}) \Phi^{[2]}_{i',j'}(w\mathbf{r}^{[2]}_{i',j'}) \rangle = \quad & -\tfrac{1}{2} D_\phi(w\mathbf{x}) \\ & +\tfrac{1}{2} \textstyle\int W(\mathbf{r}^{[1]}_{i,j}) D_\phi(w\mathbf{x}) d\mathbf{r}^{[1]}_{i,j} \\ & +\tfrac{1}{2} \textstyle\int W(\mathbf{r}^{[2]}_{i',j'}) D_\phi(w\mathbf{x}) d\mathbf{r}^{[2]}_{i',j'} \\ & -\tfrac{1}{2} \textstyle\int\int W(\mathbf{r}^{[1]}_{i,j}) W(\mathbf{r}^{[2]}_{i',j'}) D_\phi(w\mathbf{x}) d\mathbf{r}^{[1]}_{i,j} d\mathbf{r}^{[2]}_{i',j'}, \end{aligned} \tag{3.36}$$

where $\Phi^{[1]}_{i,j}(w\mathbf{r}^{[1]}_{i,j})$ is the phase with piston removed, and $\mathbf{x} = \mathbf{u} + \mathbf{r}^{[2]}_{i',j'} - \mathbf{r}^{[1]}_{i,j}$.

In order to remove the effects of telescope wind-shake, guiding errors, and other common motion, the global tip/tilt term is subtracted from all of the slope measurements. Removing the tip/tilt not only removes these error sources, but also the tip/tilt term induced from the atmospheric turbulence. As the light from the two stars is passing through different columns of turbulence (see Fig. 3.3), the tip/tilt term induced by the turbulence will be different for each star. We choose to treat each star independently, removing the tip/tilt term separately for each star. The covariances of the tip/tilt subtracted slopes in the x direction for a turbulent layer with an offset of Δ sub-apertures is then given by;

$$\begin{aligned} C'^{x}_{i,j,i',j'}(\Delta) &= \langle (s^{[1]}_{i,j} - \overline{s^{[1]}})(s^{[2]}_{i'+\Delta,j'} - \overline{s^{[2]}}) \rangle \\ &= \langle s^{[1]}_{i,j} s^{[2]}_{i'+\Delta,j'} \rangle - \langle s^{[1]}_{i,j} \overline{s^{[2]}} \rangle - \langle \overline{s^{[1]}} s^{[2]}_{i'+\Delta,j'} \rangle + \langle \overline{s^{[1]} s^{[2]}} \rangle, \end{aligned} \tag{3.37}$$

where $\overline{s}$ represents the average tilt across the pupil, so for $\overline{s^{[1]}}$;

$$\overline{s^{[1]}} = \frac{1}{N_{\text{sub}}} \sum_{\text{valid } i,j} s^{[1]}_{i,j}, \tag{3.38}$$

and N_{sub} is the total number of un-vignetted sub-apertures observed across the pupil. The cross terms are given by;

$$\begin{aligned} \langle \overline{s^{[1]}} s^{[2]}_{i'+\Delta,j'} \rangle &= \tfrac{1}{N_{\text{sub}}} \sum_{\text{valid } i,j} \langle s^{[1]}_{i,j} s^{[2]}_{i'+\Delta,j'} \rangle \\ \langle s^{[1]}_{i,j} \overline{s^{[2]}} \rangle &= \tfrac{1}{N_{\text{sub}}} \sum_{\text{valid } i'+\Delta,j'} \langle s^{[1]}_{i,j} s^{[2]}_{i'+\Delta,j'} \rangle. \end{aligned} \tag{3.39}$$

Now the covariance for the individual overlapping sub-apertures separated by Δ sub-apertures can be calculated. The full two dimensional functions are not required if the velocity profile is not being calculated, as a one dimensional slice provides all the required information to extract a profile. The one dimensional (x) response function for SLODAR to a turbulent layer at height H is given by;

$$X_L(\Delta, \delta i) = \frac{1}{N_{\text{sub}}} \sum_{\text{valid} i,j,i'} C'^{x}_{i,j,i',j}(\Delta), \tag{3.40}$$

where N_{sub} is now the number of sub-aperture pairs which can have separation δi.

An example set of tip/tilt subtracted response functions for a single row of 10 sub-apertures across a 1m circular pupil are shown in Fig. 3.5. The shape of the

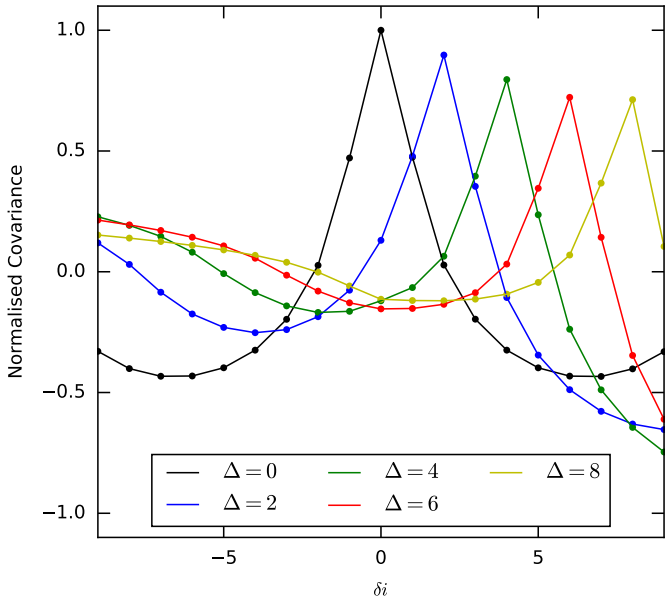

Figure 3.5: Example longitudinal SLODAR response functions for a row of 10 sub-apertures across a 1m telescope pupil. Only the functions for even Δs are shown for clarity. They have been normalised by the peak value of the auto-covariance ($\Delta = 0$).

auto-covariance can be seen in black, along with the response functions for the even separations of sub-apertures. The peak decreases in height for the higher altitude response functions (larger Δ) and the shape of the wings also change due to the tip/tilt term, which is subtracted, differing for different altitudes.

The measured cross-covariance can then be fitted with a linear least squares minimisation to a set of response functions, such as those shown in Fig. 3.5, to generate a turbulence profile.

Care needs to be taken in order to ensure that the turbulence is properly spatially sampled. The pupil is a window on the larger scale structure of the turbulent layers, so any individual measurement of the atmosphere will not sample all of the larger scale structure. It is important the sample of slopes used to estimate a turbulence profile properly samples all spatial scales of the turbulence. This can be understood if the turbulence is assumed to follow frozen flow (Taylor, 1938), and blows across the telescope pupil at a given velocity. The turbulence is static,

but appears to change as different regions of it pass over the telescope pupil. Using a large temporal window, typically sampling over one minute, should ensure that all spatial scales of the turbulence have "blown" across the pupil, and hence be properly sampled.

It should be noted that this method does not provide a direct estimate of the total strength of the turbulence along the line-of-sight. The auto-covariance function can be used to estimate the strength of the integrated turbulence (Butterley et al., 2006), or the previously mentioned DIMM method can be applied to the sub-aperture images (Sarazin and Roddier, 1990), however, this method is subject to noise on the centroid measurements.

3.5 Solar-Differential Image Motion Monitor +

One method of estimating the atmospheric profile during the day is S-DIMM+ (Scharmer and van Werkhoven, 2010), based on the S-DIMM seeing estimation technique (Beckers, 2001). As with the SLODAR (Wilson, 2002) technique this only uses the longitudinal and transverse directions for correlations, as the full two dimensional correlation is not necessary for calculating a turbulence profile.

The slopes measured by the S-DIMM+ are analysed in a similar way to the DIMM, where the variance of differential motion between different apertures are compared. So unlike SLODAR, where the a high covariance between slopes indicates the presence of a turbulent layer at a given atltitude, the S-DIMM+ measures no differential motion between sub-apertures if there is a turbulent layer present at the overlap altitude. The resolution of this technique is similar to SLODAR, as the same geometry is used in the WFS, the only difference is in the analysis of the measured slopes.

The first sub-aperture is assumed to be located at the origin, on-axis to the target. This means the measured centroid, δx_1 is then given by the sum of centroids

induced by all turbulent layers;

$$\delta x_1(\Delta w, 0) = \sum_{n=1}^{N} (s_n(\Delta w) - s_n(0)), \tag{3.41}$$

where the separation in the x direction is Δw, $s_n(\Delta w)$ is the wavefront slope induced by the turbulent layer n in the sub-aperture, and $s_n(0)$ is the centroid induced by the reference sub-aperture at layer n. A measurement in the same sub-aperture of an off-axis target at an angle α is then given by;

$$\delta x_2(\Delta w, \alpha) = \sum_{n=1}^{N} (s_n(\Delta w + \alpha h_n) - s_n(\alpha h_n)), \tag{3.42}$$

where h_n is the height of the turbulent layer n. The layers are all assumed to be independent, so the covariance between the two measurements, $\langle \delta x_1 \delta x_2 \rangle$ will be;

$$\langle \delta x_1 \delta x_2 \rangle = \sum_{n=1}^{N} \langle (s_n(\Delta w) - s_n(0))(s_n(\Delta w + \alpha h_n) - s_n(\alpha h_n)) \rangle, \tag{3.43}$$

which can be expanded to give;

$$\langle \delta x_1 \delta x_2 \rangle = \sum_{n=1}^{N} \frac{1}{2} \langle (s_n(\alpha h_n - \Delta w) - s_n(0))^2 \rangle + \frac{1}{2} \langle (s_n(\alpha h_n + \Delta w) - s_n(0))^2 \rangle - \langle (s_n(\alpha h_n) - s_n(0))^2 \rangle. \tag{3.44}$$

Sarazin and Roddier (1990) have shown that the longitudinal variances of the motion of two stars is given by;

$$\begin{aligned} \langle (s(\Delta w) - s(0))^2 \rangle &= 0.358 \lambda^2 r_0^{-5/3} D^{-1/3} \left(1 - 0.541 \left(\frac{\Delta w}{D} \right)^{-1/3} \right) \\ &= 0.358 \lambda^2 r_0^{-5/3} D^{-1/3} I \left(\frac{\Delta w}{D}, 0 \right), \end{aligned} \tag{3.45}$$

where $I\left(\frac{\Delta w}{D}, 0\right)$ is defined in Sarazin and Roddier (1990).

3.5.1 Expanding Pupil Problem

One of the effects of using an extended source instead of a point source when measuring image motion is that the size of the pupil as a function of altitude is not constant. This is shown in Fig. 3.6. The size of the effective pupil, D_{eff}, is simply

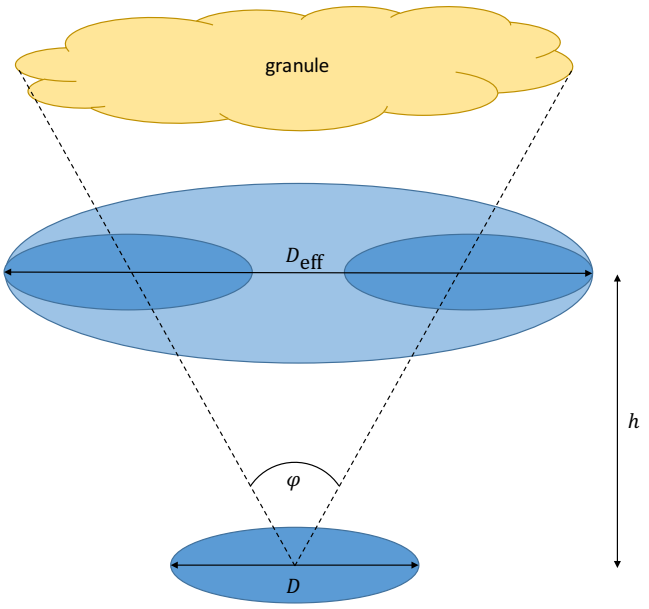

Figure 3.6: Cartoon showing how the effective pupil grows as a function of altitude when observing an extended object, of size φ. At a height h the pupil of diameter D grows to the size D_{eff}. This expansion of the pupil at altitude causes averaging of the turbulence sensed at these altitudes, reducing the slopes induced from high altitude turbulence.

given by;

$$D_{\text{eff}} = D + h\varphi, \tag{3.46}$$

where φ is the extent of the extended object in radians and h is the altitude of the projected pupil (D_{eff}).

Combining equations 3.44 and 3.45, we get the final form of the covariance, $\langle \delta x_1 \delta x_2 \rangle$;

$$\langle \delta x_1 \delta x_2 \rangle = \sum_{n=1}^{N} 0.358 \lambda^2 r_0(h_n)^{-5/3} D_{\text{eff}}(h_n)^{-1/3} F_x(s, \alpha, h_n), \tag{3.47}$$

where,

$$F_x(s, \alpha, h_n) = \frac{1}{2} I\left(\frac{\alpha h_n - s}{D_{\text{eff}}}, 0\right) + \frac{1}{2} I\left(\frac{\alpha h_n + s}{D_{\text{eff}}}, 0\right) - I\left(\frac{\alpha h_n}{D_{\text{eff}}}, 0\right). \tag{3.48}$$

This can be used to generate theoretical covariance functions for a single layer at a known altitude, in a similar manner to response functions for SLODAR. Some example response functions for S-DIMM+ are shown in Fig. 3.7. The x axis shows increasing field separation of the guide sources and the y axis represents the physical

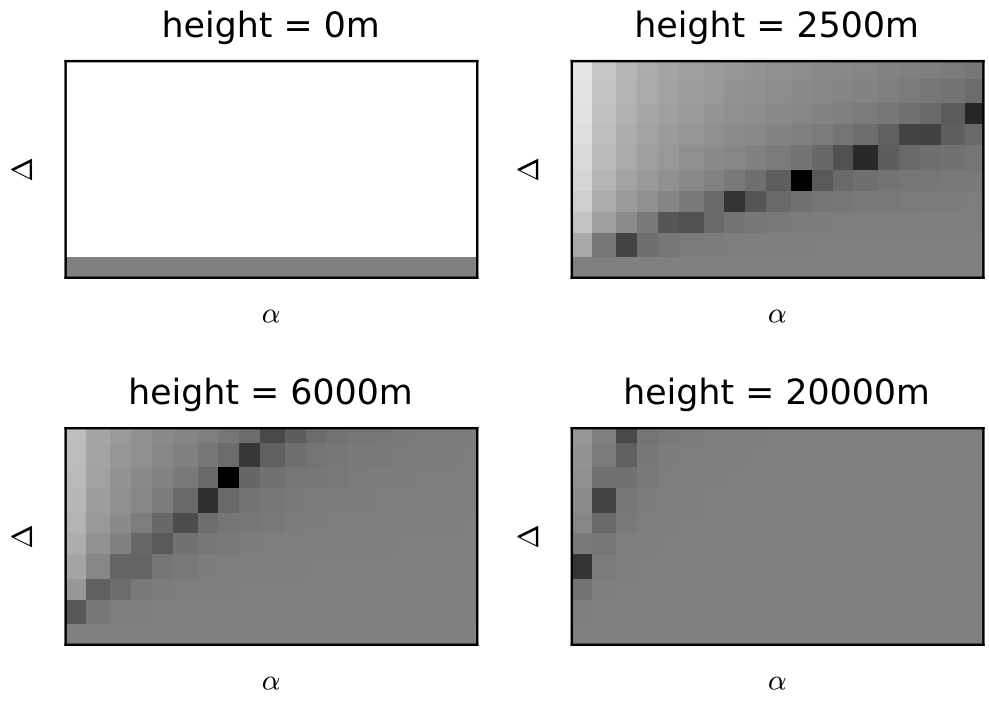

Figure 3.7: Theoretical covariance functions for single layers of turbulence at given altitudes. The heights chosen are the ground, 2.5km, 6km and 20km. Δ corresponds to spatial sub-aperture seperation and α corresponds to angular field seperation of the guide sources. The turbulent layer leaves a dip in the differential motion, which can be seen as the dark diagonal line in the response functions.

separation of the sub-apertures in the pupil. When sub-apertures overlap at a turbulent layer the centroid induced on the layer is idential for both sub-apertures, which is apparent as a darkening in Fig. 3.7.

The altitude resolution of the S-DIMM+ is limited by the effect of the expanding pupil. The resolution close to the ground is good, and decreases at higher layers as the effective pupil diameter, D_{eff} increases. The chosen altitudes of the covariance functions used in the S-DIMM+ in Scharmer and van Werkhoven (2010) was 0.0, 0.5, 1.5, 2.5, 3.5, 4.5, 6.0, 9.5, 16, and 30 km.

3.6 Other Atmospheric Profiling Methods

There are many other optical methods for measuring the atmospheric profile both during the day and at night, some of which are mentioned here.

In the day there are other methods for sensing the altitude distribution of turbulence not discussed so far. One such method to measure turbulence profiles is suggested by Waldmann et al. (2007, 2008). This is a method similar to S-DIMM+, but uses fewer sub-apertures and many more field directions to estimate the atmospheric profile. There also exists a method which utilises the differential motions of images in multiple telescopes observing solar granulation to increase the resolution of turbulence profile (En et al., 2015).

There are also a number of instruments which measure the effects of scintillation, rather than the gradient of phase of the turbulence. These include SCIDAR (Rocca et al., 1974), and more recently Generalized SCIDAR (Avila et al., 1997) and Stereo-SCIDAR (Shepherd et al., 2014) for night time turbulence profiling. These rely on the interference of the aberrated wavefront as it propagates, generating "scintillation patterns". By imaging the telescope pupil, the scintillation pattern is captured. A triangulation technique, similar to SLODAR can then be used in order to estimate the turbulence profile.

A form of SCIDAR can also be employed during the day. This includes Solar SCIDAR (Miura et al., 2013), which directly applies the SCIDAR technique to the solar surface, with modifications for the expanding pupil and SHABAR (Beckers et al., 1997), which measures the scintillation from the whole solar disk over a range of different baselines.

3.7 Summary

In this chapter I have described the statistics of atmospheric turbulence, and how it can be measured. The methods described are based on measuring the gradient of the phase, through image motion, rather than the phase directly. This allows SH-WFSs to be used to sample the turbulence. I have also shown how sub-sampling the pupil and using triangulation the turbulence profile can be measured with SLODAR and S-DIMM+. The SLODAR technique is used later in chapter 6, where it is extended for use in solar observations. Finally I briefly mentioned some other techniques and instruments which can be used to measure the turbulence profile, including techniques which measure scintillation across the telescope pupil.

Chapter 4

Optimised Center of Mass for Correlation Wavefront Sensing

In solar WFSs cross-correlations with center of mass measurements, or polynomial fitting is used to measure the sub-aperture shifts. The centroiding methods on the correlation images are subject to noise in the correlation image, which can shift the location of the correlation peak. Even a perfect measurement of the location of the peak of the correlation image will be subject to this noise, so we refer to it as extrinsic noise. The accuracy of the peak location using a centroiding method also has a noise term associated with it, which we call intrinsic noise. There is some optimal set of centroiding parameters which will minimise the effects of these terms. In this chapter I describe a method for measuring the performance of a given set of centroiding parameters using WFS images which can then be used to choose the optimal parameters for centroiding.

4.1 Simulation

The high resolution image of solar granulation shown in Fig. 2.6 is down-sampled by a factor of 10 to generate sub-aperture images that can have sub-pixel shifts of 1/10 of a pixel. Regions of 240×240 pixels are selected for the sub-aperture

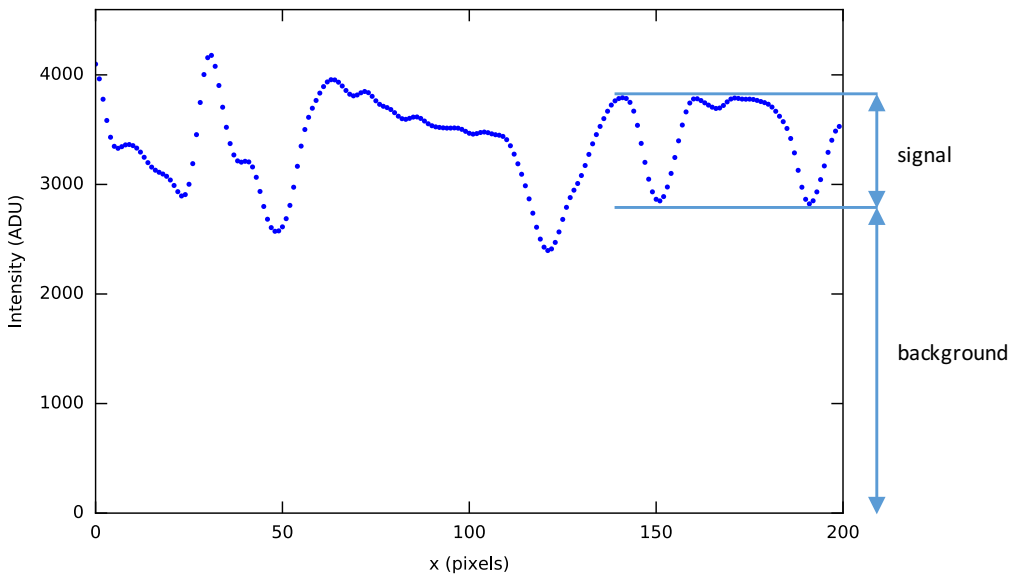

Figure 4.1: A slice through the solar granule image shown in Fig. 2.6, showing the intensity fluctuations due so solar granules. Due to the high background level seen in images of solar granulation the SNR is defined differently to Poisson noise. The signal is taken to be the level above the background of the image, and the noise is taken to be the Poisson noise on the image. This reduces the SNR significantly compared to Poisson noise.

images, which generate sub-aperture images of 24×24 pixels, with an image scale of $0.4''$/pixel. This is similar to the pixel scales used in current solar AO systems (Schmidt et al., 2014; Scharmer et al., 2002). All simulations were performed using the Python programming language, using numpy and scipy routines (Van der Walt et al., 2011) and astropy (Robitaille et al., 2013). Plotting and data visualisation was created using the matplotlib plotting library (Hunter, 2007).

The high light levels in solar WFSs are dominated by shot noise. To mitigate this sensors with large full well depths ($\sim$ 40000 electrons) are used. However noise is solar images manifests more seriously than Poisson noise for night-time astronomy. A solar WFS images low contrast granules ($\sim$ 10%) on a bright background. This is illustrated in Fig. 4.1. For camera pixels with a typical full well depth of 40000 electrons; the signal would be 4000 electrons (corresponding to 10% contrast), with

photon-noise from 40000 electrons, giving a SNR of;

$$\frac{\text{signal}}{\sqrt{\text{Full well depth}}} = \frac{4000}{\sqrt{40000}} = 20. \tag{4.1}$$

Therefore shot noise is still significant in solar WFSs.

The shifts induced between the different sub-aperture images was taken from a Gaussian distribution to give the same statistics as Kolmogorov turbulence (see § 3). The simulated data, along with the known shifts applied to each of the sub-aperture images then allows for the accuracy of various centroiding techniques to be investigated and compared.

4.2 Estimating Error on Centroid Measurements

There will be an optimal set of centroiding parameters for any given image and SNR that leads to optimal image shift estimates. The variable nature of solar granulation prevents the derivation of an analytical route to determine these optimal parameters. Instead, we propose measuring the error on the measured image shifts and using this to identify the optimal centroiding parameters through parameter space exploration.

With on-sky data, the absence of the exact shift data mandates a method of experimentally estimating the error. Here we give a method for estimating the error on centroid estimates using multiple reference images on a set of sub-aperture images. In order to make the different estimates directly comparable, the effect of global tip/tilt on the set is removed. This is because the reference images are taken from the set of sub-aperture images, and so have different relative shifts. The global tip/tilt term can be removed by setting the average x and y shifts to 0 for the set of sub-aperture images;

$$\mathbf{R}^r_{t/t} = \mathbf{R}^r - \langle \mathbf{R}^r \rangle_r \,, \tag{4.2}$$

where $\mathbf{R}^r_{t/t}$ is the matrix containing a series of x and y centroids using reference image r. $\mathbf{R}^r$ are the raw centroids measured, and $\langle \mathbf{R}^r \rangle_r$ is the vector containing

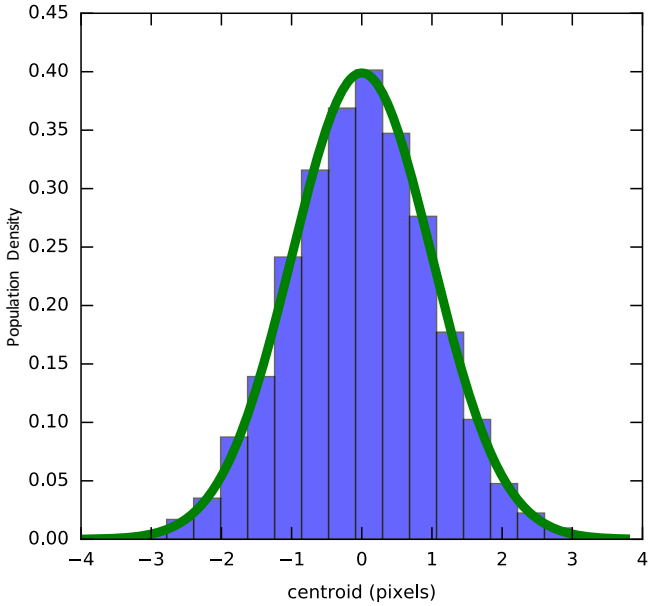

Figure 4.2: A normalised histogram showing the distribution of centroid estimates for a sub-aperture image with a shift of 0 pixels. The histogram is shown in the blue boxes, with a Gaussian fit to the histogram shown in green. The standard deviation of the distribution gives an indication of the error on the centroid estimates for the centroid parameters used.

the average centroids in the x and y directions.

If we look at a single sub-aperture, with the multiple estimates of its centroid, we expect to see a distribution like in Fig. 4.2. The width of the distribution gives an estimate of the error of the centroid estimates. An example of the distribution of a good set of centroid parameters is shown in Fig. 4.3. As the distributions follow a Gaussian shape, a good estimate of the width is to use the standard deviation of the different centroid estimates, described by;

$$\mathbf{R}_{\text{error}} = \sqrt{\frac{1}{N}\sum_{i=1}^{n}(\mathbf{R}_{t/t}^{i} - \mathbf{R}_{t/t}^{\text{mean}})}, \tag{4.3}$$

where $\mathbf{R}_{\text{error}}$ is a matrix containing the error estimate for each sub-aperture in the x and y directions, N is the total number of different reference images, and $\mathbf{R}_{t/t}^{\text{mean}}$ is the matrix containing the average centroid from the different reference images, for each of the sub-aperture images.

Depending on the number of different reference images used, the estimates of error

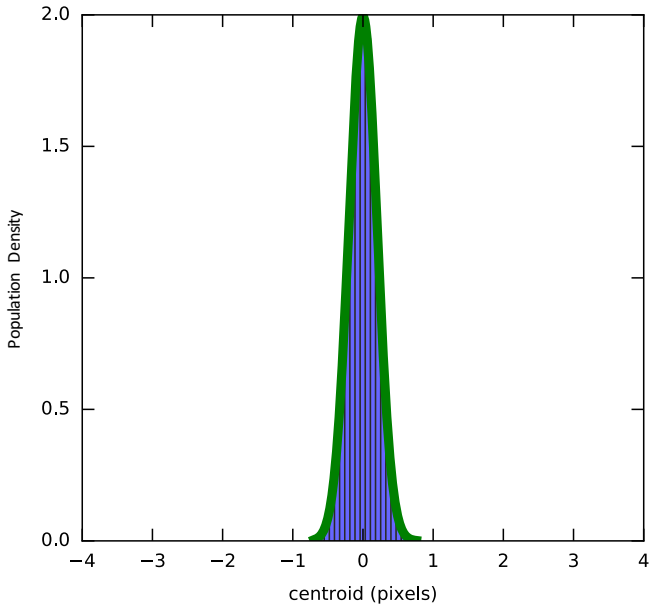

Figure 4.3: A normalised histogram showing the distribution of centroid estimates using optimal window and threshold parameters. The width is much narrower than seen in Fig. 4.2, where a large window and no threshold was used. The narrower width of the distribution shows the centroiding parameters are better than the ones used in Fig. 4.2.

on the individual sub-apertures is likely to be very noisy. However they are all derived from the same threshold and window parameters on the center of mass used to measure the location of the cross-correlation peak. While each estimate may be noisy, the ensemble of estimates should give a good estimate of how the parameters chosen perform. So an estimate of the error on the set of sub-aperture images, for a given set of centroiding parameters can be derived by averaging all of the individual error estimates;

$$\sigma^{w,\alpha} = \bar{\mathbf{R}}_{\text{error}}, \tag{4.4}$$

where $\sigma^{w,\alpha}$ is the error estimation for the set of sub-aperture images using a window size w, and threshold value of α. Using this approach it is possible to explore the parameter space defined by w and α, then assess which pair of values gives the best estimates of the real centroid. For the simulations that follow 10 seperate sub-aperture images are used as reference images, and the estimates of error on the centroid estimate taken from their statistics.

4.3 Optimised Windowed, Thresholded Center of Mass

There will be an optimal value for the thresholding level, α, and the size of the window, w, that gives the best centroid estimate for a set of cross-correlation images. The optimal values for these two parameters will depend on the size, shape and SNR of the cross-correlation peak. We can explore the performance of different α, and w values using the error estimation technique shown in § 4.2, using only the sub-aperture images themselves, and then select the centroiding parameters which yield the most accurate centroid estimates.

The size of the window is a relatively small parameter space to explore, going from a single pixel of the cross-correlation image (corresponding to an integer shift measurement), to including the full wings of the cross-correlation peak. If a larger window is used a drop off in performance will be seen, as more noise is included in the centroid estimate without any extra useful information about the location of the peak. The optimum window size is chosen as a trade off between including as much of the correlation peak as possible, but also minimizing the number of pixels which contribute only noise to the measurement.

The threshold level behaves similarly to the window size, in that having a lower threshold, which uses more pixels, increases the noise included in the centroid measurement and reduces its accuracy. Using a high threshold, which reduces the number of pixels included, gives rise to a bias towards integer shift measurements, similar to that seen in the 2nd order polynomial fit (§ 2.2.2.3). The optimum threshold value lies somewhere between these two regimes, and is liable to change depending on the size of the window selected. This means the whole parameter space needs to be explored, for all window sizes and threshold values, to identify the best combination of parameters for centroiding the cross-correlation images.

The parameter space created by w and α for a given set of images can be explored

relatively easily as the cross-correlation images only need to be generated once. This means the increase in the computational effort required to find the optimal centroiding parameters scales as $O(N)$, rather than the computational cost of generating cross-correlation images, which scales as $O(N^2 \log_2(N))$, making it feasible for use in real time. It also allows the method to be used with on-sky data from a WFS without any external input.

The optimum set of parameters will depend on a number of different obvious factors, including the image shape, the shape of the resulting correlation function, and the SNR of the sub-aperture images. There is no obvious analytical way to determine the best parameters for a given set of images, or circumstances, hence we explore the whole parameter space to find the optimal solution. Once the optimum set of centroiding parameters is found for a given object, at a set SNR level, then it should remain constant until one of these factors changes. This means after the optimal centroiding parameters have been found, they only need updating if something in the AO system changes, such as the shape of the images within the sub-aperture. In the case of solar AO the shape of the solar granulation changes typically on the order of a few minutes (Bahng and Schwarzschild, 1961). Given this timescale, a desktop class computer could augment a real time solar AO system by recomputing the optimal centroiding parameters and updating the real time control system on the order of once a minute.

4.4 Results

The full parameter space was explored in simulation for a range of α values and w sizes for a center of mass measurement of the cross-correlation images. How the error estimates compare with the actual errors measured on the centroids are shown in Fig. 4.4. Figure 4.4a shows the magnitude of the real residual errors for different parameters. Figure 4.4b shows the estimated error on the centroids using the multiple reference image method. The optimal parameters from each of the

methods is highlighted with a white spot and the estimated optimal parameters are highlighted on the actual errors with a white cross. The estimation technique can be seen to give a good estimation of the error on the centroids, as both parts of Fig. 4.4 show similar shapes. As seen in Fig. 4.4, the optimal parameters chosen by the error estimator differs somewhat from the actual optimum, however this translates to a very small difference in error on the centroid. This is expected given the plateau-like nature of the optimal region of the parameter space.

In the α axis (x) of Fig. 4.4 it is possible to see the effects of aliasing at large α values (on the right of the plots). As too few pixels are used to estimate the location of the cross-correlation peak the estimate is biased towards the integer location of the brightest pixel. The extreme is reached at a α value of 1, where only the brightest pixel is used for the estimate, making the estimate the integer value of the brightest pixel.

In the w axis (y) of Fig. 4.4 the structure is more complicated. Initially the aliasing is apparent for small window sizes, where the estimates are biased towards integer pixel centroids. This problem decreases as the window size increases, until its optimal region. However the performance begins to degrade again for large windows with small α values. This happens where the region is so large that as well as including all of the cross-correlation peak, it includes increasing amounts of noise, which isn't filtered out by the thresholding as the value of α is too low.

4.4.1 Optimal Parameters for Varying SNR Levels

The centroid optimisation was performed for a range of different noise levels (using photon-noise) to demonstrate how noise on the sub-aperture images affects the optimal centroid parameters, and estimates. The parameter's dependence on SNR is shown in Fig. 4.5. Figure 4.5a shows how α affects the accuracy of the centroid estimates, and Fig. 4.5b illustrates how changing the window size affects the accuracy of the centroid estimates.

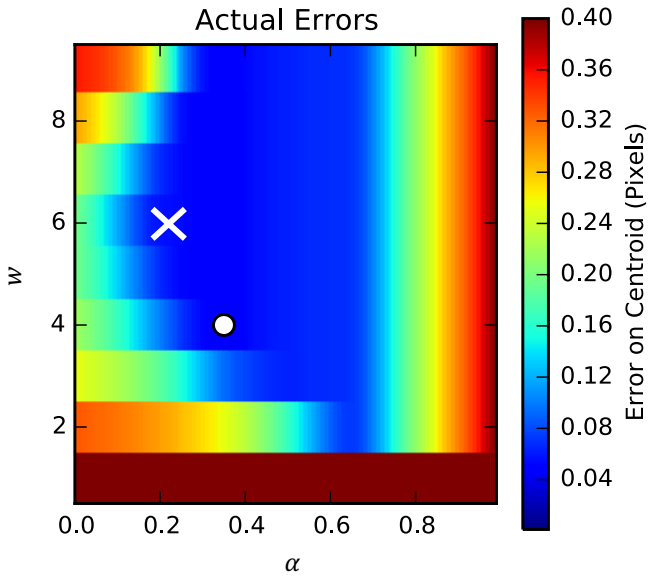

a

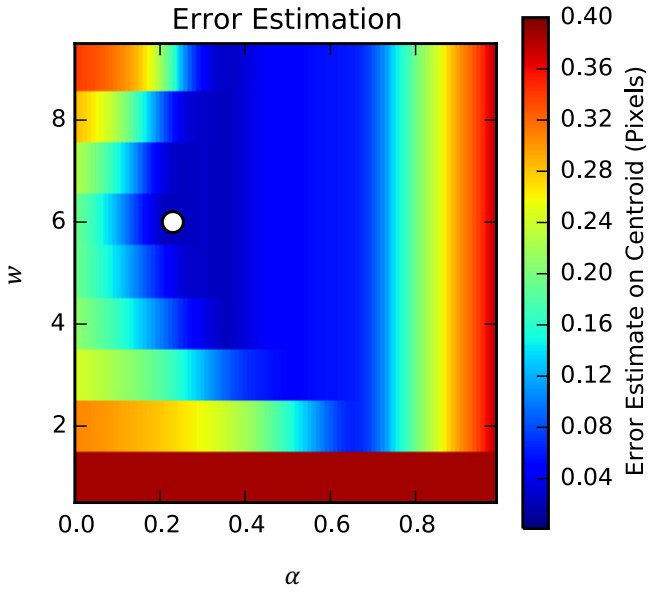

b

Figure 4.4: The error in the centroid measurements for a set of correlation images, visualised across the parameter space of the centroider. Subfigure a shows the real error associated with the parameters used in the center of mass, and Subfig. b shows the estimated error. The shape of the two plots is similar, indicating the error estimation technique is valid. The white spots on the plot show where the minimum lies in the parameter spaces. The estimated error position, shown as an x on the real errors, does not directly overlap with the location of the real minima, but it can be seen that the difference in error is minimal.

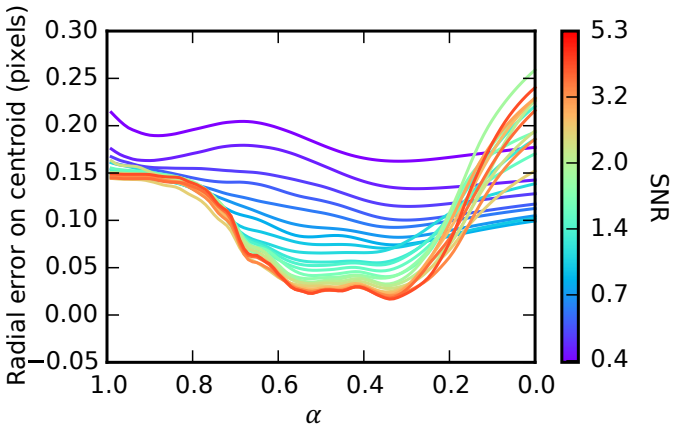

a

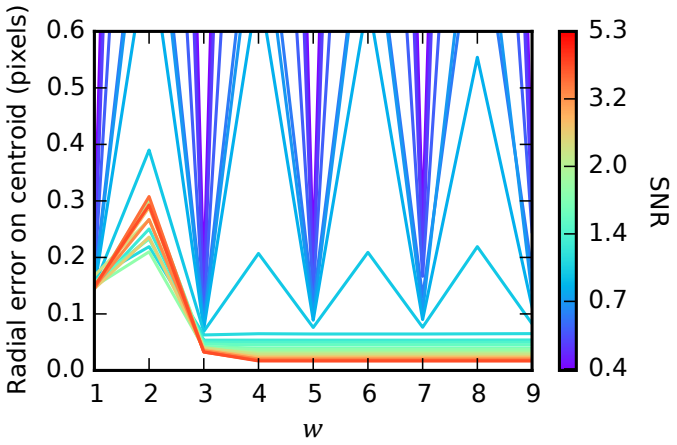

b

Figure 4.5: Subfig. a shows how the optimum threshold value is affected by different SNRs. The location of the optimal threshold values changes depending on the SNR, converging on a value of ~ 0.35 for high SNR sub-aperture images. Subfig. b shows how the window size affects the error on the centroid estimate for different SNRs. At low SNR the error is dominated by aliasing. For high SNR the window size has a minimum value of 4 pixels, but using larger windows doesn't degrade the accuracy of the centroid estimate.

The α values have a large effect on the accuracy of the centroids, and is best seen on the higher SNR (shown in red in Fig. 4.5). The location of the minima depends on the SNR level, highlighting that the optimal parameters for one set of sub-aperture images, taken at a certain time, is not likely to be the optimal set of parameters for another set of sub-aperture images, taken at a different time.

The optimal values found for the w and α parameters with varying SNRs is shown in Fig. 4.6. Figure 4.6a shows the optimal thresholding values for the various SNR levels, both the optimal value and the estimated value. Figure 4.6b shows the value of the optimal and estimated window sizes.

The α values are overestimated for low SNR. This can be explained to some extent by the corresponding estimated window size. The window is large, so the threshold value will also be large, to remove more pixels from the windowed region of the cross-correlation image. This is mirrored in the true optimal parameters, between SNRs of 1 and 10. Here the window size increases, from 2 pixels to 5, and the thresholding value also jumps up to remove more of the pixels in the windowed region. Finally both the true optimal values and the estimated optimal centroiding parameters converge on a value for high SNR sub-aperture images.

When the window is small, or the threshold value is high, the center of mass measurement suffers from the same problem as the 2nd order polynomial fit. These values for the parameters restrict the number of pixels used by the center of mass to estimate the location of the cross-correlation peak. This biases the centroid estimates towards integer pixel centroid measurements. In low SNR conditions these parameters may still be optimal, as the effect of including more noise in the centroid estimate can cause a larger error than the bias from undersampling the cross-correlation peak.

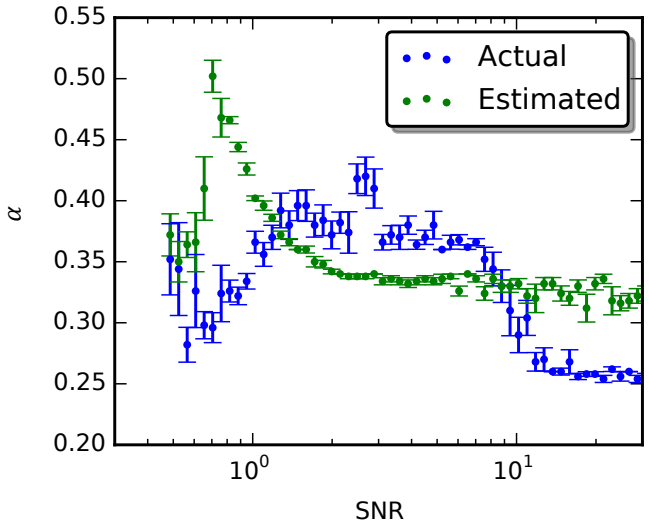

a

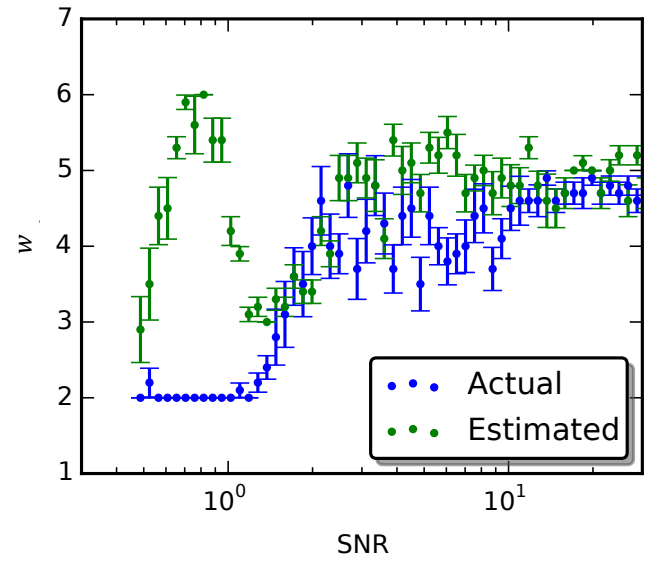

b

Figure 4.6: Subfigure a shows the optimal α values, for both estimated and actual parameters, with different SNR sub-aperture images. Initially the estimated threshold is high, to remove as much noise as possible from the correlation image, then the threshold value drops to its optimum value for high SNR images. Subfigure b shows the window size for the different SNR levels. This shows a similar trend, of increasing window size at high SNR, using more pixels when the noise is reduced. At low SNR the estimated parameters disagree with the true optimal parameters, but this disagreement is compensated for to some extent by an increase in the threshold value.

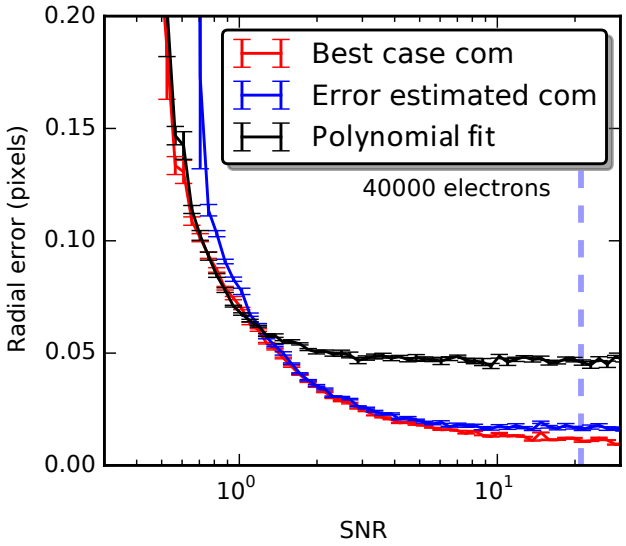

Figure 4.7: Performance of the optimal center of mass (com), estimated parameters for the center of mass, and the 2nd order polynomial fit for a range of different SNR. It can be seen above a SNR of 1 the windowed, thresholded center of mass outperforms a 2nd order polynomial fit. The 2nd order polynomial fit tapers off in performance at 0.05 pixel error, whereas both the windowed center of mass methods taper off at much lower errors. The vertical line on the plot show the expected SNR for solar granule sub-aperture images with a contrast of 10%, and a camera with a full well depth of 40000 electrons. It can be seen that the performance from estimating the errors on the center of mass is worse than the optimal case, but still outperforms the 2nd order polynomial fit for high SNR levels, and achieves close to optimal performance.

4.4.2 Comparison to a 2nd Order Polynomial Fit

The application of a 2nd order polynomial fit to the core 3×3 pixels in a correlation image is a typical centroiding method employed by Solar AO systems (Löfdahl, 2010). This method has no free parameters and samples a small region of the correlation peak which suggests it will be optimal for only a sub-set of conditions. Here I compare the 2nd order polynomial fit to the optimised center of mass for both estimated and actual optimal parameters in Fig. 4.7 for a range of different SNR levels.

For high SNR levels, both center of mass methods outperform the 2nd order polynomial fit to the cross-correlation peak. This is due to the center of mass properly

sampling the peak, when the 2nd order polynomial fit under-samples it giving a bias towards integer pixel centroids. There is a noticeable difference between the performance of the optimal center of mass and the center of mass where the threshold and window size are estimated. This error comes from choosing the wrong parameters for the center of mass in Fig. 4.4.

In low SNR the 2nd order polynomial fit and the optimal center of mass give similar errors on the centroids. However, the center of mass using the estimated parameters gives a larger error. In this region both the center of mass and the 2nd order polynomial fit suffer from the effects of noise in the reference images beginning to dominate the cross-correlation image. The center of mass using the estimated parameters doesn't perform as well as the optimal center of mass due to these noise sources going unsensed with the error estimation technique.

4.4.3 Sources of Error in the Parameter Estimation

In order to understand the inaccuracy of our error estimation technique at low SNR we need to consider the propagation of noise through the centroiding algorithm and how this impacts our error estimation method. The simulations operate in a regime where non-common image noise (see chapter 5) can be ignored, leaving the main source of error as shot noise. As described in equation 2.22 this results in four terms; $C_{Im_s Ref_s}$, $C_{Im_s Ref_\sigma}$, $C_{Im_\sigma Ref_s}$, and $C_{Im_\sigma Ref_\sigma}$.

If we assume that the contribution of $C_{Im_\sigma Ref_\sigma}$ is negligible, then the two remaining error terms which affect our estimate of the centroid are the cross terms. The method for estimating the error on the centroid estimates uses multiple reference images. When estimating the error on the centroid estimates for a given set of parameters the effect of the different reference images is averaged out. This has the effect of averaging out the $C_{Im_s Ref_\sigma}$ term. This term begins to have a noticeable effect at low SNR, as can be seen in Fig. 2.11. As the technique of estimating the error on centroids is insensitive to this noise term, the estimation of the center of

mass parameters is not reliable at low SNR, causing the error on the centroids to be larger than the optimal values.

There are other methods for estimating the error of a centroid on an extended object, such as Saunter (2010), which don't have this problem of being insensitive to the $C_{Im_s Ref_\sigma}$ term in the cross-correlation image. However this technique relies on over-sampled images in order to de-interlace the cross-correlation images and give two separate centroid estimates for each sub-aperture image. Over-sampled images are readily available in biological imaging, where the technique is shown to work, but are generally avoided in AO systems, as they increase data rates and computation time in systems which have large temporal constraints.

4.5 Estimating Center of Mass Parameters on Laser Guide Star Wavefront Sensors

Some LGS WFS use cross-correlation techniques to measure centroids. The method of estimating the error on centroids suggested here should be equally valid on the cross-correlation images from a LGS WFS as they are for solar WFS. Due to the different elongation and orientation of the laser plume in each sub-aperture (as described in §2.1.1), it is not possible to combine different sub-aperture images in a single WFS frame. Instead each sub-aperture needs to be treated separately, and the multiple images be taken from a time series of WFS frames.

This requires the sodium profile to be stable over the period of the data set, to allow the optimal parameters to be estimated, and then applied to subsequent centroid measurements. One advantage of doing the optimisation over a time series of sub-aperture images is that each sub-aperture can be optimised independently. It could be possible that the parameters which work best on a slightly elongated cross-correlation image for sub-apertures close to the laser launch location will be different to the ones which are on the opposite side of the pupil, with the largest values of elongation.

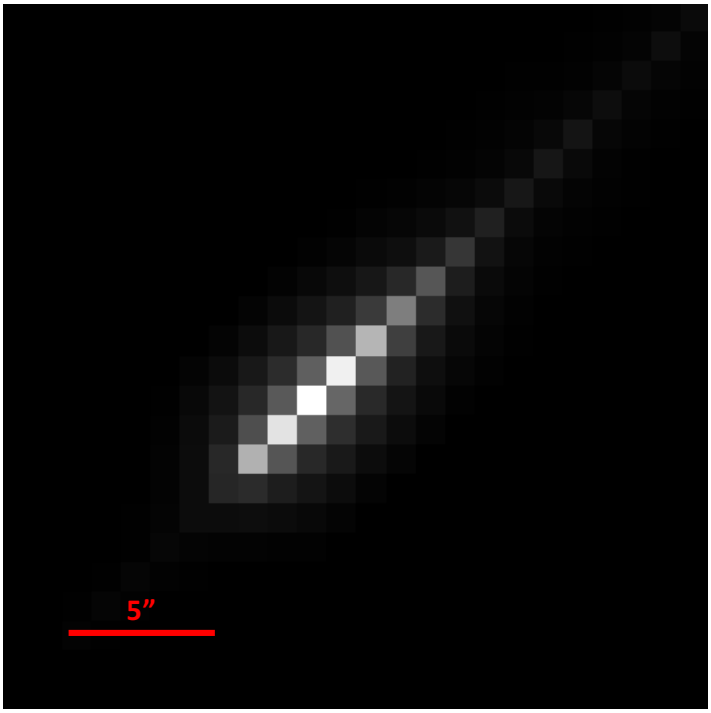

Figure 4.8: An example WFS frame for the most elongated sub-apertures on an E-ELT. The image hasn't had any noise added or atmospheric turbulence applied. The image has a pixel scale of 1″/pixel and the visible tail of the sodium plume spans more than 12″.

As with our simulation on solar granulation, a set of WFS images that contain sub-pixel shifts can be simulated by shifting and binning full resolution profiles, taken in this case from Pfrommer and Hickson (2014). An example sub-aperture image is shown in Fig. 4.8. It is 24×24 pixels and has a pixel scale of 1″/pixel, to simulate one possible WFS configuration for the LGS WFS in CANARY (Gendron et al., 2011).

The results of the error estimation, along with the real error on the centroids from the known shifts, are shown in Fig. 4.9. Both the real error on the centroids (Fig. 4.9a) and the estimated error on the centroids using multiple reference images (Fig. 4.9b) have similar shapes. This shows the robustness of the error estimation, as although the shape of the parameter space is very different to the one from centroiding images of solar granules (Fig. 4.4), the technique gives accurate estimates for the errors. This allows us to estimate the best parameters for centroiding

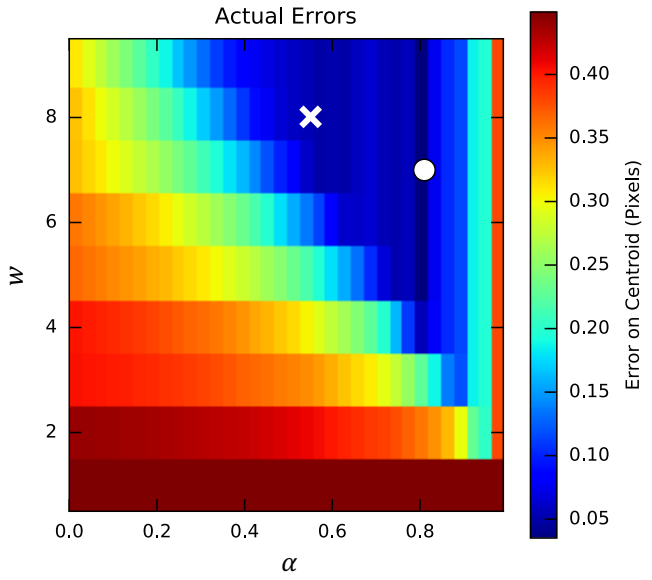

a

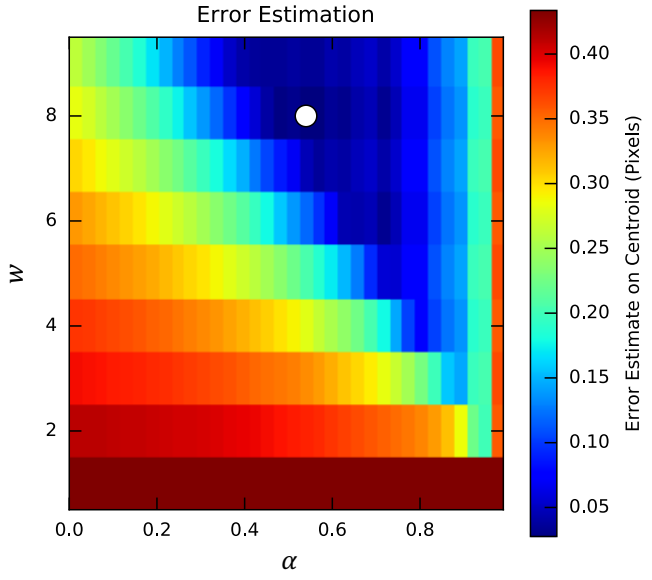

b

Figure 4.9: Subfig. a shows the real error on centroid estimates with given threshold and window parameters, with a cross showing the location of the estimated centroiding parameters. Subfig. b shows the error which is estimated using multiple reference images. The white spots show the minima for each plot. The locations of the white cross and spot on Subfig. a are close and in the plateau region of the best centroid parameters.

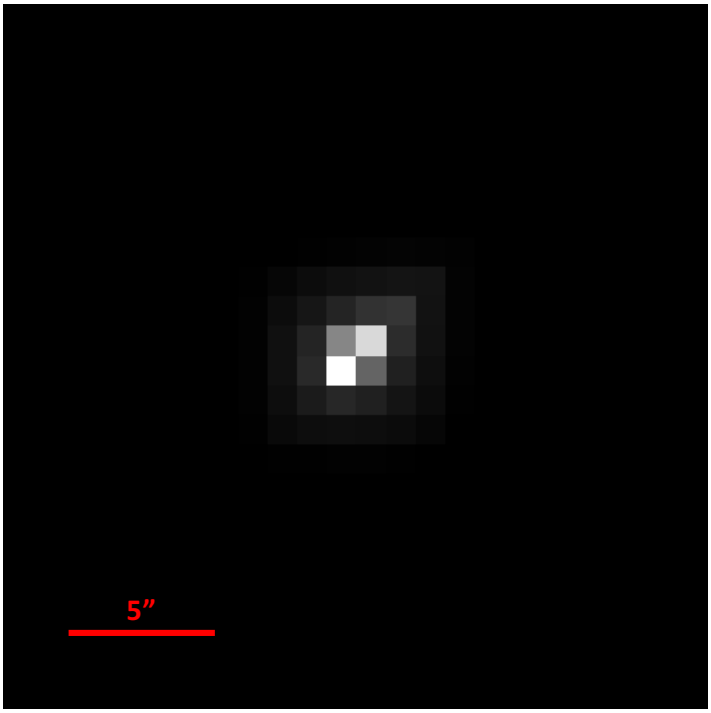

Figure 4.10: This image has the same characteristics as the WFS simulated in Fig. 4.8, but is a different sub-aperture much closer to the laser launch, only 2.8m away. This gives a much smaller value for the elongation, which can be seen as the image of the LGS is spread over fewer pixels than the LGS image in Fig. 4.8.

by exploring the parameter space.

4.5.1 Comparison of Different Elongations

The optimal centroiding parameters depend on the noise of the images used. This is especially relevant to LGSs as the noise characteristics of each sub-aperture will be different, due to the different elongations of the laser in them. An example of a LGS WFS image for a sub-aperture with much less elongation is shown in Fig. 4.10.

The same optimisation routine was performed on frames from this less elongated sub-aperture. Due to the large difference in the shape of the images in the sub-aperture, the size, shape, and noise characteristics of the cross-correlation is very different. This changes the optimal centroiding parameters for this sub-aperture.

The parameter space for Fig. 4.10 is shown in Fig. 4.11.

The location of the optimal centroid parameters is estimated well, as can be seen by the agreement of the location of the minima in Fig. 4.11. The shape of the parameter space for this much less elongated LGS has similarities with the more elongated ones (Fig. 4.9), but also is different in that the error on shift estimate is low for very low threshold parameters, whereas it gets large for the more elongated LGS images. This shows how the optimal centroiding parameters found are heavily dependent on the shape of the sub-aperture images being cross-correlated, and aren't universal.

This optimisation was performed for a range of different SNRs, on both of the LGS shapes shown previously (Fig. 4.8 and Fig. 4.10). The results are shown in Fig. 4.12. It should be noted that the SNR values for the LGS sub-aperture images are calculated differently to the way it was for the images of solar granulation. As the background of the sub-aperture images is 0, there is no need to calculate the SNR with respect to a high background. The SNR is then calculated using Poisson statistics, giving a SNR of $\sqrt{\text{signal}}$.

4.6 Future Work

This method has only been used to explore a windowed, thresholded center of mass, with the cross-correlation images generated using the covariance function. It would be interesting to explore the other methods of generating cross-correlation images in order to see if the method still is able to select optimal parameters. The results of this could be used to compare the performance of different centroiding techniques, for instance the "brightest pixel selection" centroider (Basden et al., 2012).

There are also a lot of unexplored avenues with using this technique on LGS WFSs. While a selection of different LGS elongations are presented here, a full analysis of a WFS observing a LGS, with each sub-aperture analysed independently would be

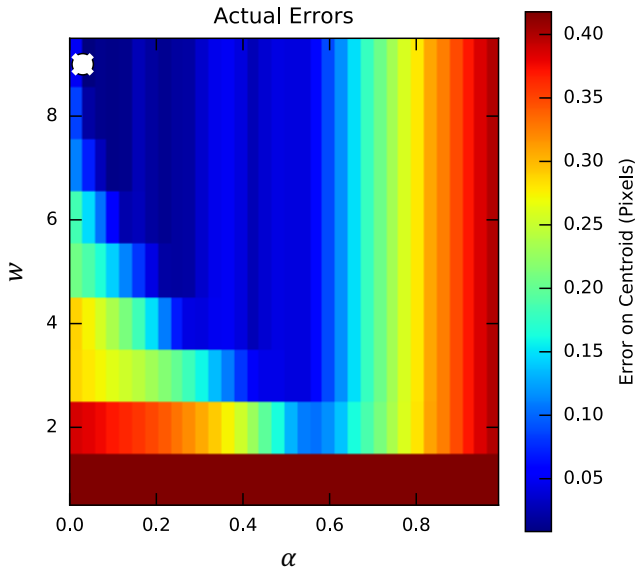

a

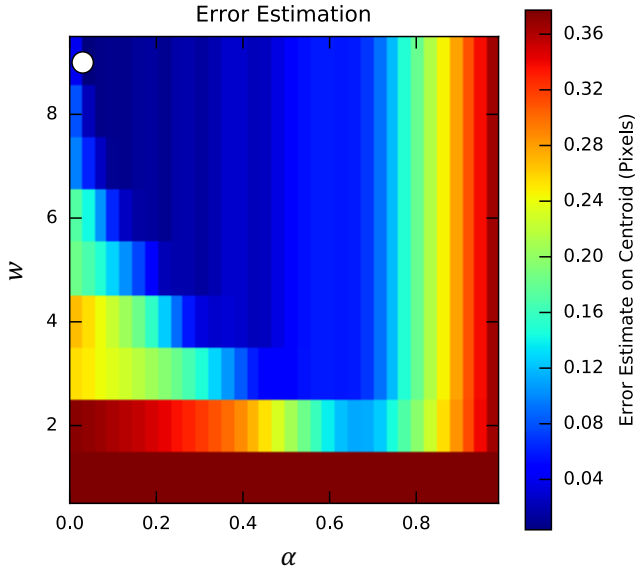

b

Figure 4.11: Subfigure a shows the real error on centroid estimates for given threshold and window parameters, and Subfig. b shows the error which is estimated using multiple reference images. The white spots show the minima for both plots and the white cross shows the location of the estimated centroiding parameters on Subfig. 4.11a. The shape and estimate of the optimum parameters for centroiding agree well, however the shape of the parameter space is quite different to the one for a much more elongated LGS (Fig. 4.9).

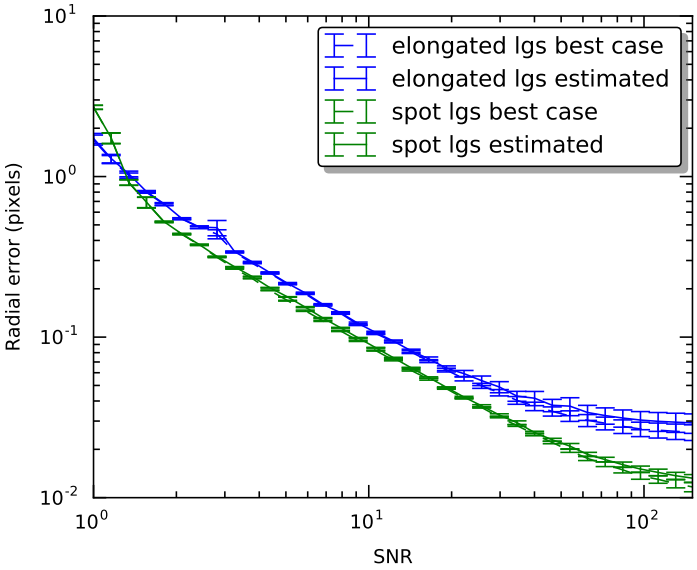

Figure 4.12: Performance of optimal center of mass, and the estimated parameters for the center of mass for elongated LGS sub-aperture images. Both curves have similar performances, and the estimated parameters perform as well as the actual optimal values. Above a SNR of 2 both elongations give centroid estimates that have better than a 1 pixel error.

useful. As the elongation seen in every sub-aperture is different, this optimisation should be done for every sub-aperture independently.

4.7 Summary

In this chapter I have presented a way of estimating the error on centroid measurements which can be applied to real WFS images. This allows the performance of a windowed, thresholded, center of mass measurement to be assessed for different sets of parameters, and the full parameter space to be explored. From this the optimal centroiding parameters can be selected for any given input sub-aperture images.

This method has also been shown to work on simulated LGS images, with the optimal parameters changing for different LGS elongations. This demonstrates the technique to be useful outside of solar WFS, and demonstrates the need to

explore the parameter space for the particular structure of the sub-aperture, as the parameter spaces change dramatically depending on the content of the sub-aperture images. It also shows the versatility of the method, as it works on a variety of input sub-aperture images, which have different optimal centroiding parameters.

Chapter 5

Supersized Reference Images for Correlating Wavefront Sensors

When the shifts in FOV induced by atmospheric turbulence between sub-apertures in a WFS are large, the different structure entering and exiting the sub-apertures adds non-common image noise to the cross-correlation images, adding noise to the centroid estimates. One way of reducing this is to increase the size of the reference image. This increases the overlap between the sub-aperture image with the reference image, reducing the non-common elements in the sub-aperture image.

In this chapter I describe a technique for generating a supersized reference image from WFS data, and assess its performance compared to reference images of a similar FOV to sub-aperture images. In § 5.1 I introduce how a supersized reference image can reduce noise in centroid estimates for pairs of images with large relative shifts. I present a method for estimating the shifts of a set of images with large shifts in § 5.2 and how these estimates can be used to construct a supersized reference image in § 5.3. In § 5.4 I show the results of simulating a solar WFS and using a supersized reference image to estimate centroids and in § 5.5 I show how this method can be used on images of elongated LGS. Finally in § 5.6 I describe avenues of further investigation of the technique and summarise the method and my results in § 5.7.

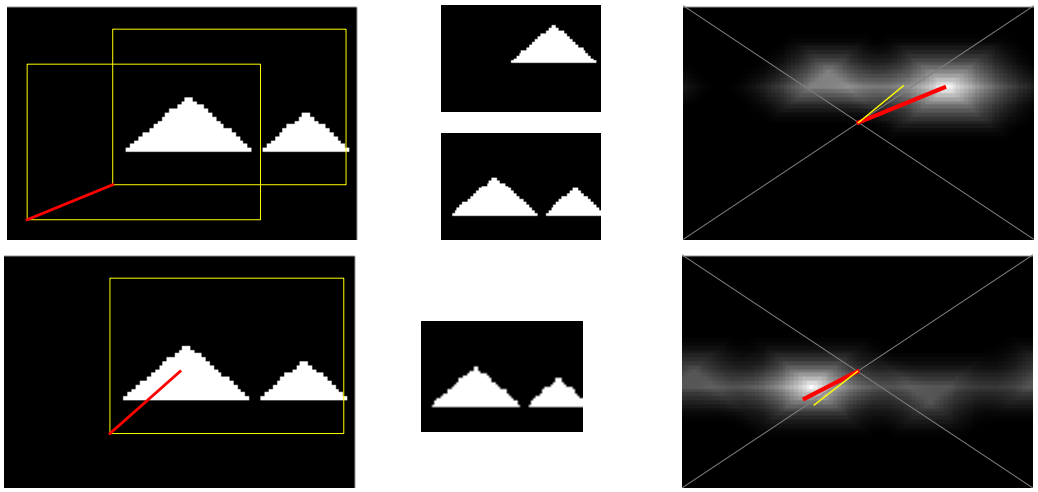

Figure 5.1: Concept of how a supersized reference image can reduce noise in estimating image shifts. The upper section is the same as the lower part of Fig. 2.12 and shows two images with shifted FOVs with a demonstration of how a correlation method estimates their shift. The lower part shows the situation if the whole region is taken as the reference image, as would be the case for a supersized reference image. The left section shows the full FOV with the yellow boxes highlighting the FOV of a sub-aperture and the red line indicating the shift between them. The middle section shows the sub-aperture images in isolation and the right section shows the cross-correlation image generated, with the red line showing the true shift of the images and the yellow line showing the centroid estimate.

5.1 Concept

The concept of using a supersized reference image to reduce non-common image noise is illustrated in Fig. 5.1. By modifying the lower section of Fig. 2.12, and using the whole field as the reference image, we can in effect remove the non-common image noise.

The upper section of Fig. 5.1 shows the case where a normal correlating WFS will give a bad centroid estimate. The sub-aperture image (lower middle) has a feature which is not present in the reference image (upper middle). This adds an extra signal to the cross-correlation image which affects the centroid, moving it away from the actual peak of the cross-correlation image. By increasing the size of the reference image, the reference image contains all the features present in the sub-aperture image. This removes the erroneous signal present in the upper cross-

correlation image, allowing for a more accurate centroid measurement, as shown by the yellow and red lines appearing closer in the the lower section of Fig. 5.1.

It is possible to utilise the shift between individual sub-aperture images to generate a supersized reference image. As the observed FOV from different sub-apertures is different, due to the effect of atmospheric turbulence, a larger FOV is sampled for the series of images than is present in any of the individual sub-aperture images. These images can be combined, keeping all parts of all of the sub-aperture images, generating an image with a larger FOV than the individual sub-apertures observe.

This process will reduce the noise in the generated reference image, as well as increase its effective FOV. Looking at the combination of noise in the cross-correlation image, described in equation 2.22;

$$C = C_{Im_s Ref_s} + C_{Im_s Ref_\sigma} + C_{Im_\sigma Ref_s} + C_{Im_\sigma Ref_\sigma}, \tag{5.1}$$

we can see which of the terms will be reduced. C_{Im_σ,Ref_s} arises from noise in the sub-aperture images, making it random and unpredictable. C_{Im_s,Ref_σ} arises from noise in the reference image, so is the same for all centroid estimates and C_{Im_σ,Ref_σ} is a second order noise term, from the two noise terms combining.

The noise on the reference image is present in both the C_{Im_s,Ref_σ} and C_{Im_σ,Ref_σ} terms. By reducing these sources of noise, the resulting centroid estimates will be more accurate, even for small shifts between sub-apertures, where the effect of non-common image noise is not present. In the ideal case this would move the red line, corresponding to noise on both the sub-aperture and reference images, in Fig. 2.11 down to the blue line, corresponding to only having noise on the sub-aperture images. This effect is reduced in the higher SNR regimes, especially if global tip/tilt is removed, as the solid blue and red lines start to overlap when the SNR reaches a value of 11, so there is little advantage to this technique in high SNR regimes where the relative shifts are small.

5.2 Least Squares Centroider for Correlating Wavefront Sensors

The initial problem with creating a supersized reference image, using images from a WFS, is that a set of sub-aperture images with large differential shifts need to be aligned. The structure of atmospheric turbulence is continuous and so is the gradient of the turbulence. In a large set of sub-aperture images (taken from the same sub-aperture) there will be some sub-apertures with similar shifts to any given sub-aperture. This means they observe similar FOVs, which minimises the effect of non-common image noise for those pairs. This is true for every sub-aperture image and so makes a set of sub-aperture images a good candidate for using a least squares minimizer to estimate the centroids of each of the sub-apertures.

A least squares fit for centroids requires all sub-aperture images to be cross-correlated with all other sub-aperture images. This takes computationally longer than using a single reference image, but should allow for accurate centroid estimates of a set of sub-aperture images with large relative shifts. Here I describe how a linear least squares minimisation can be applied to a set of sub-aperture images. The differential shift of sub-aperture i with respect to sub-aperture j is denoted as $\mathbf{R}^{i,j}$. For a set of 3 sub-aperture images, the least squares problem would take the form;

$$\begin{pmatrix} +1 & -1 & \\ +1 & & -1 \\ & +1 & -1 \end{pmatrix} \begin{pmatrix} \mathbf{R}^0 \\ \mathbf{R}^1 \\ \mathbf{R}^2 \end{pmatrix} = \begin{pmatrix} \mathbf{R}^{0,1} \\ \mathbf{R}^{0,2} \\ \mathbf{R}^{1,2} \end{pmatrix}, \tag{5.2}$$

where $\mathbf{R}^i$ represents the absolute shift of sub-aperture i, and the matrix is a matrix of permutation factors, describing the combination of sub-aperture shifts in each centroid measurement. The measured centroids, $\mathbf{R}^{i,j}$ contain both the relative shift of i with respect to j and the associated error, $\sigma^{i,j}$;

$$\mathbf{R}^{i,j} = \mathbf{R}^{i,j}_{\text{signal}} + \sigma^{i,j}. \tag{5.3}$$

The least squares minimisation can be performed separately for the x and the y centroids. This should generate a set of centroids for the sub-aperture images which are more accurate than the technique of using one sub-aperture image as the reference image.

5.2.1 Weighted Least Squares Centroider

The least squares fit can be optimised further by adding a weight to the measured centroids to reduce the influence of centroid estimates with larger errors. The obvious choice for weight is the inverse of the magnitude of the measured centroid of a pair of sub-apertures, as this will work to minimise the effect of non-common image noise by suppressing the larger centroid estimates;

$$w^{i,j} = \frac{1}{\mathbf{R}^{i,j}}, \tag{5.4}$$

where $w^{i,j}$ is the weight applied to the centroid measurement $\mathbf{R}^{i,j}$. As the estimated centroid between two sub-apertures grows, the error from non-common image noise also grows, as a larger shift corresponds to the region of overlap of the two sub-aperture images growing smaller. The inclusion of a weight in the measured centroids modifies equation 5.2 to;

$$\begin{pmatrix} w^{0,1} & -w^{0,1} & \\ w^{0,2} & & -w^{0,2} \\ & w^{1,2} & -w^{1,2} \end{pmatrix} \begin{pmatrix} \mathbf{R}^0 \\ \mathbf{R}^1 \\ \mathbf{R}^2 \end{pmatrix} = \begin{pmatrix} w^{0,1} \\ w^{0,2} \\ w^{1,2} \end{pmatrix} \begin{pmatrix} \mathbf{R}^{0,1} \\ \mathbf{R}^{0,2} \\ \mathbf{R}^{1,2} \end{pmatrix}. \tag{5.5}$$

Adding a weight, like the inverse of the centroid estimate, adds very little extra computation to the least squares method, and offers an improvement to the overall centroid estimates. A comparison of the performance of both a weighted, and an unweighted least squares method, with using a single sub-aperture as the reference image is shown in Fig. 5.2. Whilst using a least squares method offers better performance than using a single sub-aperture image as a reference image, the error on the centroid estimate is still greater than 1 pixel when the induced shifts between

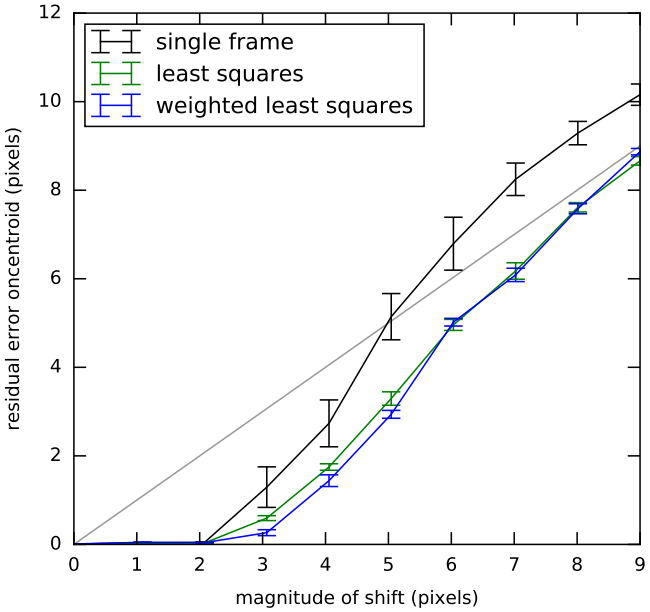

Figure 5.2: Performance of weighted, and unweighted least squares centroids with using a single sub-aperture image as the reference image for a range of different magnitude of image shifts. The grey line shows $y = x$ for reference. Both the weighted and unweighted least squares methods outperform using a single sub-aperture as a reference image for larger shifts. The weighted least squares also outperforms the least squares method until the shifts between sub-aperture images gets very large and neither is able to measure the centroids accurately.

sub-apertures is larger than 3 pixels. However, they remain under the grey 1:1 line, unlike using a single reference image.

5.3 Reference Image Generation

The results from Fig. 5.2 suggest that simply using the centroids from a weighted least squares method will not align the sub-aperture images sufficiently well to generate a usable supersized reference image when the shifts are larger than 3 pixels. This offers a very limited region where there is an advantage over simply using a single sub-aperture image as the reference, as this performs to a similar level for shifts of up to 2 pixels. However, unlike using a single sub-aperture image as the reference, the least squares methods both fall under the $y = x$ grey line, suggesting

they offer a better estimate of the shifts than assuming no shift between the sub-aperture images.

The supersized reference images themselves are simply created using a "shift and add" technique, described in Basden et al. (2014). Only instead of windowing the aligned and stacked sub-aperture images down to the size of the individual sub-apertures, the entirety of all of the sub-aperture images are kept. This means that as well as keeping track of the alignment of the individual sub-apertures each pixel in the supersized reference image needs to keep track of how many sub-aperture images are included in it. This is done with a second array, which simply keeps track of the number of sub-aperture images used in each pixel of the supersized reference image. The supersized reference image can then simply be divided by this array, effectively re-normalising the intensity values to the levels seen in a single sub-aperture.

5.3.1 Iteratively Generating Supersized Reference Images

The weighted least squares method generates more accurate centroids than using a single sub-aperture image, however, the error on these centroids is still too large to generate a usable supersized reference image when the shifts are large. The estimates are better than assuming there is no shift between the images, so the supersized reference image generated from this method should allow for more accurate centroids to be measured than the centroids used to generate it. With this process of measuring the same sub-aperture images with new iterations of supersized reference images, the centroid estimates should converge on the true centroid values. This should allow an iterative technique, which generates a superized reference image with centroid estimates from a previous supersized reference image, to converge on accurate centroid estimates. These accurate centroid estimates can be used to generate a supersized reference image which can be used as the reference image in a correlation WFS.

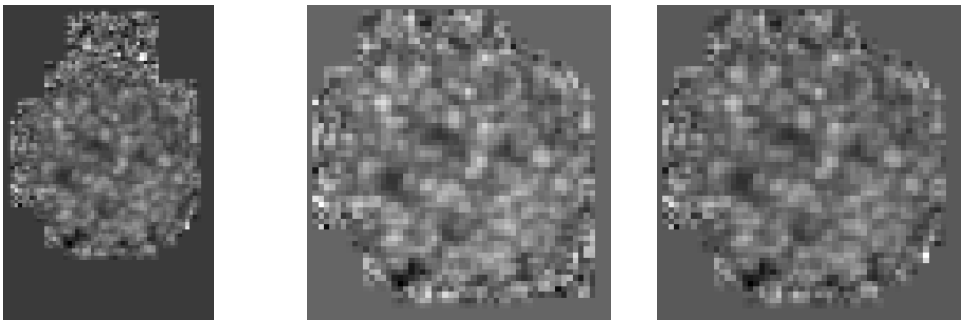

Figure 5.3: The left most image is the supersized reference image from the initial weighted least squares fit. The middle is the second iteration, using the first supersized reference image, and the right most image is the third version of the second supersized reference image. The supersized reference images progressively improve with each iteration, with more structure becoming apparent, showing that it is possible to iteratively generate a supersized reference image even when the first iteration does not show enough structure to work as a supersized reference image.

Iteratively generating a supersized reference image is computationally expensive, as is the first step of using a least squares method to create the initial centroid estimates. However after a supersized reference image has been created, centroid estimates using one should be accurate. This means that subsequent supersized reference images can be created by simply using the centroid measurements of the sub-apertures with the previous supersized reference image. An example of how iteration changes the generated reference images is shown in Fig. 5.3. The difference between the individual images appears to be small, however it is more apparent around the edges of the images. The least squares fit has aligned sub-aperture images on the top of the image which are not there on the subsequent iterations. The third iteration is also noticeably different to the second supersized reference image, with structure in the lower right portion of the supersized reference image becoming clearer.

The differential noise properties around the supersized reference images are visible in all iterations of Fig. 5.3. The center of the images show clear granular structure, at high SNR. However, the edges of the images show more noise, and it is possible to see the edge of a single noisy sub-aperture image in the upper region of the

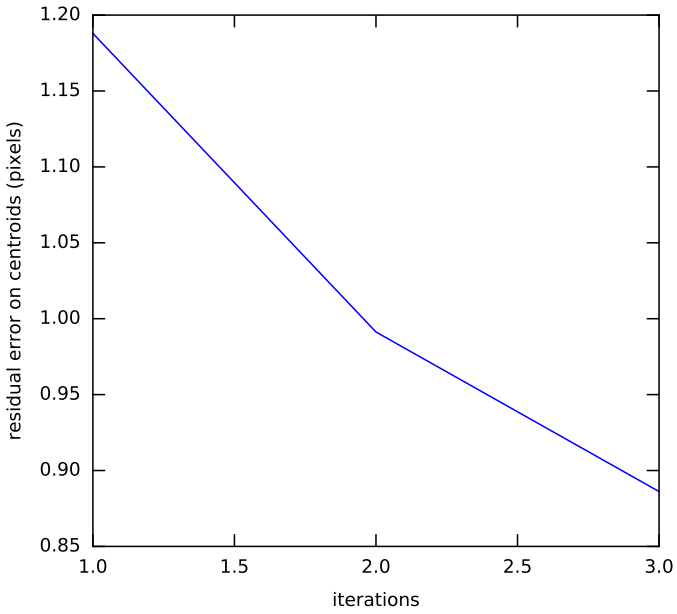

Figure 5.4: The residual error from iterating to generate a supersized reference image. The error is initially over 1 pixel from the weighted least squares fit (first iteration), and drops with each iteration of using the supersized reference image. The errors shown here are exaggerated by the fact that low SNR images were used, and that only 3 iterations were performed on the set of sub-aperture images.

first supersized reference images. This is a trend across all the supersized reference images, the center having a high SNR, which decreases towards the edge of the supersized reference images. The errors on the centroid estimates from using the different iterations of the supersized reference images in Fig. 5.3 is shown in Fig. 5.4.

As can be seen in the outer parts of the supersized reference images in Fig. 5.3, the sub-aperture images used had low SNRs. This was done to illustrate the effect iteration can have on aligning sub-aperture images. This, along with the large shifts between the sub-aperture images, means the error on the centroid estimates from the weighted least squares method is larger than a pixel. Despite this the supersized reference image produced (left part of Fig. 5.3) still shows the granular structure in the central regions. Each iteration brings the error on the centroids down, until it reaches a sub-pixel accuracy. This would decrease further with

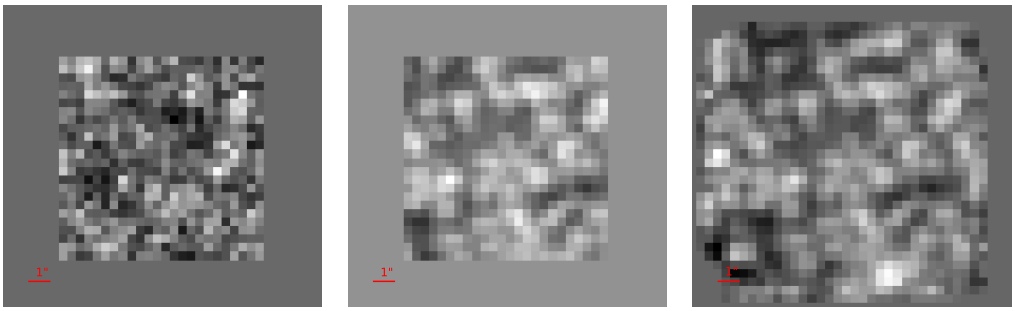

Figure 5.5: The left image shows a single noisy sub-aperture image, which is normally used in a correlating WFS. The middle and right images show artificially generated reference images, after iterating to reduce error on centroid estimates. The middle image is the supersized reference image windowed to the same FOV as the original sub-aperture images and the right image shows the full supersized reference image.

subsequent iterations, until the errors arise solely from noise on the sub-aperture images. This is reflected in the generated supersized reference images as the last iteration shows much more structure than the initial one, generated from the least squares fit.

5.3.2 Comparison of Reference Images

An example of a single sub-aperture image, a windowed reference image and a supersized reference image that has been generated using the iterative method is shown in Fig. 5.5. The left most image shows one of the noisy sub-aperture images, the type that would typically be used in a solar correlating WFS. The other two images show the generated reference images. The middle image shows the generated reference image windowed down to the same FOV as the sub-aperture images and the right most image shows the full supersized reference image. The granular structure on the generated reference images is much more apparent than in the single, noisy sub-aperture image. The increase in FOV is obvious when comparing the middle windowed frame to the full supersized reference image.

Observing the edges of the most right image in Fig. 5.5, it is apparent that the supersized reference image is not square. This is due to the random nature of

the shifts combined to generate the supersized reference image. The statistics of atmospheric turbulence generate a gaussian distributions of shifts, centered about zero (Kolmogorov, 1941). This means there will be many sub-aperture images with small shifts, and few with the largest shifts. When combined, creating a supersized reference image with sub-aperture images which follow these statistics, the central part of the supersized reference image is the average of many individual sub-aperture images. However the outer edges of the supersized reference images are much more sparsely populated, as there are few sub-apertures which sample that FOV and in some areas there are none. This is visible in the right image in Fig. 5.5, as some parts of the outer edges have no solar granulation visible, and are just uniform in intensity.

The values for regions which have no information from the individual sub-aperture images cannot remain 0 for images of solar granulation. This would cause a large disparity in the image, where the normal contrast is ($\sim 10\%$). The large disparity would add signifiant noise to the cross-correlation image, reducing the accuracy of the centroids measured using the supersized reference image. In order to minimise this the value for pixels which are not filled by at least one sub-aperture image are set to the average intensity of the set of sub-aperture images. This reduces the disparity between the parts of the supersized reference image which utilise information in the sub-aperture images and those that don't.

A similar approach needs to be taken with the individual sub-aperture images when they are cross-correlated with a supersized reference image. The sub-aperture images need to be the same size as the reference image in order to use the fast fourier transform (FFT) cross-correlation method (§ 2.2.1.2). This means the sub-aperture images need to be padded to the size of the supersized reference image. A similar problem of extra noise from a large discontinuity between the image and the padding would occur if the padding were set to an intensity value of 0. To avoid this the padding is set to the average intensity of the sub-aperture image, reducing the disparity between the sub-aperture image and the padding.

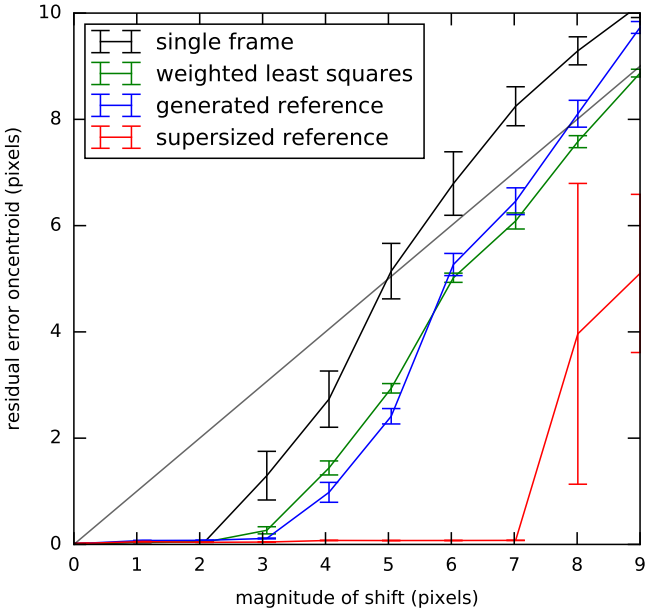

Figure 5.6: Results of using a variety of different reference images and centroiding techniques for sets of sub-apertures with different magnitudes of shift. The lines for using a single sub-aperture image and the least squares method are the same as in Fig. 5.2 and the blue and red curves are the results from using generated reference images. The red line is the full supersized reference image and the blue is the same reference image windowed down to the FOV of a single sub-aperture. The grey line shows $y = x$ for reference. It is apparent the supersized reference image outperforms all other methods for large shifts, and begins to fail with shifts of 8 pixels.

5.4 Results on Solar Granules

A comparison of how a supersized reference image performs compared with a windowed region of the supersized reference image with the same FOV as a single sub-aperture, and the weighted least squares method of centroiding is given in Fig. 5.6. Using a single sub-aperture as the reference image performs the worst out of all of the methods, though still offers good accuracy for small shifts between sub-aperture images. The weighted least squares offers a better estimation of the centroids for larger shifts, but still does not perform adequately when the magnitude of shifts reaches 4 pixels. The weighted least squares does still offer a better estimate of centroids than assuming none of the sub-apertures had any shifts (grey

line). This allows for the supersized reference image to be created using the iterative method. The supersized reference image performs well for all shifts, until it fails when the shifts reach 8 pixels.

The blue and red lines are derived from the same supersized reference image, after the iterative reference image generation has taken place. The supersized reference image is windowed to the same FOV as the individual sub-apertures before it is used as the reference image in the blue line. The full supersized reference image is used to generate the red line. The blue line has a similar performance to the weighted least squares method, and still does not perform adequately in the regime where shifts are large. This shows how effective the weighted least squares method is, as it gives the same performance as a reference image with much less noise. The supersized reference image is able to provide accurate centroid estimates up to very large shifts, where its performance rapidly declines.

The reason for the failure of the supersized reference to give good centroid estimates for very large shifts can be seen in Fig. 5.6. At these very large shifts the weighted least squares method is at the limit of being able to provide any estimate on the centroids, as it begins to overlap with the $y = x$ line. This is the first step of attempting to iteratively generate supersized reference images, when this starts to fail iteratively generating supersized reference images will not converge. We see that shifts of 8 pixels is at the limit of the iterative method, as the error bars are extremely large, indicating that the supersized reference image generated sometimes performs well, but at other times performs as badly as the rest of the methods. We also see that the weighted least squares method is nearly overlapping with the grey $y = x$ line for this value of image shifts.

5.4.1 Implementation into an Adaptive Optics System

The methods described in this chapter should be readily implementable in an AO system. The method for generating a supersized reference image, and updating it

as required, would not interfere with the operation of an AO loop. Updating a reference image in a correlating WFS, in a continuously working AO system, has been demonstrated by Basden et al. (2014). The only modification to this technique would be that the sub-aperture images would need to be padded to the size of the supersized reference image before they are correlated with the supersized reference image.

The method could then be implemented into an AO system in the following way;

1. Perform a weighted least squares fit with a set of sub-aperture images, and generate a supersized reference image.

2. Iteratively generate supersized reference images, updating the supersized reference image and centroid estimates with each iteration, until a reference image with the desired characteristics is created.

3. Use the supersized reference image in an AO system for estimating centroids in the WFS.

4. Use shifts generated using the supersized reference image, along with the sub-aperture images to generate subsequent supersized reference images.

Using this method the computationally expensive method of using the weighted least squares method, and iteratively generating a supersized reference image would only need to be used when starting to use supersized reference images. After this, the subsequent sub-aperture images, and centroid estimates using an existing supersized reference image, can be used to update the supersized reference image to cope with the evolution of the structure of the guide source. This occurs in solar granulation on the order of a few minutes (Bahng and Schwarzschild, 1961).

This could be implemented into an existing AO system in the WFS as shown in Fig. 5.7. Periodically a set of sub-aperture images and their centroid estimates can be used to update the supersized reference image. This can be done entirely

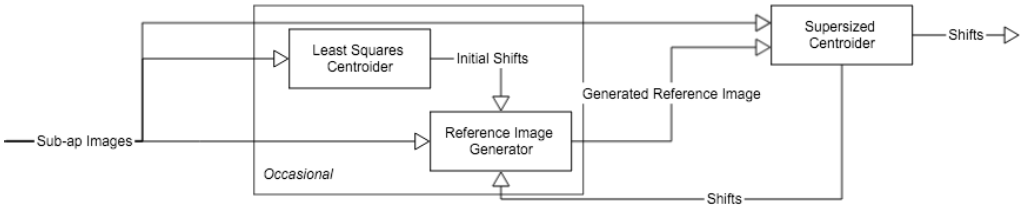

Figure 5.7: How a supersized reference image could be created, and used in an existing AO system, with minimal changes to its operation. The changes all occur within the calculations with the WFS and the calculation of the new supersized reference image could be offloaded onto a separate machine, so there should be no degradation in performance of the AO system. The only update required in the AO system would be the centroiding technique used, with one that could use a supersized reference image. This should offer a performance increase, from the more accurate centroid estimates in the WFS.

separately to the AO system, with the only interface being the new, supersized reference image, along with the change in reference slopes required (Basden et al., 2014).

5.5 Application to Laser Guide Stars

The methods shown here could also be of use to LGS WFSs. The main difference between the LGS and solar WFS is in how the signal is distributed in the sub-aperture images. The solar granulation extends out of the sub-aperture FOV in all directions, however, in a LGS it only extends out in one direction. This will reduce the performance benefit from using a supersized reference image, as there is a very limited regime where there will be extra signal added to the supersized reference image, and most parts will receive no extra image information.

5.5.1 Laser Guide Star Truncation

The effect of cutting off the wings of the sodium plume in WFS images is known as truncation. This effect can be seen in Fig. 5.8 where a sub-aperture FOV is plotted over the full laser plume, simulated from Pfrommer and Hickson (2014) sodium

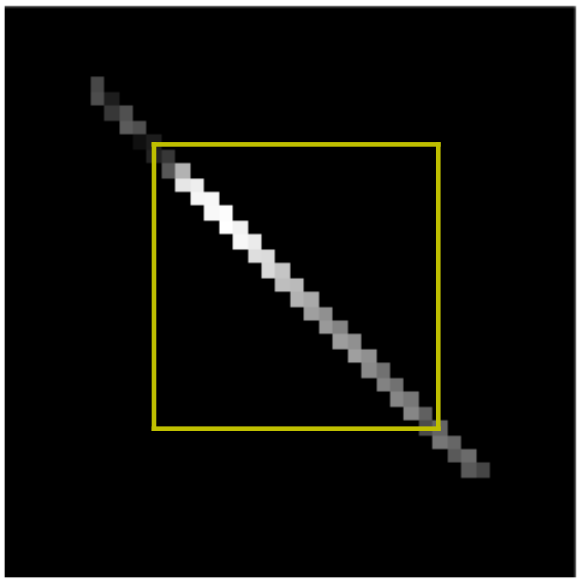

Figure 5.8: A full laser plume, with a yellow box around the FOV of a typical LGS WFS. The LGS intensity is shown in a log scale to emphasise the edges of the plume. The size of the laser plume is much larger than the size of the sub-aperture FOV, which truncates the plume.

laser profiles. This is a problem for WFS design for AO systems which use LGS, as there is often little structure in the laser plume. This makes the laser appear to be mainly continuous, with few features. This, combined with the truncation, makes centroiding a LGS image in a WFS complex. Centroiding methods for truncated LGS spots is an active area of research (Conan et al., 2009; Thomas et al., 2008b; Lardière et al., 2009).

5.5.2 Results on Laser Guide Stars

Due to the different design of LGS WFS to solar WFS, the shifts expected for LGS WFS are much smaller in pixels. Instead of pixel scales of tenths of an arc-second per pixel, much coarser resolutions are used to fit as much of the laser plume into a sub-aperture with the minimmum number of pixels, typically with pixel scales of

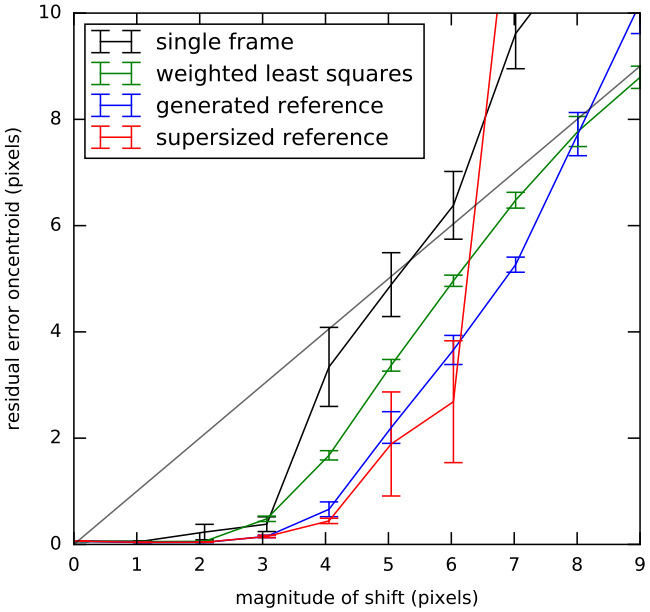

Figure 5.9: Results of using a variety of different reference images and centroiding techniques for sets of LGS sub-aperture images with different magnitudes of shift. The weighted least squares method (shown in green) gives a good starting point for all shifts shown, allowing the iterative generation of supsersized reference images to work. The windowed down generated reference image (shown in blue) performs noticeably better than the least squares method, however, the supersized reference image (shown in red) does not offer as much of an improvement as it did in the solar case and fails at a smaller magnitude of shifts than for the solar case.

$\sim 1\ ''$/pixel (Gendron et al., 2011; Cuby et al., 2008).

Figure 5.9 shows the performance of the various centroiding techniques applied to images of LGS, based on the windowed region shown in Fig. 5.8. The performance of the supersized reference image is better than any of the other methods, until the shifts reach a magnitude of 6 pixels. Here the technique fails in the same way that it does for the solar case. This is expected with the structure being restricted to one direction, rather than all directions like it is in the solar case. The windowed reference image that is generated performs much better than the least squares fit to the images and at a similar level to the full supersized reference image for some of the smaller shifts.

Measuring image motion for large shifts is not as much of a problem for LGS WFS

due to the coarser pixel scales. If this method was refined for use in LGS WFS it is possible that it would be beneficial to further truncate the LGS images (decreasing the FOV) in order to have finer pixel scales in the WFS.

5.6 Future Work

There are a number of avenues which need further investigation in the use of supersized reference images with LGS WFSs. These include looking at the benefit of using a supersized reference image for different amounts of elongation, and different levels of truncation in a WFS. The technique could also be investigated with the use of polar WFS as proposed by Thomas et al. (2008b). Another problem facing LGS is the stability of the sodium layer. Pfrommer and Hickson (2014) show that the sodium layer is continuously evolving which would affect the validity of any reference image over time, which may constrain how often the supersized reference image is required to be updated.

This technique could also be used outside of the AO community. For instance in biological imaging, where individual frames on a camera can be noisy, a number of frames can be co-aligned to reduce noise (Yang et al., 2014). This technique could not only give better shift estimates for aligning the images, but also give a larger FOV than any of the individual frames.

5.7 Summary

In this chapter a method of generating supersized reference images is described and demonstrated for both solar and LGS WFSs. This starts with using a least squares method to estimate the shifts for a set of sub-aperture images with large relative shifts, which makes using a single sub-aperture image as a reference unsuitable. A supersized reference image can then be created by co-aligning these shifted sub-aperture images and the supersized reference image iterated upon to generate a

supersized reference image which has better noise characteristics, and larger FOV than any of the individual sup-aperture images.

The performance of these methods is then compared for both solar and LGS WFS images, with varying degrees of relative shift added. In most cases the supersized reference image offers the best centroid estimates for the sub-aperture images, however at very large shifts it collapses and can no longer give accurate centroid estimates. In these regimes the other methods also fail leaving no way to estimate the centroids in these regimes.

Chapter 6

Solar SLODAR

The turbulence profile is important for the development and operation of MCAO systems. With both the DKIST and EST due to operate with MCAO the turbulence profile during the day is required. While there are many instruments for measuring high resolution turbulence profiles at night, there are few instruments developed for turbulence profiling during the day.

In this chapter I describe So-SLODAR, a slope based turbulence profiling instrument for day-time observations, and present turbulence profiles measured on the SST. I describe the design of a WF-WFS used on the SST for So-SLODAR in § 6.1. I describe how SLODAR was modified for So-SLODAR in § 6.2 and show example response functions for So-SLODAR in § 6.3. I show how the altitude resolution of So-SLODAR was determined in § 6.4. I give the turbulence profiles measured by So-SLODAR on the SST in § 6.6. Finally I give examples of how So-SLODAR could be developed in the future in § 6.7 and summarise the results in § 6.8

6.1 Design of the Wide-Field Wavefront Sensor

The predominant feature observed on The Sun in the visible is the granulation on the solar surface. These features are typically of order a few arcseconds across, which allows them to be centroided using cross-correlation techniques on regions

$\sim 5''$ across. Observing solar granulation is convenient as granules cover the whole of the solar surface, ensuring a good coverage of guide sources on the solar surface. However, their low contrast levels make centroiding images of granulation more complicated than for point sources or other simple objects.

To measure turbulence profiles during the day a WFS with a large FOV is required to sample large field separations. The design of the WF-WFS was similar to that used previously on the S-DIMM+ (Scharmer and van Werkhoven, 2010). The WF-WFS was placed on a spare port of the SST, such that it could operate alongside science observations without interfering with them. A schematic of the instrument alongside a photo of it on the SST is shown in Fig. 6.1. The design is simple, consisting only of a collimating lens from the telescope output, a lenslet array conjugated to the pupil of the telescope and a camera at the focus of the lenslet array. The part of the SST shown in Fig. 6.1b is the lower part of the vacuum tube, where the WF-WFS is mounted (shown in the green box).

The pupil and image planes are shown in Fig. 6.2. The lenslet array geometry is such that 10 full sub-apertures fit across the pupil (970mm), giving a sub-aperture size of 97mm. The lenslet array is hexagonal in shape, creating hexagonal sub-apertures. For simplicity the sub-apertures are assumed to be square when calculating the theoretical covariances for So-SLODAR. The port used for the So-SLODAR is picked off from the main optical path by a prism placed in the focal plane just outside the vacuum tube. This prism then acts as the field stop for the So-SLODAR, of $45''$.

The optical apparatus is based on the WF-WFS used for the S-DIMM+ and is summarised in Tab. 6.1. The lenslet array used was a custom lenslet array manufactured by SMOS* and its specification is given in Tab. 6.2. Finally, the camera used for the So-SLODAR is a Teledyne Dalsa Falcon2 CMOS, its specification is given in Tab. 6.3.

*http://www.smos-microoptics.de/

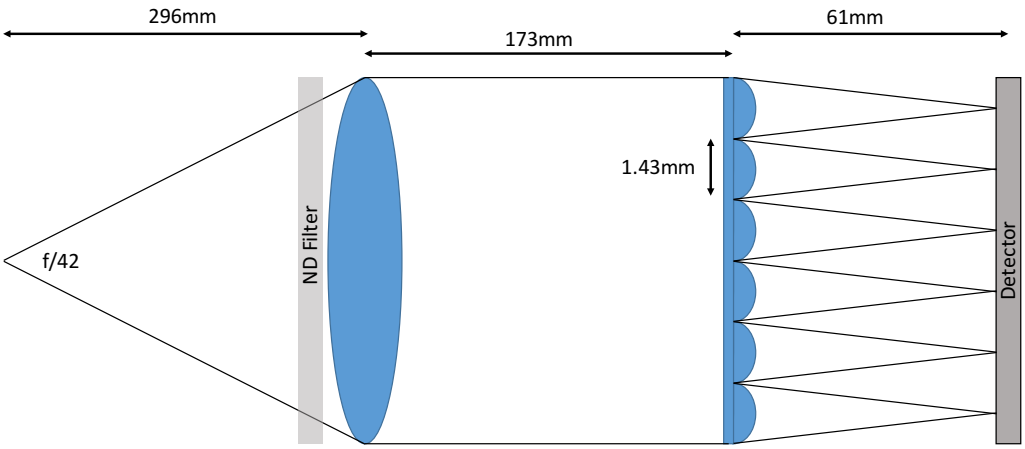

a

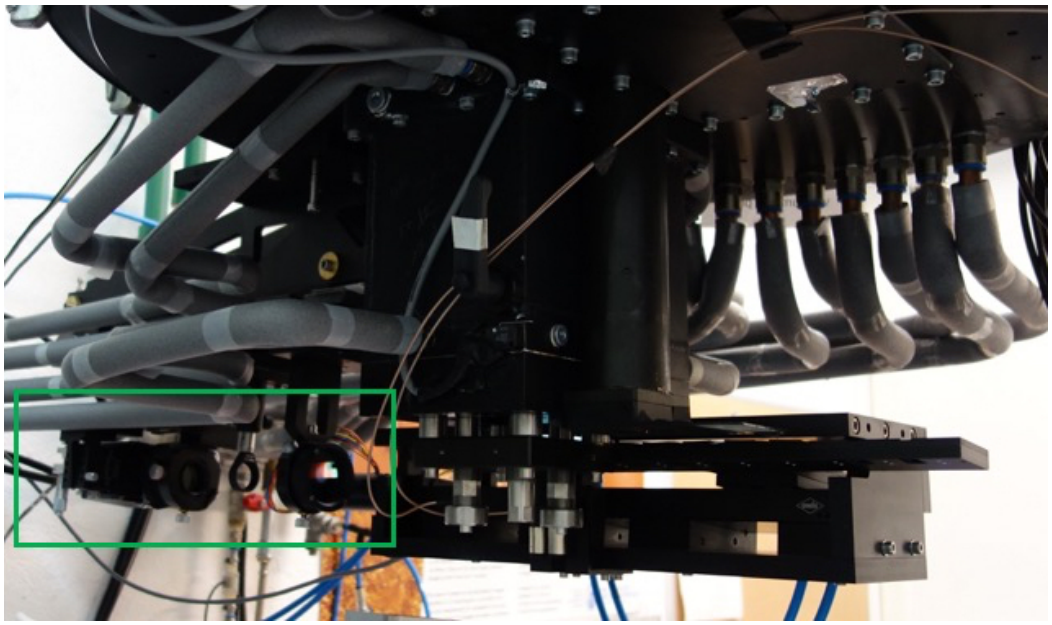

b

Figure 6.1: The So-SLODAR design is shown in Subfig. a with a photo of it installed on the SST in the green box in Subfig. b. The design simply uses a lens to collimate the output of the SST, a lenslet array conjugated to the pupil of the SST to split the pupil into sub-apertures and a camera at the focus of the lenslet array.

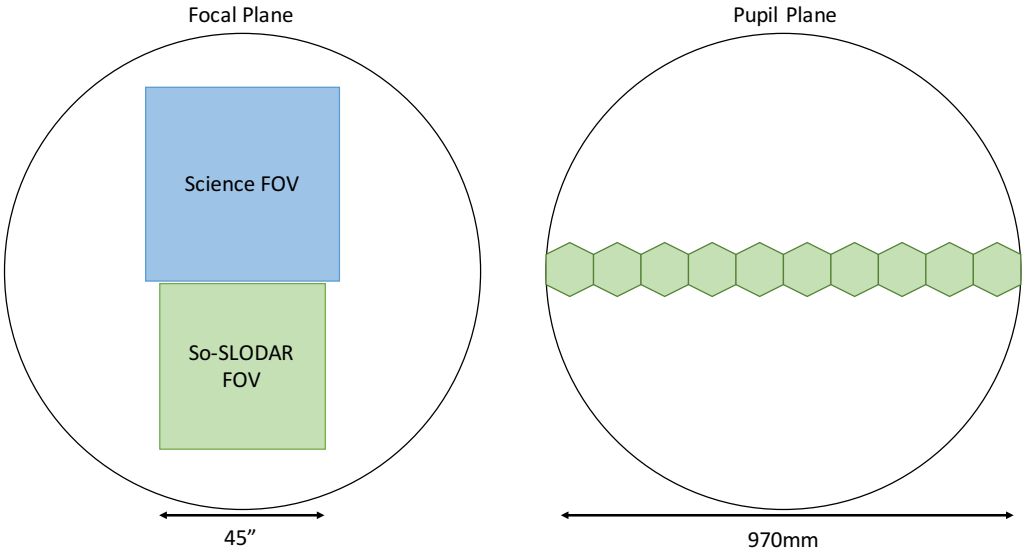

Figure 6.2: The geometry of the WF-WFS in the pupil and image planes of the SST. The left image shows the focal plane of the So-SLODAR, which is situated next to the main science FOV on the SST. The right image illustrates the geometry of the sub-apertures across the pupil plane. There are 10 sub-apertures across the SST pupil, each of 97mm which fill the full 970mm aperture.

Optic	Description	Thickness (mm)
	Telescope focus (f/42)	
	Focus to collimator	296.2
Melles Griot LAO 639	Collimating lens	9.4
	Collimator to lenslet array	179.9
SMOS lenslet array	Lenslet array	1.5
	Lenslet array to camera	63.3

Table 6.1: Description of the spacing of optical components for the WF-WFS. The description starts from the focal plane output of the telescope, after the Schupman corrector, where the pick-off for the field is located.

Manufacturer	Smart Micro-optical Solutions
Pitch (mm)	1.43
Focal length (mm)	63.3
Diameter (mm)	29.5

Table 6.2: Specification of the SMOS lenslet array used in the So-SLODAR.

Manufacturer	Teledyne Dalsa
Model	Falcon2 4M
Detector Size (pixels)	2432×1728
Max. frame rate (Hz)	168
Pixel size (µm)	6
Pixel scale (″/pixel)	0.234

Table 6.3: Parameters of the camera used for the So-SLODAR.

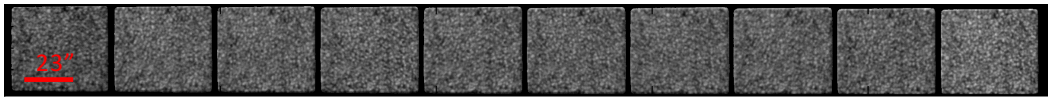

Figure 6.3: Frame taken from the WF-WFS used for the So-SLODAR. There are ten fully illuminated sub-apertures running across the pupil, each with a 45″ FOV. This gives each sub-aperture a usable size of $\sim 200 \times 200$ pixels on the detector.

Due to the large volumes of data the So-SLODAR generates the camera is windowed down to only read out a single row of sub-apertures, as shown on the right of Fig. 6.2. This greatly reduces the size of data packets and allows for longer data sets to be obtained which helps ensure the measured slopes are properly temporally averaged. An example WF-WFS frame is shown in Fig. 6.3.

6.2 Modifying SLODAR for use in Solar Observations

There are two major differences between applying SLODAR to day-time observations and applying it to night-time observations. The first is estimating the wavefront slopes with an extended source. This causes the size of the effective pupil to change with altitude. The second is the different availability of "guide stars" across the FOV, as The Sun is extended over 0.5° there are many available sources over the stellar disk, as opposed to the more limited regime SLODAR works in at night.

6.2.1 Expanding Pupil

As previously discussed in § 3.5.1 there is a problem in solar observations associated with measuring wavefront slopes over extended FOVs. If this effect is not taken into account then the influence of high altitude layers will be underestimated.

In a similar way to the S-DIMM+ the diameter of a sub-aperture is replaced with the effective diameter which is a function of altitude, as given in equation 3.46. This changes the definition of the pupil function, defined in equation 3.31, to now also be a function of altitude;

$$\begin{aligned} W_{\text{eff}}(h,\mathbf{r}) &= 1 \qquad \text{for } |x|,|y| < 1/2 \\ &= 0 \qquad \text{otherwise,} \end{aligned} \tag{6.1}$$

where h is the altitude at which the pupil size is calculated, and the size of the window is calculated using equation 3.46. The linear slope function then also depends on the altitude of the turbulent layer;

$$\int F^2_{x,\text{eff}}(h,\mathbf{r}) W_{\text{eff}}(h,\mathbf{r}) d\mathbf{r} = 1. \tag{6.2}$$

The modified pupil function from equation 6.1 and the modifield slope function from equation 6.2 are substituted into equation 3.35, the covariance of the slopes;

$$\begin{aligned} C^x_{i,j,i',j'}(h) = \int\int \langle \phi^{[1]}_{i,j}(w\mathbf{r}^{[1]}_{i,j}) \phi^{[2]}_{i',j'}(w\mathbf{r}^{[2]}_{i',j'}) \rangle F_{x,\text{eff}}(\mathbf{r}^{[1]}_{i,j}) F_{x,\text{eff}}(\mathbf{r}^{[2]}_{i',j'}) \\ \times W_{\text{eff}}(h,\mathbf{r}^{[1]}_{i,j}) W_{\text{eff}}(h,\mathbf{r}^{[2]}_{i',j'}) d\mathbf{r}^{[1]}_{i,j} d\mathbf{r}^{[2]}_{i',j'}, \end{aligned} \tag{6.3}$$

which in turn modifies equation 3.36, the covariance of the slopes with piston removed to be altitude dependant;

$$\begin{aligned} \langle \Phi^{[1]}_{i,j}(w\mathbf{r}^{[1]}_{i,j}) \Phi^{[2]}_{i',j'}(w\mathbf{r}^{[2]}_{i',j'}) \rangle = \; & -\tfrac{1}{2} D_\phi(w\mathbf{x}) \\ & + \tfrac{1}{2} \textstyle\int W_{\text{eff}}(h,\mathbf{r}^{[1]}_{i,j}) D_\phi(w\mathbf{x}) d\mathbf{r}^{[1]}_{i,j} \\ & + \tfrac{1}{2} \textstyle\int W_{\text{eff}}(h,\mathbf{r}^{[2]}_{i',j'}) D_\phi(w\mathbf{x}) d\mathbf{r}^{[2]}_{i',j'} \\ & - \tfrac{1}{2} \textstyle\int\int W_{\text{eff}}(h,\mathbf{r}^{[1]}_{i,j}) W_{\text{eff}}(h,\mathbf{r}^{[2]}_{i',j'}) D_\phi(w\mathbf{x}) d\mathbf{r}^{[1]}_{i,j} d\mathbf{r}^{[2]}_{i',j'}. \end{aligned} \tag{6.4}$$

For a given altitude the effective diameter of the sub-aperture is calculated and the sub-aperture separations recalculated to be in terms of the effective pupil diameter. This then allows for the normal SLODAR covariance calculations to be used, modifying only the size of the pupil and separations. However, there is still an altitude dependence, so the pupil size, separation and covariances need to be generated separately for every altitude.

The subsequent calculations are then all similar to SLODAR. The removal of the effect of global tip/tilt is simple for So-SLODAR, as the WF-WFS is constrained to a single row of sub-apertures, which is only in one dimension.

For the So-SLODAR the chosen FOV to use in centroid estimation was 24 pixels, which corresponds to $5.6''$. This was chosen as the correlating region to give a FOV which is consistent with the S-DIMM+, containing enough structure to measure accurate centroids. A comparison of how this changes the response functions of SLODAR is shown in Fig. 6.4.

The two effects of the expanding pupil are obvious. Firstly the averaging of the turbulence at higher altitudes can be seen as the peak is much lower in the So-SLODAR response functions (dotted lines) than for the SLODAR response functions (solid lines) at higher altitudes. Secondly the peaks for the So-SLODAR response functions are shifted left with respect to the peaks of the SLODAR response functions. This is due to the separations of the projected sub-apertures changing as a function of altitude. The separation in meters is consistent between SLODAR and So-SLODAR, but as the effective pupils increase in size, the separations in units of sub-aperture widths decreases, shifting the peaks to smaller apparent separations in So-SLODAR.

6.2.2 Multiple Guide Sources

Unlike SLODAR at night, during the day any region of the solar surface can be used as a “guide star”. This means that over the stellar disk, there many possible

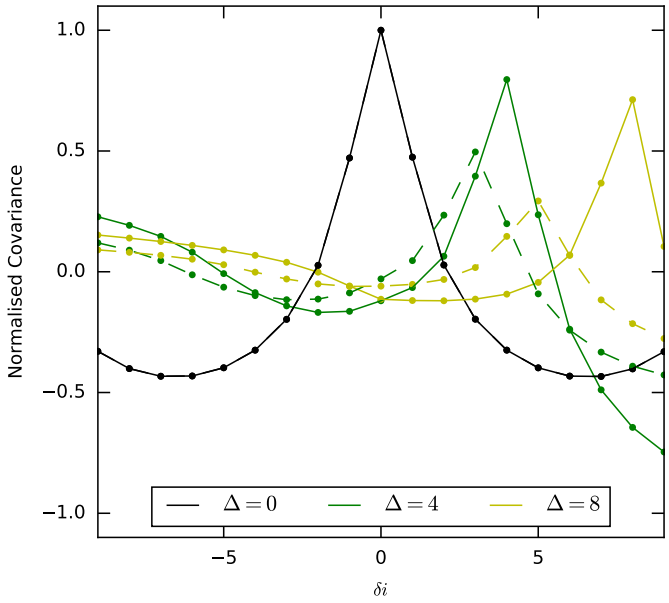

Figure 6.4: Comparison of SLODAR and So-SLODAR response functions for the same altitudes. The SLODAR response functions in solid lines, with the response functions modified for the So-SLODAR at the same altitudes shown in dotted lines. The SLODAR response functions are the same as the ones shown in Fig. 3.5 and the response for the ground layer ($\Delta = 0$) for the two techniques is identical.

choices for available guide stars. In reality we are limited by the sampling of the detector. The sub-apertures are 200 pixels across, using regions of width 24 pixels for correlating. This leaves 176 possible different field directions in each dimension, shifting the correlating region by 1 pixel for each source.

The response functions using so many guide sources would be extremely large and would take a substantial amount of time to compute. The measured covariances would also take an extremely long time to calculate, as a cross-correlation would have to be performed for every field direction. Such large response functions would also take a substantially long time to fit to the measured covariances and generate profiles. This makes it unreasonable to use the full size for the response functions, as it would take substantially longer to reduce the frames to profile estimates than it would to record them, which prohibits the possibility of using a profiling instrument running in tandem with science observations at the SST. As seen later in § 6.3 the

resolved altitudes are limited by the expanding pupil and largest field separation, so there is no gain in resolution to be attained from increasing the number of guide sources at intermediate separations.

In order to attain the highest resolution profiles at low altitude the largest field separations should be included. However to measure the turbulence to the greatest altitude the smallest field separations should be used. This leads us to choose a set of response functions which use a regular grid of guide sources across the FOV. This gives many estimations of the covariances for small separations, which can be averaged over to reduce the effects of noise for high altitudes and includes the largest field separations to give good altitude resolution at the ground.

The choice of field separations for the So-SLODAR is a regularly sized grid of 7×8 field directions across the image plane. This is a compromise between the computational cost of calculating slopes, covariances and fitting the measured covariances to the response functions. The chosen set of field separations are shown plotted over a sub-aperture image in Fig. 6.5. This gives the largest field separation of $39.3''$, and a smallest field separation of $5.3''$.

6.3 Theoretical Response Functions

Response functions show the expected response of an instrument, in this case So-SLODAR, to a single layer of turbulence at a given altitude. A set of response functions are used to fit the measured covariances of the So-SLODAR in order to estimate the turbulence profile. Here I show some So-SLODAR response functions and describe how the altitude resolution of the So-SLODAR was determined.

As has previously been shown in Fig. 6.4 the response functions for So-SLODAR differ from those used in SLODAR. However the availability of more guide sources allows for multiple different field directions to be used in response functions and fitting for the turbulence. This results in two dimensional response functions,

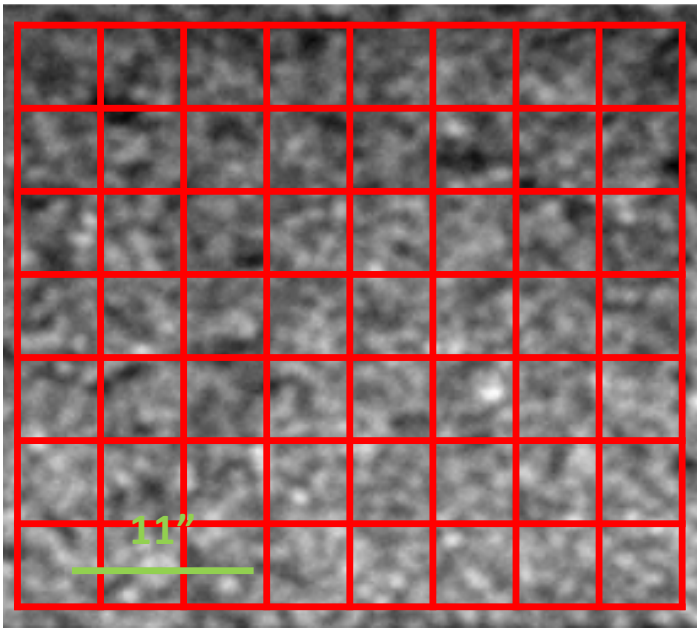

Figure 6.5: A single sub-aperture image with the grid of 7×8 FOVs used as guide sources overlaid. The size of the boxes show the size of the regions correlated over to estimate the centroids for a given field direction. The chosen spacing of the sources spans the whole FOV of the sub-aperture with no FOVs overlapping.

where each row corresponds to a different field separation, such as the ones shown in Fig. 6.4.

The response functions are generated in the same way as the response functions shown in Fig. 6.4 for each individual field seperation. A selection of response functions are shown in Fig. 6.6. The response functions shows how the expanding pupil restricts the ability of the instrument to detect turbulence at high altitudes, as the response is much weaker than for low altitude turbulence. At the highest altitudes the strength of the peak of the covariance function is diminished almost to the background level.

6.4 Orthogonality of Response Functions

As there are multiple different field separations in the measured covariances and response functions the approach used for choosing the altitude of the response

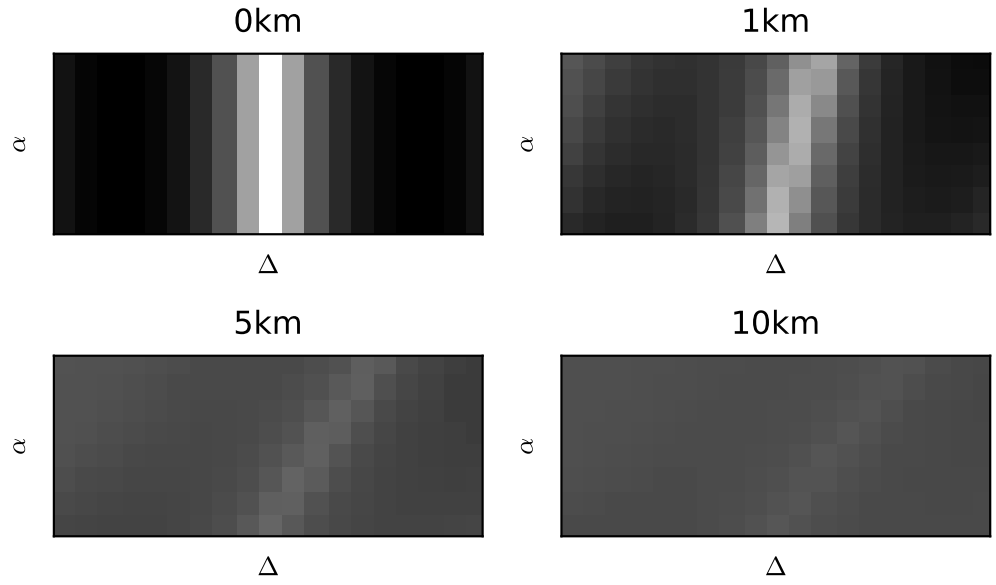

Figure 6.6: Example response functions for So-SLODAR shown on the same colour scale. The y axis (α) shows increasing field seperation and the x axis (Δ) shows sub-aperture seperation, centered around zero offest. The effect of the expanding pupil can be clearly seen as the strength of the response falls for high altitude turbulence. These response functions differ in shape from the response functions for S-DIMM+ shown in Fig. 3.7.

functions for SLODAR cannot be used. Instead we look at the orthogonality of the response functions at different altitudes. If two response functions are orthogonal then when fitting for a single layer of turbulence that matches one of the response functions altitudes, the fit should calculate that the turbulence all fits into the response function. If however the response functions are not orthogonal then the fit may indicate strength at multiple altitudes. A more orthogonal set of response functions should reduce the likelihood of fitting turbulence into a response function at the incorrect altitude. The response functions shown next all use the geometry of the So-SLODAR so they can be compared directly, a single row of 10 sub-apertures across a 1m pupil, with a grid of field separations, from $5.6''$ to $39.3''$, seperated by $5.6''$.

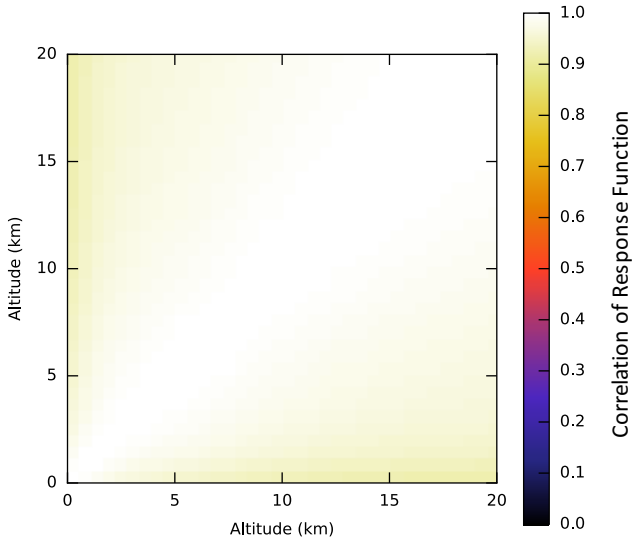

Figure 6.7: Correlation of response functions for S-DIMM+. The response functions are not very orthogonal, with the correlation never falling below 0.9, even when comparing the ground layer to the highest altitude response function.

6.4.1 S-DIMM+ Response Functions

S-DIMM+ response functions were generated for altitudes up to 20km in order to compare their orthogonality to that of So-SLODAR response functions (§ 6.4.3). The correlations of the response functions for S-DIMM+ are shown in Fig. 6.7. All of the response functions share a lot of common structure, making them well correlated and limiting the resolution of the S-DIMM+. This is seen in Fig. 6.7 as the correlation between all of the response functions is large and never falls below 0.9.

6.4.2 SLODAR Response Functions

The correlation of the response functions for SLODAR are shown in Fig. 6.8. These were generated for the same geometry as is used in the S-DIMM+ and So-SLODAR, where multiple guide sources are available and only a single row of sub-apertures are measured. The response functions appear to be practically orthogonal for low altitude turbulence. This means the resolution of a SLODAR system using this

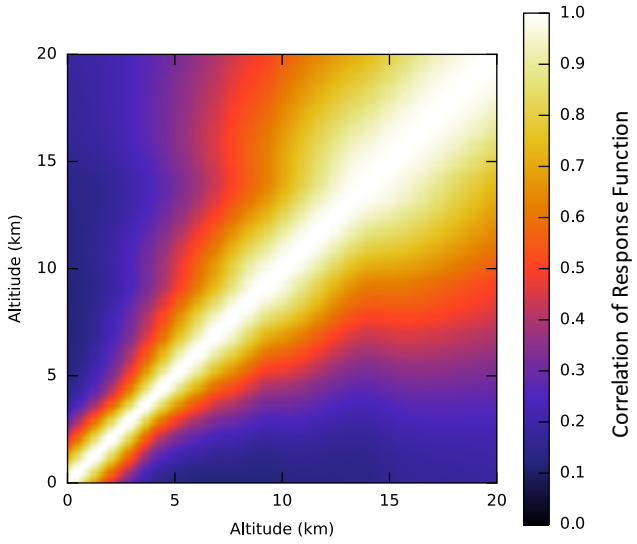

Figure 6.8: Correlation of the SLODAR response functions. Here we see that the response functions are much more orthogonal than the ones used in S-DIMM+ (Fig. 6.7). The response functions appear less orthogonal at higher altitudes due to the loss of signal contribution from the guide sources with the larges field separations.

geometry will give high resolution at low altitudes. As the altitude increases, the orthogonality of the response functions falls, this is due to to the peak of the covariances moving out of the sampled region for the largest field separations.

For a typical night-time SLODAR system the orthogonality of the response functions appears much more like the orthogonality shown in Fig. 6.8 for low altitudes, and continues in that way to the high altitudes. This is not the case for the response functions here due to the multiple guide sources used. The guide sources with the largest field separations offer the smallest difference in altitude between resolved bins. However, the full telescope pupil separates at low altitudes, leaving them unable to measure the turbulence profile above this separation height. For narrow separations the distance between resolved altitude bins is low, however, the full telescope pupil separate at a much higher altitude. This is reflected in the correlation of the response functions, the correlation is low for low altitudes, but as the altitude increases only the narrow field separations contribute useful signal, where the altitude separation between adjacent bins is large (or the correlation

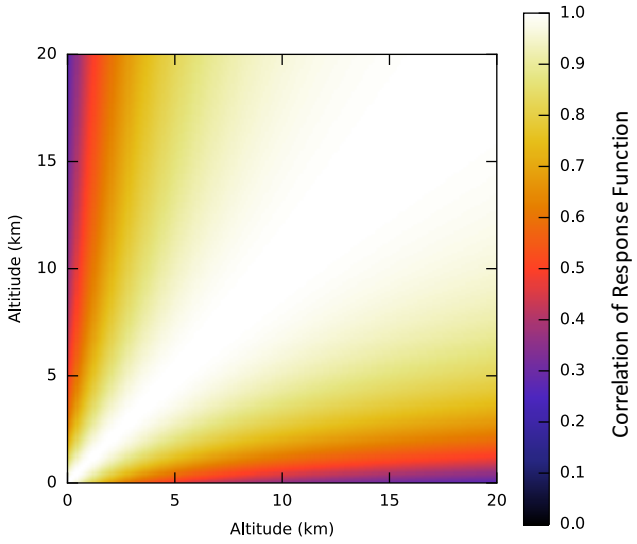

Figure 6.9: Correlation of the So-SLODAR response functions. There is a large difference between the response function and the ground and higher altitude response functions, apparent as the correlation is small. However at higher altitudes the orthogonality is greatly reduced, to the extent of the highest altitudes almost appearing to be degenerate.

between altitudes with small separations is large).

6.4.3 So-SLODAR Response Functions

Figure 6.9 shows the orthogonality of So-SLODAR for various altitudes. The orthogonality of the response functions at low altitudes is much greater than the orthogonality for high altitudes. This suggests that the optimal choice of the altitudes will have a higher resolution at low altitudes, with decreasing resolution as the altitude increases. This is similar to the choice of altitudes for S-DIMM+.

Comparing the orthogonality of S-DIMM+ (Fig. 6.7) with So-SLODAR (Fig. 6.9) response functions, the So-SLODAR response functions are much more orthogonal than the response functions for S-DIMM+. This should result in the So-SLODAR being more robust than the S-DIMM+. Comparing Fig. 6.8 with Fig. 6.9 we see that SLODAR has much more orthogonal response functions than So-SLODAR. This is expected, as the modifications made to SLODAR reduce both the height

of the correlation peak and shift them towards smaller pupil operations, both of which will reduce the orthogonality of the response functions.

6.4.4 Altitude Resolution of So-SLODAR

The altitude resolution of So-SLODAR was calculated from the orthogonality of the response functions shown previously. The resolved altitudes are chosen such that the response functions of adjacent altitude have the same orthogonality. The value for the orthogonality are chosen from SLODAR analysis. SLODAR uses altitude bins taken from the peak of the correlation moving by an integer number of sub-apertures. For a standard SLODAR observing two stars, using the sub-aperture geometry of the So-SLODAR, the orthogonality of adjacent response functions is $\sim$ 0.95.

The limiting correlation value of 0.95 was used in conjunction with Fig. 6.9 to generate the altitude bins for So-SLODAR. The initial height was taken to be the ground layer. The next layer is chosen to be the altitude where the correlation between the response function for that altitude and the response function for the ground is less than 0.95. This is continued until a maximum altitude is reached. For the So-SLODAR used here the generated altitude bins are $h = 0, 0.5, 1.2, 2.2, 3.8, 6.8, 14, 30$ km. A trace of this over the orthogonality plot for So-SLODAR is shown in Fig. 6.10. The response functions generated correspond to the case in SLODAR where the largest field separation covariance peak moves by a single sub-aperture for each of the resolved altitudes.

6.5 So-SLODAR Data Reduction

The raw camera images from the So-SLODAR need to be reduced to covariances, which the response functions can be fitted to. However, before this can be done the frames are first flat-fielded and de-biased to remove vignetting and any artifacts on

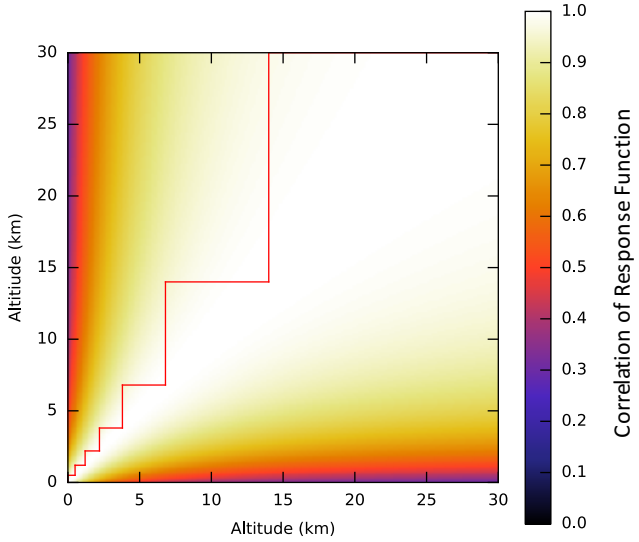

Figure 6.10: The altitude resolution plotted over the correlation of the response functions for So-SLODAR. The red line shows the trace used to calculate the altitude bins for the So-SLODAR. This highlights that the resolution is altitude dependent, with a greater density of altitude bins at low altitudes and fewer at high altitudes.

the optics. Once a day the So-SLODAR captured dark frames for each exposure setting and took flat field measurements using long exposures when the SST was continuously slewing (in flat-fielding mode). This smears out the images of the granular structure, and when averaging over many frames generates flat-field images (Löfdahl and Scharmer, 2012). An example of a processed frames is shown in Fig. 6.3.

The frame is then separated into individual sub-apertures, which in turn are separated into the different field directions shown in Fig. 6.5. These individual regions are centroided using the images from a single frame as the reference image for the whole set of images and the global tip/tilt term subtracted from each of the field directions as previously discussed in § 3.4.

The covariances of the centroid measurements are then calculated and formatted to the shape of the response functions calculated in § 6.4.4. An example of a processed set of data is shown in Fig. 6.11. The measured and fitted covariances have similar shapes, as can be seen from the residual plot, however, the auto-correlation (0 field

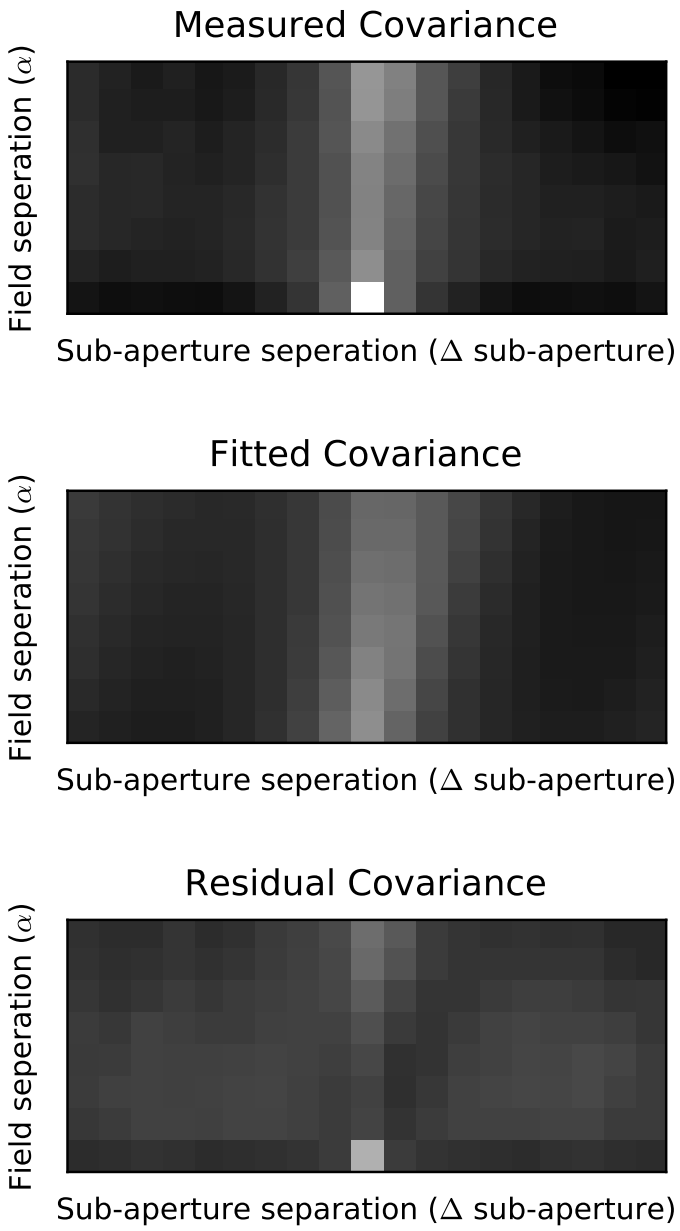

Figure 6.11: An example covariance measured with So-SLODAR shown with the fitted profiles covariance and the residual between the two. The residuals and measured covariances both show the noise from the peak of the autocorrelation, which can be seen at 0 field separation and 0 sub-aperture separation as the brightest point.

separation) measurements differ. This is due to the noise in the centroids appearing in the peak of the auto-correlation as described in Butterley et al. (2006). The scale factor in the fitting process for each of the individual response functions gives the strength of the turbulence at that layer. These strengths are then used as the turbulence profile.

6.6 Measured Turbulence Profiles

The WF-WFS was used on the SST for two campaigns, one in September 2013 and another in April/May 2014, to measure the turbulence profile in La Palma during the day. Series of raw frames from the WF-WFS were captured and brought back to Durham for analysis.

The centroiding was then performed on the frames to generate centroids using the Fourier transform based cross-correlation algorithm and peak fitted using the 2nd order polynomial fitting technique, both described in § 2. The cross-correlations between the different sub-apertures and field directions were then calculated using the technique described in Wilson (2002), using 1 minute of centroid measurements for each measurement. The correlations were then averaged by field separation and sub-aperture separation in order to reshape them to the same size and shape as the response functions described in § 6.3. The response functions were fitted to the measured cross-correlations using a non-negative least squares fit in order to calculate the turbulence profile.

6.6.1 Example Profiles

The turbulence profiles measured on 19 September 2013 are shown in Fig 6.12, along with the median profile for that day in Fig. 6.13. Fig. 6.12 is split into three regions, the two lower sections show the turbulence profile and the upper section shows the r_0 measurements. The turbulence profile is split at 500m due

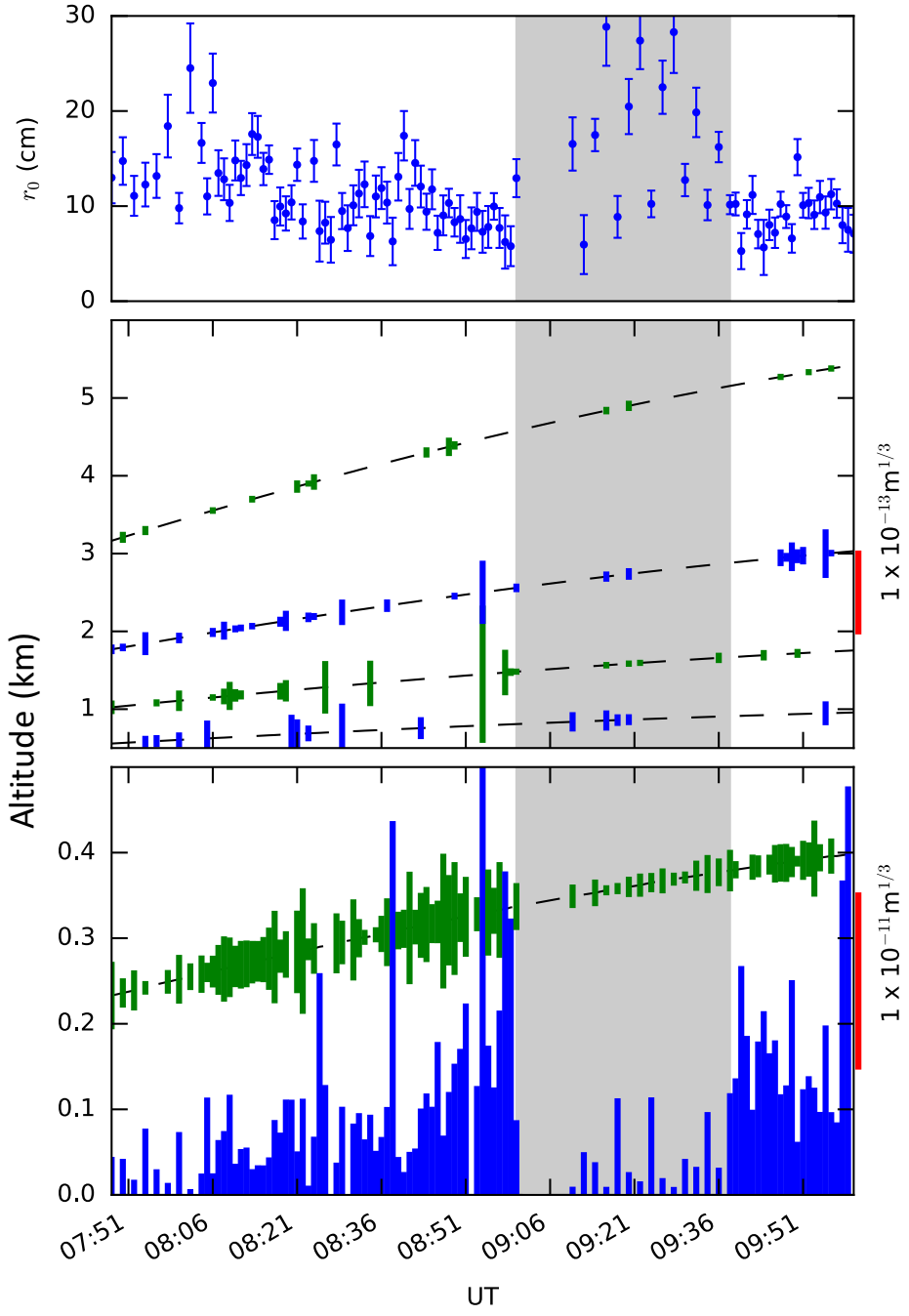

Figure 6.12: Turbulence profiles measured on 19 September 2013. The profile is split between two plots, with different scales so both the high altitude, and low altitude turbulence can be clearly seen. The upper part of the plot shows the r_0 values measured for each of the profiles from the WFS data. The grey region shows where cloud was present during data capture.

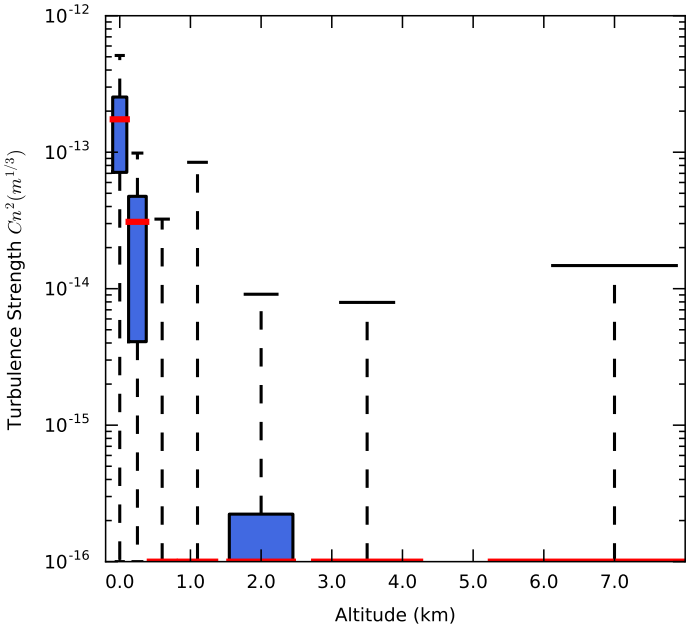

Figure 6.13: The median profile from the 19 September 2013 shown on a box plot. The bins used are sympathetic to the results from Fig. 6.12, where the altitude resolution decreases with altitude. The red line shows the median strength of the turbulence, the blue shaded regions show the first and third quartile strengths and the bounding lines shown the 5% and 95% quartiles. There was no observed turbulence above the 7km bin, so the altitude is cut off here.

to the significant change in estimated turbulence strength around this altitude. The red lines to the right of the plots show the height of a region with the given turbulence strength. The upper region shows the estimated r_0 values estimated with the DIMM technique applied to individual pairs of sub-apertures and field directions. The error bars are then calculated by taking the standard deviation of the individual estimates of r_0.

We see from the top section of Fig. 6.12 that the seeing conditions were variable, with large disparities between 09:00 and 09:40 due to intermittent cloud. Looking at the turbulence profiles the turbulence is mostly situated at the ground, with some structure intermittently appearing at higher altitudes. There was no observed turbulence above $\sim$ 6km, hence these altitudes are not shown. We see the structure of the turbulence for that day more clearly in Fig. 6.13, where the median conditions are shown. Here we see strong turbulence at the ground, with some

structure reading up to $\sim$ 7km appearing intermittently. The r_0 values calculated are consistent with the expected values, with the SST typically reporting r_0 values of $\sim 10 - 20$cm in the morning (Scharmer et al., 2002), with worsening conditions towards mid-day. The values for both the strength of individual layers in the measured turbulence profile and the r_0 measurements are also plausible when compared to night-time profiles, where the strength of the turbulent layers in C_n^2can be up to $10^{-12}\mathrm{m}^{1/3}$ and r_0 values are typically of the order of 10cm.

The next campaign took place at the end of April 2014. The profiles from this campaign are shown in Figs. 6.14-6.16. These show a similar structure to the profiles taken on 19 September 2013, with a predominant ground layer and some higher altitude structure visible. Again there is no observed turbulence above 6km, so the plots don't show any altitude higher than this. The median profiles for these day are shown in Figs. 6.17-6.19. The median profiles show a measure of the turbulence from each of the days. They tend to show similar structure, a strong ground layer is usually present and turbulence distributed up to 2km. The feature which seems to exist at $\sim$ 2km has been seen at night by Stereo-SCIDAR on occasion (Osborn et al., 2013).

A strong ground layer has been observed during the day, of a similar strength by S-DIMM+ (Scharmer and van Werkhoven, 2010). The strength of the low altitude turbulence is also consistent with the turbulence profile measured by S-DIMM+. There is a discrepancy between the turbulence profiles shown here and the ones measured by S-DIMM+, which is the high altitude turbulence. This is likely to be due to the response of the So-SLODAR to the high altitude turbulence and it being extremely attenuated due to the expanding pupil effect, meaning it cannot be measured reliably with the So-SLODAR in its current state.

It should be noted that the profiles shown here are not statistically representative of the daytime turbulence in La Palma, as the sample size is extremely small (only 4 partial days). Also the time resolution of the profiles is limited by the camera computer. Due to the large data rates from the camera the computer buffers fill

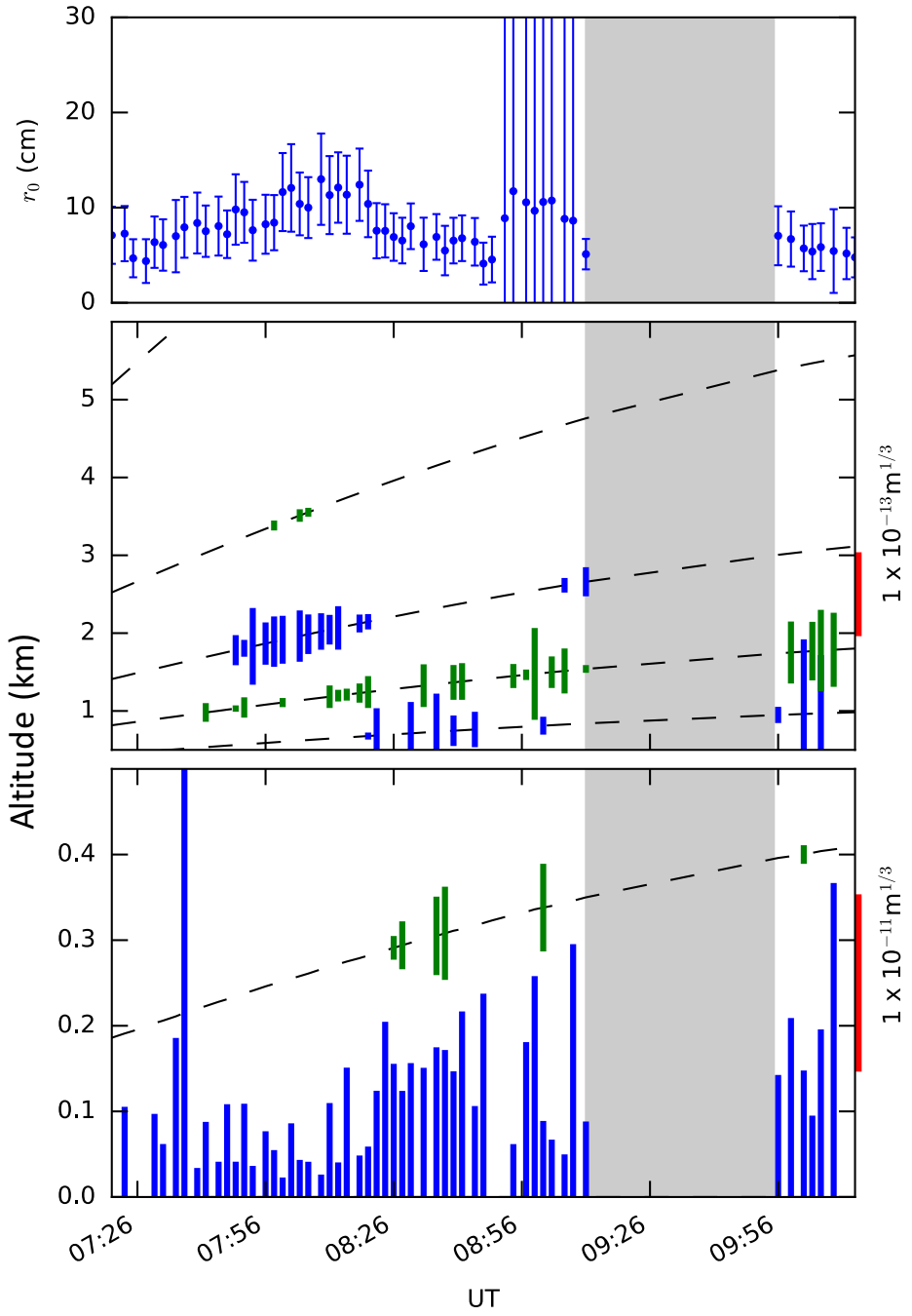

Figure 6.14: Turbulence profiles measured on the 23 April 2014. The profiles follow the expected pattern of a strong ground layer with intermittent turbulence at the higher altitudes. There is no observed turbulence above $\sim$ 5km, so the high altitudes are not plotted. There was a spell of intermittent cloud from $\sim$ 9:00 until $\sim$ 10:00, highlighted in grey, making measurements between these times unreliable.

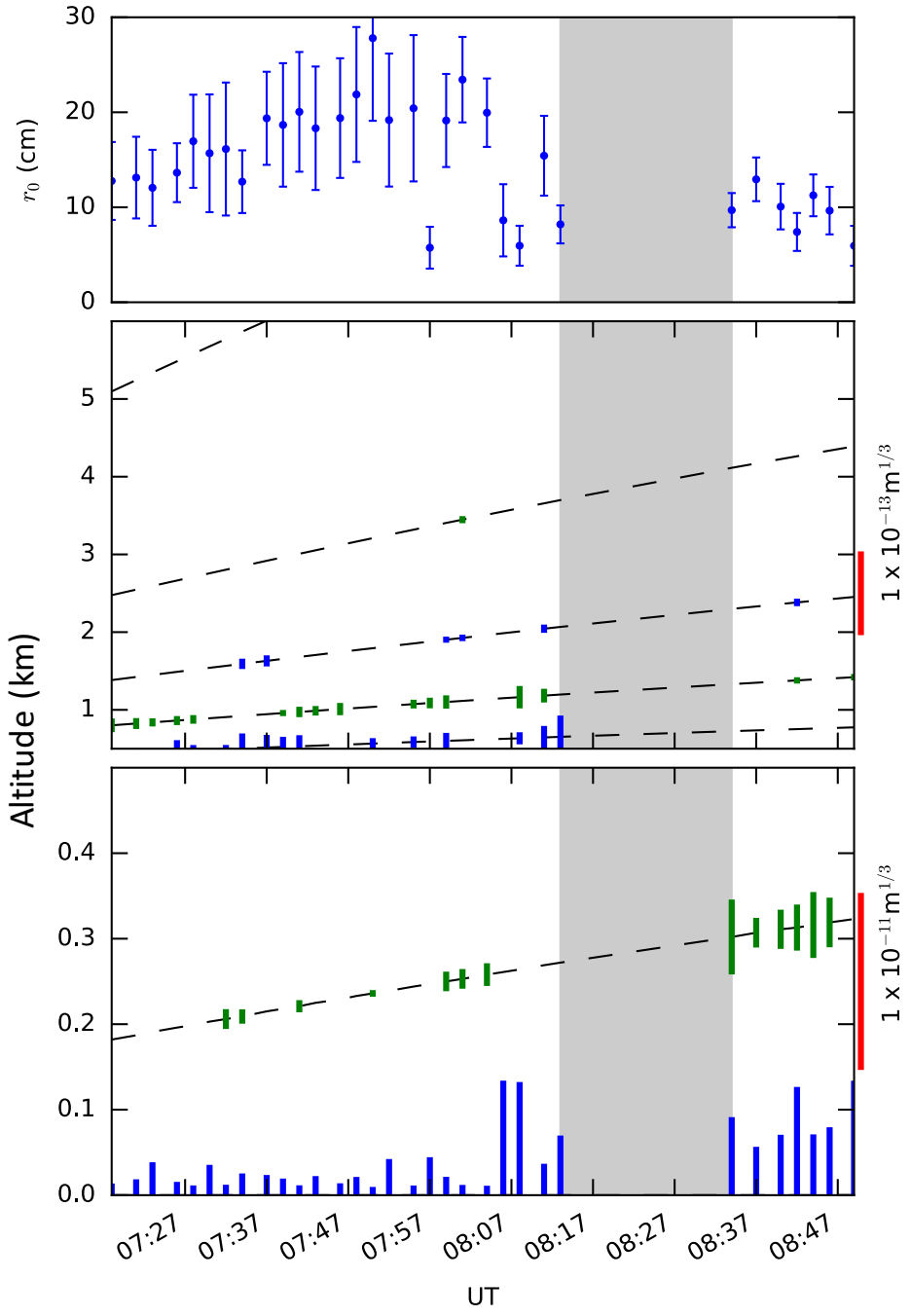

Figure 6.15: Turbulence profiles measured on the 24 April 2014 showing the turbulence profile up to 6km. The profiles show a ground layer, with some structure at low altitudes. The overall seeing conditions were good, so the ground layer is not as pronounced as some of the previous profiles. There was a region of cloud, shown in grey where there was not enough flux in the camera to measure centroids, after which the conditions only briefly improved.

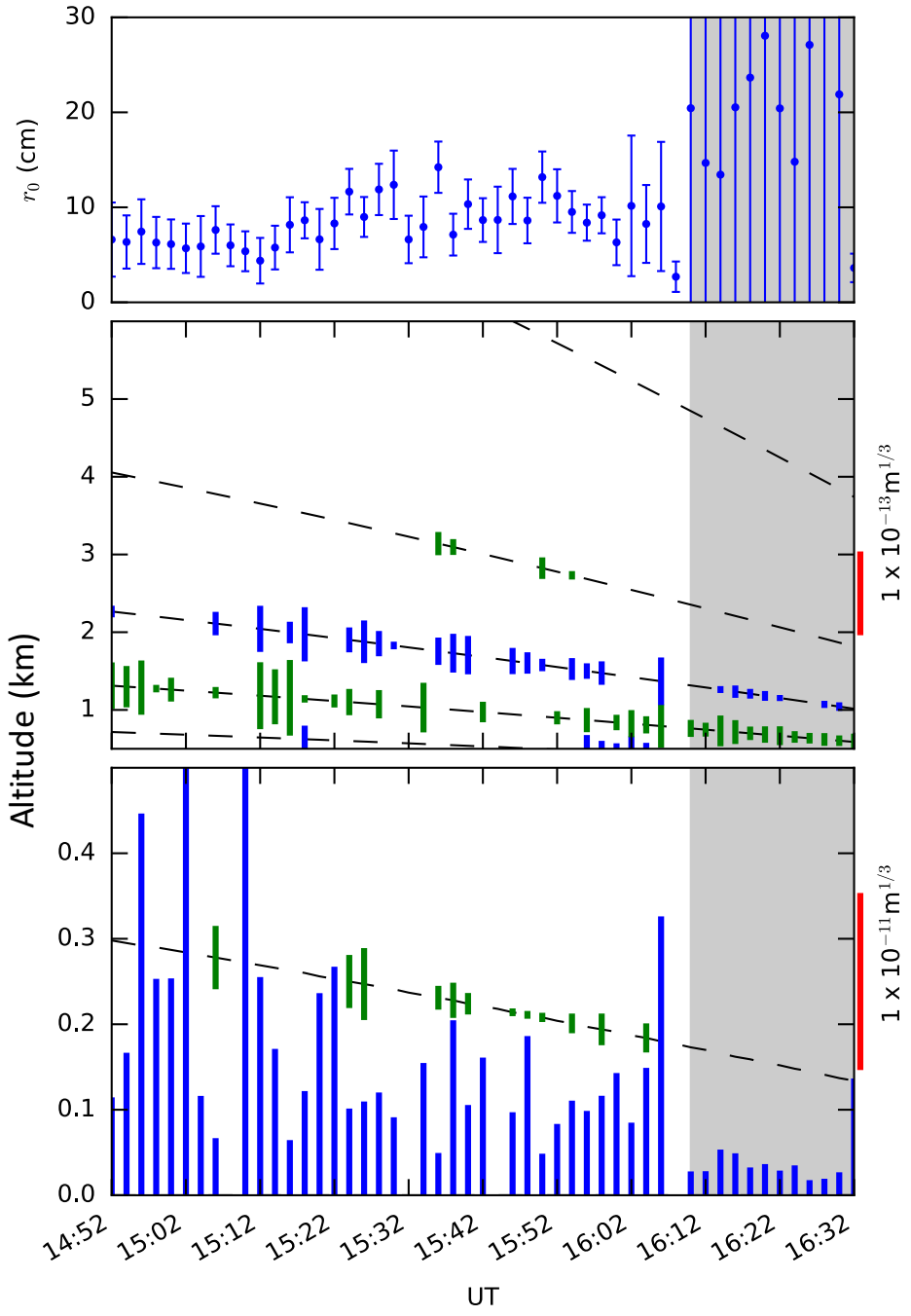

Figure 6.16: Measured turbulence profiles from 3 May 2014. The profiles are measured in the afternoon, showing a general decrease in total turbulence towards sunset. The last measurements are biased by the sun passing behind cloud. Despite the profiles being measured in the afternoon, they follow a similar structure to the morning of being dominated by the ground layer.

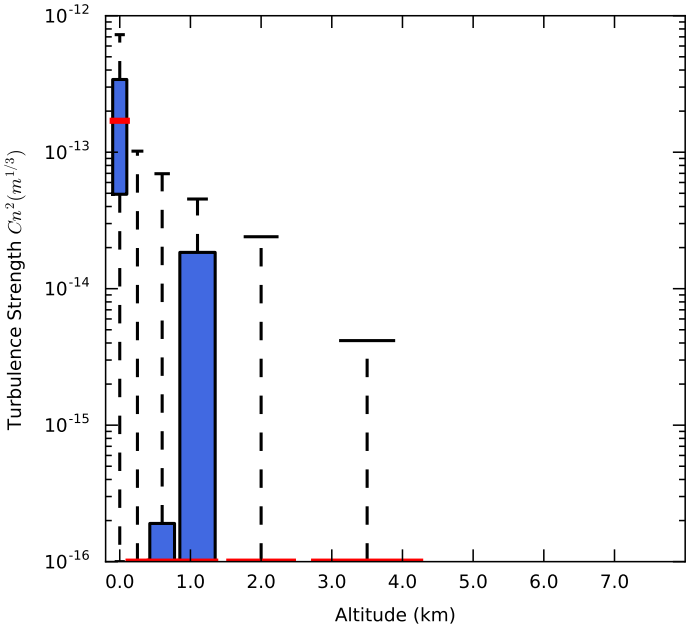

Figure 6.17: Median turbulence profile from the 23 April 2014. The red lines indicate the median strengths, while the blue boxes show the first and third quartile of the data. The bounding regions indicate the 5% and 95% of the data. Most of the turbulence is located at the ground, with some turbulence up to 1km occurring relatively frequently.

after only a minute before the system needs to pause to empty them. This means that the data is not continuous and so cannot be analysed as such to measure the evolution of the profile. Instead only individual snapshots of the turbulence profile are measured.

6.7 Future Work

The turbulence profiles shown so far are the first to be calculated using the So-SLODAR technique. In order to measure the statistics of the turbulence above La Palma during the day much more data is required. Therefore it would be of interest to automate the data acquisition and reduction such that the instrument could autonomously measure the turbulence profile whenever the SST is in operation.

The method of choosing the altitude resolution of the So-SLODAR shown here

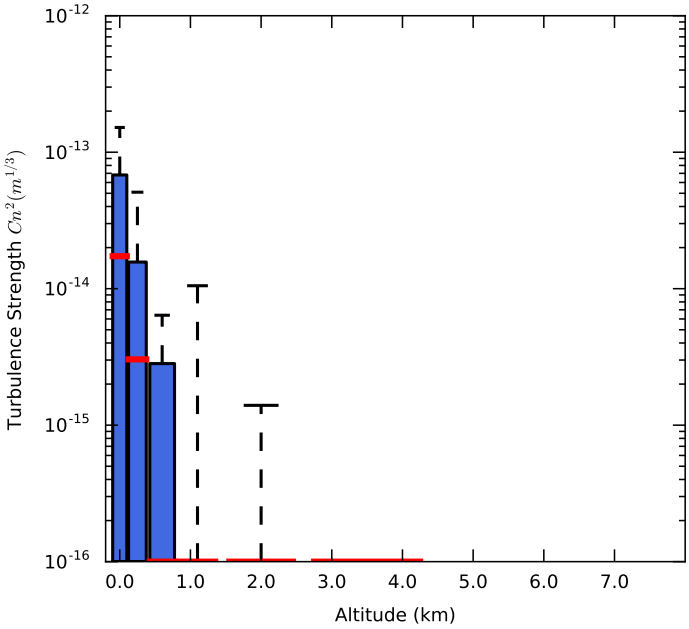

Figure 6.18: Median turbulence profile from the 24 April 2014. The red lines indicate the median strengths, while the blue boxes show the first and third quartile of the data. The bounding regions indicate the 5% and 95% of the data. Most of the turbulence is located at the ground, with the strength decaying until there is a low probability of there being any turbulence above 1km.

is based on creating response functions which have a similar orthogonality to SLODAR response functions. Another method which could be used is the S-DIMM+ method, where the response functions are chosen from minimising the noise influence on the minimisation matrix used in the least squares fitting. This could generate a set of response functions with higher altitude resolution than is currently employed by the So-SLODAR.

So far the turbulence profiles have been calculated only comparing WFS frames taken at the same time. Temporal statistics, such as τ_0 can be calculated by comparing the correlations of WFS centroids taken at different times. This could be implemented on a So-SLODAR in the same way that it is done for SLODAR (Butterley et al., 2006).

Another modification that could be made is the implementation of the methods presented in Chapters 4 and 5 into the centroiders used for So-SLODAR, as so far

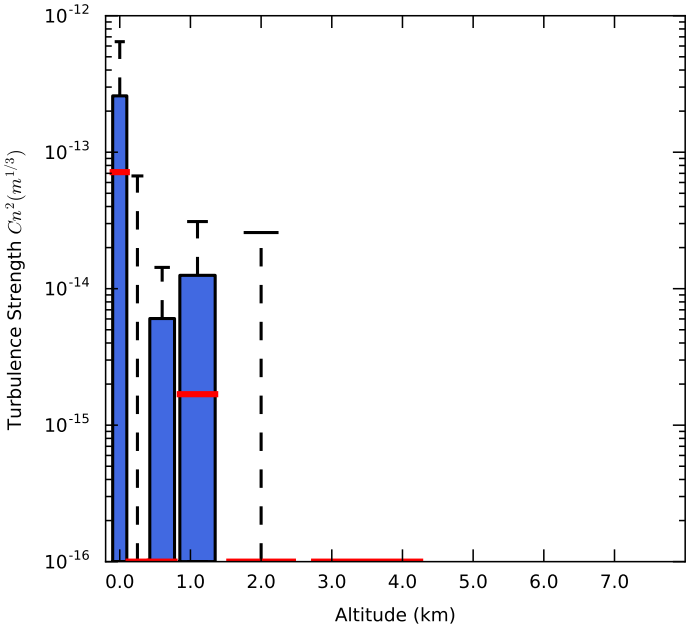

Figure 6.19: Median turbulence profile from the 3 May 2014. The red lines indicate the median strengths, while the blue boxes show the first and third quartile of the data. The bounding regions indicate the 5% and 95% of the data. Here we see a strong ground layer, with a relatively strong layer at $\sim$ 1km. This differs slightly from the previous profiles, but is expected as the profiles were taken during the afternoon before sunset rather than in the morning.

only the 2nd order polynomial fitting technique has been used for estimating the centroids from the WF-WFS.

6.8 Summary

In this chapter I have described how the SLODAR method (Wilson, 2002; Butterley et al., 2006) can be modified for use with a WF-WFS observing The Sun. The modifications made to the data analysis is similar to those made for the S-DIMM+ (Scharmer and van Werkhoven, 2010), with the inclusion of an expanding pupil to account for the effect of using an extended FOV. The choice of altitude resolution was calculated by choosing correlations between the response functions which match the correlation of the response functions in a normal SLODAR system.

A WF-WFS used on the SST in La Palma is described and the results from using the

So-SLODAR technique on the WF-WFS data are shown. The turbulence profiles shown are the first measured using this technique and show similar structure to previous turbulence observed at the SST using the S-DIMM+.

So-SLODAR is still in early development and still has a number of features which could be implemented with it. I mention some of the work that could be done in the future in order to upgrade the system, from upgrading the methods used to estimate the centroids to implementing methods for measuring the temporal statistics of the atmosphere.

Chapter 7

Conclusions

The aim of this work was to measure the turbulence profile of day-time conditions on La Palma and develop centroiding techniques for correlation WFSs. Day-time turbulence profiles are required for measuring the turbulence for solar MCAO systems and potentially estimation of conditions for night-time astronomy. I developed a method for estimating the turbulence profile using a WF-WFS, So-SLODAR, which can be used to measure the turbulence profile during the day and utilise the advantages of guide source availability on the solar surface. In order to measure turbulence profiles accurate centroids are required for multiple field directions in a WFS. This motivated the development of centroiding techniques for extended objects, both optimising centroiding parameters for estimating the location of a cross-correlation peak and developing a technique to increase the accuracy of centroids for images with large relative shifts.

7.1 Optimal Center of Mass on Cross-Correlation Images

When estimating the centroid from a cross-correlation image the optimal choice of centroiding parameters is not known. There are centroiding methods which have no free parameters, such as the 2nd order polynomial fit, and so don't suffer

from an optimisation problem. However, these methods don't measure the centroid accurately in all conditions.

By using multiple reference images to compare centroid estimates for a sub-aperture and using the spread of those estimates as a measure of the error on the centroid it is possible to estimate the performance of a given set of centroiding parameters. Using this estimator of the performance of a set of centroiding parameters it is then possible to explore a centroiders parameter space and to choose the optimal set of parameters. The computational effort required to perform this task is kept to a minimum through the use of the same cross-correlation images for testing each set of centroid parameters. This allows us to use one set of cross-correlation images for each different reference image, rather than generate new cross-correlation images for each set of centroiding parameters.

This method was demonstrated for a center of mass algorithm which utilised a window and threshold to minimise the influence of noise in the centroid calculation. However, this is not the only centroiding technique to which this method of error estimation can be applied. It would be of interest to apply this method to other centroiding techniques and estimate their optimal centroiding parameters for given scenarios. Also, in the era of E-ELTs many LGS WFSs observe extremely elongated laser spots. This technique can be applied to each sub-aperture in a WFS individually, allowing for different centroid parameters for each sub-aperture, each of which is optimised for the particular elongation seen in that sub-aperture.

7.2 Supersized Reference Images for Correlating Wavefront Sensors

For WFSs operating in open-loop systems non-common image noise can become the dominant source of error in high SNR regimes. This can be negated through the use of a larger reference image which contains the structure surrounding the mean FOV position of a sub-aperture window.

Creating a supersized reference image which contains structure around the mean position of the sub-aperture can be done using a time series of WFS images. The motion of the field within the sub-aperture in each frame can be measured using centroiding techniques for extended objects and the set of images can then be aligned and averaged. The size of the image created will be larger than the individual sub-aperture images, as the movement of the sub-aperture FOV allows the sub-aperture to sample a larger field over time than it observes in any given frame. Averaging multiple sub-aperture images also has the effect of reducing noise on the generated image.

This method may need to be applied multiple times in order to generate accurate centroid estimates for sub-apertures with large relative shifts. If this is the case a least squares centroiding method can be applied to a set of sub-aperture images to estimate the initial image shifts for a set of sub-aperture images. This is a computationally heavy centroiding technique, however it is only required to generate an initial set of centroids, for creating the initial supersized reference image.

The generated supersized reference image can then be used for centroiding where the shifts of the sub-apertures is relatively large. This increases the regime in which a correlating WFS can accurately measure centroids, which increases their viability for use in open-loop systems where the expected magnitude of centroids is large. The technique relies on a least squares centroid estimate providing accurate centroids in order to estimate initial shifts. For very large shifts between sub-aperture images if the least squares method cannot estimate centroids the technique will be unable to estimate shifts and fail to generate a supersized reference image.

7.3 Solar SLODAR

The turbulence profile at night can be well characterised by a number of different instruments, including SLODAR and Stereo-SCIDAR. However, turbulence profile during the day-time is less known, with fewer instruments available (SHABAR and

S-DIMM+). I have described a method for estimating the turbulence profile during the day, named So-SLODAR, which uses a WF-WFS observing solar granulation to estimate the day-time turbulence profile. This differs from the existing centroid based day-time turbulence profiling method, S-DIMM+, by using a modified version of the SLODAR analysis. The modifications are required as the solar disk is a continuous extended source.

Using an extended source for centroiding means the pupil size is not fixed with respect to altitude. Instead the pupil appears to expand as altitude increases, as the different field directions diverge. This effect is taken into account by modifying the pupil function in the SLODAR analysis to also be a function of altitude.

The availability of guide sources is much greater for solar observations than night-time observations. This lead to further development of the SLODAR technique to allow for multiple field separations to be used to measure the turbulence profile. This adds an extra dimension to the response functions and measured covariances from the So-SLODAR, which changes the choice of altitude resolution. A new method of estimating the altitude resolution for So-SLODAR is shown, which utilises the correlation between response functions to choose a set of altitude bins which are sufficiently orthogonal.

The day-time profiles measured are important for a number of different applications. The most obvious is for the EST, which will employ a MCAO system (Collados et al., 2013). The day-time turbulence profiles are also of potential interest to night-time astronomy for estimating the expected distribution of turbulence, however, this comparison is yet to be conducted.

Bibliography

D. S. Acton and R. C. Smithson. Solar imaging with a segmented adaptive mirror. *Applied Optics*, 31(16):3161–3169, jun 1992.

A. Agabi, J. Borgnino, F. Martin, A. Tokovinin, and A. Ziad. G.S.M: A Grating Scale Monitor for atmospheric turbulence measurements. II. First measurements of the wavefront outer scale at the O.C.A. *Astronomy and Astrophysics Suppliment Series*, 109:557–562, 1995.

R. Avila, J. Vernin, and E. Masciadri. Whole atmospheric-turbulence profiling with generalized scidar. *Applied Optics*, 36:7898–7905, 1997.

H. W. Babcock. The Possibility of Compensating Astronomical Seeing. *Publications of the Astronomical Society of the Pacific*, 65(386):229–236, 1953.

J. Bahng and M. Schwarzschild. Lifetime of Solar Granules. *Astrophysical Journal*, 134:312 – 322, 1961.

A. G. Basden, R. M. Myers, and E. Gendron. Wavefront sensing with a brightest pixel selection algorithm. *Monthly Notices of the Royal Astronomical Society*, 419(2):1628–1636, 2012.

A. G. Basden, F. Chemla, N. Dipper, E. Gendron, D. Henry, T. Morris, G. Rousset, and F. Vidal. Real-time correlation reference update for astronomical adaptive optics. *Monthly Notices of the Royal Astronomical Society*, 439(1):968–976, 2014.

J. M. Beckers. Increasing the Size of the Isoplanatic Patch with Multiconjugate Adaptive Optics. In M.-H. Ulrich, editor, *European Southern Observatory Conference and Workshop Proceedings*, volume 30, page 693, 1988.

J. M. Beckers. A seeing monitor for solar and other extended object observations. *Experimental Astronomy*, pages 1–20, 2001.

J. M. Beckers, E. Leon, J. Mason, and L. Wilkins. Solar Scintillometry: Calibration of Signals and its Use for Seeing Measurements. *Solar Physics*, 176(1):23–36, 1997.

R. Benedict, J. B. Breckinridge, and D. L. Fried. Introduction. *Journal of the Optical Society of America A*, 11(1):257, jan 1994.

T. Butterley, R. W. Wilson, and M. Sarazin. Determination of the profile of atmospheric optical turbulence strength from SLODAR data. *Monthly Notics of the Royal Astronomical Society*, 369(2):835–845, jun 2006.

M. Carlsson, V. Hansteen, L. R. van der Voort, A. Fossum, E. Marthinussen, and M. Löfdahl. Swedish Solar Telescope Online Gallery. `http://www.isf.astro.su.se/gallery/`, 2003. Online; accessed 12-February-2015.

M. Collados, F. Bettonvil, L. Cavaller, I. Ermolli, B. Gelly, A. Pérez, H. Socas-Navarro, D. Soltau, R. Volkmer, and the EST team. European Solar Telescope: Progress status. *Astronomische Nachrichten*, 331(6):615–619, jun 2010.

M. Collados, F. Bettonvil, L. Cavaller, I. Ermolli, B. Gelly, A. Pérez, H. Socas-Navarro, D. Soltau, and R. Volkmer. The European Solar Telescope. *Journal of the Italian Astronomical Society*, 84:379–390, 2013.

R. Conan, O. Lardière, G. Herriot, C. Bradley, and K. Jackson. Experimental assessment of the matched filter for laser guide star wavefront sensing. *Applied Optics*, 48:1198, feb 2009.

C. E. Coulman, J. Vernin, Y. Coqueugniot, and J. L. Caccia. Outer scale of turbulence appropriate to modeling refractive-index structure profiles. *Applied Optics*, 27(1):155–160, 1988.

J.-G. Cuby, S. Morris, I. Bryson, M. Lehnert, C. Evans, T. Fusco, P. Jagourel, R. Myers, G. Rousset, H. Schnetler, J.-P. Amans, J. Allington-Smith, F. Assemat, S. Beard, F. Chemla, R. Content, N. Dipper, M. Ferrari, E. Gendron, J.-L. Gimenez, P. Hastings, Z. Hubert, E. Hugot, P. Laporte, B. Leroux, F. Madec, B. Neichel, T. Morris, E. Prieto, M. Swinbank, G. Talbot, W. Taylor, F. Vidal, S. Vivès, P. Vola, and M. Wells. Eagle: an moao fed multi-ifu in the nir on the e-elt. In *Proceedings of SPIE*, volume 7014, pages 70141K–70141K–11, 2008.

J.-G. Cuby, S. Morris, T. Fusco, M. Lehnert, P. Parr-Burman, G. Rousset, J.-P. Amans, S. Beard, I. Bryson, M. Cohen, N. Dipper, C. Evans, M. Ferrari, E. Gendron, J.-L. Gimenez, D. Gratadour, P. Hastings, Z. Hubert, E. Hugot, P. Jagourel, P. Laporte, V. Lebrun, D. Le Mignant, F. Madec, R. Myers, B. Neichel, T. Morris, C. Robert, H. Schnetler, M. Swinbank, G. Talbot, W. Taylor, F. Vidal, S. Vives, P. Vola, N. Welikala, and M. Wells. EAGLE: a MOAO fed multi-IFU NIR workhorse for E-ELT. *Proceedings of SPIE*, 7735 (Ground-based and Airborne Instrumentation for Astronomy III):77352D–1 – 77352D–15, 2010.

W. Dali Ali, A. Ziad, A. Berdja, J. Maire, J. Borgnino, M. Sarazin, G. Lombardi, J. Navarrete, H. Vazquez Ramio, M. Reyes, J. M. Delgado, J. J. Fuensalida, A. Tokovinin, and E. Bustos. Multi-instrument measurement campaign at Paranal in 2007. Characterization of the outer scale and the seeing of the surface layer. *Astronomy and Astrophysics*, 524:A73, Dec. 2010.

E. Diolaiti. MAORY : A Multi-conjugate Adaptive Optics RelaY for the E-ELT. *The Messenger*, (June):28–29, 2010.

D. F. Elmore, T. Rimmele, R. Casini, S. Hegwer, J. Kuhn, H. Lin, J. P. McMullin, K. Reardon, W. Schmidt, A. Tritschler, and F. Wöger. The Daniel K. Inouye

Solar Telescope first light instruments and critical science plan. In S. K. Ramsay, I. S. McLean, and H. Takami, editors, *Proceedings of SPIE*, volume 9147, page 914707, jul 2014.

D. E. R. En, G. Zhao, X. Zhang, J. Dou, R. Chen, and Y. Zhu. Multiple-Aperture-Based Solar Seeing Profiler. *IAU General Assembly*, 127(955):870–879, 2015.

D. L. Fried. Optical Resolution Through a Randomly Inhomogeneous Medium for Very Long and Very Short Exposures. *Journal of the Optical Society of Amerrica*, 56(10):1372, 1966.

D. L. Fried and G. E. Mevers. Evaluation of r0 for Propagation Down Through the Atmosphere. *Applied Optics*, 13(11):2620, 1974.

M. Frigo. A fast Fourier transform compiler. *ACM SIGPLAN Notices*, 34:169–180, 1999.

M. Frigo and S. G. Johnson. the Design and Implementation of FFTW3. *Southeast Conference IEEE*, 2(May 2001):234–241, 2001.

T. Fusco and A. Costille. Impact of Cn2 profile structure on wide-field AO performance. *Proceedings of SPIE*, 7736:77360J–77360J–10, 2010.

T. Fusco, G. Rousset, J.-F. Sauvage, C. Petit, J.-L. Beuzit, K. Dohlen, D. Mouillet, J. Charton, M. Nicolle, M. Kasper, P. Baudoz, and P. Puget. High-order adaptive optics requirements for direct detection of extrasolar planets: Application to the SPHERE instrument. *Optics Express*, 14(17):7515–34, 2006.

G. Galilei. *Dialogo sopra i due massimi sistemi del mondo.* 1632.

E. Gendron, F. Vidal, M. Brangier, T. Morris, Z. Hubert, a. Basden, G. Rousset, R. Myers, F. Chemla, a. Longmore, T. Butterley, N. Dipper, C. Dunlop, D. Geng, D. Gratadour, D. Henry, P. Laporte, N. Looker, D. Perret, a. Sevin, G. Talbot, and E. Younger. MOAO first on-sky demonstration with CANARY. *Astronomy and Astrophysics*, 529:L2, 2011.

L. Gilles and B. Ellerbroek. Shack-Hartmann wavefront sensing with elongated sodium laser beacons: centroiding versus matched filtering. *Applied Optics*, 45: 6568–6576, sep 2006.

J. Hardy, J. Lefebvre, and C. Koliopoulos. Real-time atmospheric compensation. *Journal of the Optical Society of America*, 67(3):360, 1977.

J. W. Hardy. Solar imaging experiment. *Final Report, Feb. 1979 - Jun. 1980 Itek Corp., Lexington, MA. Opt. Syst. Div.*, 1980.

J. W. Hardy. *Adaptive optics for astronomical telescopes*. Oxford University Press, 1998.

S. B. Howell. *Handbook of CCD astronomy*, volume 5. Cambridge University Press, 2006.

J. D. Hunter. Matplotlib: A 2d graphics environment. *Computing in Science & Engineering*, 9(3):90–95, 2007.

H. Karttunen, P. Kröger, H. Oja, M. Poutanen, and K. J. Donner. *Fundamental astronomy*. Springer Science & Business Media, 2007.

M. E. Kasper, J.-L. Beuzit, C. Verinaud, N. Yaitskova, P. Baudoz, A. Boccaletti, R. G. Gratton, N. Hubin, F. Kerber, R. Roelfsema, H. M. Schmid, N. A. Thatte, K. Dohlen, M. Feldt, L. Venema, and S. Wolf. Epics: the exoplanet imager for the e-elt. In *Proceedings of SPIE*, volume 7015, pages 70151S–70151S–12, 2008.

C. U. Keller, C. Plymate, S. M. Ammons, N. S. Observatory, and N. C. Ave. Low-cost solar adaptive optics in the infrared. In *Proceedings of SPIE*, volume 4853, pages 351–359, 2003.

V. Klyatskin and V. I. Tatarskii. Statistical Therory of light propagation in a turbulent medium. *Izvestiya Vysshikh Uchebnykh Zavedenii, Radiofizika*, 15(10): 1433–1455, 1972.

A. N. Kolmogorov. The local structure of turbulence in incompressible viscous fluid for very large Reynolds numberst. *Doklady Akademii Nauk Sssr*, 30(1890): 301–305, 1941.

V. Kornilov, A. A. Tokovinin, O. Vozyakova, A. Zaitsev, N. Shatsky, S. F. Potanin, and M. S. Sarazin. MASS: a monitor of the vertical turbulence distribution. In P. L. Wizinowich and D. Bonaccini, editors, *Proceedings of SPIE*, volume 4839, pages 837–845, feb 2003.

M. Langlois, G. Moretto, and K. Richards. Solar multiconjugate adaptive optics at the Dunn Solar Telescope: preliminary results. In *Proceeding of SPIE*, pages 59–66, 2004.

O. Lardière, R. Conan, C. Bradley, K. Jackson, and P. Hampton. Radial thresholding to mitigate laser guide star aberrations on centre-of-gravity-based Shack-Hartmann wavefront sensors. *Monthly Notices of the Royal Astronomical Society*, 398(3):1461–1467, 2009.

M. G. Löfdahl. Evaluation of image-shift measurement algorithms for solar Shack-Hartmann wavefront sensors. *Astronomy and Astrophysics*, 524:A90, Nov. 2010.

M. G. Löfdahl and G. B. Scharmer. Sources of straylight in the post-focus imaging instrumentation of the Swedish 1-m Solar Telescope. *Astronony and Astrophysics*, 537:A80, 2012.

M. L. Louarn, N. Hubin, M. Sarazin, and A. Tokovinin. New challenges for Adaptive Optics: Extremely Large Telescopes. *Monthly Notices of the Royal Astronomical Society*, 11(February):11, 2000.

O. V. D. Lühe. A study of a correlation tracking method to improve imaging quality of ground-based solar telescopes. *Astronomy and Astrophysics*, 1983.

V. P. Lukin, E. V. Nosov, and B. V. Fortes. The Efficient Outer Scale of Atmospheric Turbulence. In *European Southern Observatory Conference and Workshop Proceedings*, volume 56, page 619, 1999.

E. Masciadri, J. Stoesz, S. Hagelin, and F. Lascaux. Optical turbulence vertical distribution with standard and high resolution at Mt Graham. *Monthly Notices of the Royal Astronomical Society*, 404(1):144–158, jan 2010.

A. McPherson, J. Spyromilio, M. Kissler-Patig, S. Ramsay, E. Brunetto, P. Dierickx, and M. Cassali. E-ELT update of project and effect of change to 39m design. In *Proceedings of SPIE*, volume 8444, page 84441F, 2012.

V. Michau, G. Rousset, and J. Fontanella. Wavefront Sensing of Extended sources. In *Real Time Post Facto Solar Image Correction, Proceedings of the 13th National Solar Observatory/Sacramento Peak Summer Workshop*, pages 124—-8, 1993.

V. Michau, J.-M. Conan, T. Fusco, M. Nicolle, C. Robert, M.-T. Velluet, and E. Piganeau. Shack-Hartmann wavefront sensing with extended sources. In *Proceedings of SPIE*, volume 6303, pages 63030B–63030B–11, 2006.

N. Miura, a. Oh-ishi, S. Shionoya, K. Watanabe, S. Kuwamura, N. Baba, S. Ueno, and K. Ichimoto. Solar scintillation detection and ranging (SCIDAR) technique for measuring turbulent-layer heights. *Monthly Notices of the Royal Astronomical Society*, 434(2):1205–1219, 2013.

B. Neichel, F. Rigaut, F. Vidal, M. A. van Dam, V. Garrel, E. R. Carrasco, P. Pessev, C. Winge, M. Boccas, C. D'Orgeville, G. Arriagada, A. Serio, V. Fesquet, W. N. Rambold, J. Lührs, C. Moreno, G. Gausachs, R. L. Galvez, V. Montes, T. B. Vucina, E. Marin, C. Urrutia, A. Lopez, S. J. Diggs, C. Marchant, A. W. Ebbers, C. Trujillo, M. Bec, G. Trancho, P. McGregor, P. J. Young, F. Colazo, and M. L. Edwards. Gemini multiconjugate adaptive optics system review-II. Commissioning, operation and overall performance. *Monthly Notices of the Royal Astronomical Society*, 440(2):1002–1019, 2014.

I. Newton. *Opticks: Or a Treatise of the Reflections, Refractions & Colours of Light*. Dover Publications, 1730.

L. J. November and G. W. Simon. Precise Proper Motion Measurement of Solar Granulation. *Astrophysical Journal*, 333(1):427–442, oct 1988.

J. Osborn, R. W. Wilson, T. Butterley, R. Avila, V. S. Dhillon, T. J. Morris, and H. W. Shepherd. Stereo Scidar : Profiling Atmospheric Optical Turbulence With Improved Altitude Resolution. In *Third AO4ELT Conference - Adaptive Optics for Extremely Large Telescopes*, May 2013.

B. Pan, G.-q. Yang, and Y. Liu. Study on optimization threshold of centroid algorithm. *Optics and Precision Engineering*, 16, 2008.

T. Pfrommer and P. Hickson. High resolution mesospheric sodium properties for adaptive optics applications. *Astronomy and Astrophysics*, 565:A102, 2014.

R. Ragazzoni. Pupil plane wavefront sensing with an oscillating prism. *Journal of Modern Optics*, 43(2):289–293, feb 1996.

L. Rayleigh. Xii. on the manufacture and theory of diffraction-gratings. *Philosophical Magazine Series 4*, 47(310):81–93, 1874.

O. Reynolds. On the dynamical theory of incompressible viscous fluids and the determination of the criterion. In *Proceedings of the Royal Society London*, volume 56, pages 40–45, 1894.

F. J. Rigaut, B. L. Ellerbroek, and R. Flicker. Principles, Limitations and Performance of Multi-Conjugate Adaptive Optics. In P. L. Wizinowich, editor, *Proceedings of SPIE*, volume 4007, pages 1022–1031, jul 2000.

T. R. Rimmele. Recent Advances in Solar Adaptive Optics. *Proceedings of SPIE*, 5490:34–46, oct 2004.

T. R. Rimmele and J. Marino. Solar adaptive optics. *Living Reviews of Solar Physics*, 8, 2011.

T. R. Rimmele and R. R. Radick. Solar adaptive optics at the National Solar Observatory. *Proceedings of SPIE*, 3353:72–81, 1998a.

T. R. Rimmele and R. R. Radick. Solar Adaptive Optics at the National Solar Observatory. In *Proceedings of SPIE*, volume 3353, pages 72–81, 1998b.

T. R. Rimmele, F. Woeger, J. Marino, K. Richards, S. Hegwer, T. Berkefeld, D. Soltau, D. Schmidt, and T. Waldmann. Solar multi-conjugate adaptive optics at the Dunn Solar Telescope. *Proceedings of SPIE*, 7736:773631–773631–7, jul 2010.

T. P. Robitaille, E. J. Tollerud, P. Greenfield, M. Droettboom, E. Bray, T. Aldcroft, M. Davis, A. Ginsburg, A. M. Price-Whelan, W. E. Kerzendorf, A. Conley, N. Crighton, K. Barbary, D. Muna, H. Ferguson, F. Grollier, M. M. Parikh, P. H. Nair, H. M. Günther, C. Deil, J. Woillez, S. Conseil, R. Kramer, J. E. H. Turner, L. Singer, R. Fox, B. A. Weaver, V. Zabalza, Z. I. Edwards, K. Azalee Bostroem, D. J. Burke, A. R. Casey, S. M. Crawford, N. Dencheva, J. Ely, T. Jenness, K. Labrie, P. L. Lim, F. Pierfederici, A. Pontzen, A. Ptak, B. Refsdal, M. Servillat, and O. Streicher. Astropy: A community Python package for astronomy. *Astronomy and Astrophysics*, 558:A33, 2013.

A. Rocca, F. Roddier, and J. Vernin. Detection of atmospheric turbulent layers by spatiotemporal and spatioangular correlation measurements of stellar-light scintillation. *Journal of the Optical Society of America*, 64(7):1000, 1974.

F. Roddier. The Effects of Atmospheric Turbulence in Optical Astronomy. *Progress in Optics*, 19:281–376, 1981.

F. Roddier. *Adaptive optics in astronomy*. Cambridge university press, 1999.

F. Roddier and C. Roddier. Curvature Sensing and Compensation: A New Concept in Adaptive Optics. In *Very Large Telescopes their Instrumentation, ESO Conference Workshop Proceedings*, volume 1, pages 667–973, 1988.

G. Rousset, D. Gratadour, E. Gendron, T. Buey, R. Myers, T. Morris, A. Basden, G. Talbot, D. Bonaccini Calia, E. Marchetti, and T. Pfrommer. Proposal for a

field experiment of elongated Na LGS wave-front sensing in the perspective of the E-ELT. *Proceedings of SPIE*, 9148(0):91483M, 2014.

D. Saint-Jacques. *Astronomical Seeing in Space and Time*. PhD thesis, University of Cambridge, 1998.

M. Sarazin and F. Roddier. The ESO differential image motion monitor. *Astronomy and Astrophysics*, 227:294–300, 1990.

C. D. Saunter. Quantifying subpixel accuracy: an experimental method for measuring accuracy in image-correlation-based, single-particle tracking. *Biophysical Journal*, 98(8):1566–70, Apr. 2010.

G. B. Scharmer and T. I. M. van Werkhoven. S-DIMM+ height characterization of day-time seeing using solar granulation. *Astronomy and Astrophysics*, 513:A25, apr 2010.

G. B. Scharmer, M. Shand, M. G. Löfdahl, P. M. Dettori, and W. Wei. A Workstation Based Solar / Stellar Adaptive Optics System. In *Proceedings of SPIE*, volume 4007, pages 239–250, 2000.

G. B. Scharmer, P. Dettori, M. G. Löfdahl, and M. Shand. Adaptive optics system for the new Swedish solar telescope. In *Proceedings of SPIE*, volume 4853, pages 370–380, 2002.

G. B. Scharmer, K. Bjelksjö, T. Korhonen, B. Lindberg, and B. Petterson. The 1-meter Swedish solar telescope. In *Proceedings of SPIE*, volume 4853, pages 341–350, 2003.

G. B. Scharmer, D. Kiselman, M. G. Löfdahl, and L. H. M. Rouppe van der Voort. First Results from the Swedish 1-m Solar Telescope. In J. Trujillo-Bueno and J. Sanchez Almeida, editors, *Solar Polarization*, volume 307 of *Astronomical Society of the Pacific Conference Series*, page 3, 2003.

D. Schmidt, N. Gorceix, X. Zhang, J. Marino, R. Coulter, S. Shumko, P. Goode, T. Rimmele, and T. Berkefeld. The multi-conjugate adaptive optics system of the New Solar Telescope at Big Bear Solar Observatory. In *Proceedings of SPIE*, volume 9148, page 91482U, 2014.

J. D. Schmidt. Numerical simulation of optical wave propagation with examples in matlab. SPIE Bellingham, WA, 2010.

R. V. Shack and B. Platt. Production and use of a lenticular Hartmann screen. *Journal of the Optical Society of America*, 61:656, 1971.

H. W. Shepherd, J. Osborn, R. W. Wilson, T. Butterley, R. Avila, V. S. Dhillon, and T. J. Morris. Stereo-SCIDAR: optical turbulence profiling with high sensitivity using a modified SCIDAR instrument. *Monthly Notices of the Royal Astronomical Society*, 437(4):3568–3577, nov 2014.

D. Soltau, T. Berkefeld, D. Schmidt, and O. von der Lühe. Solar adaptive optics at the Observatorio del Teide, Tenerife. In A. Comeron, E. I. Kassianov, K. Schäfer, K. Stein, and J. D. Gonglewski, editors, *Proceedings of SPIE*, volume 8890, pages 88901D–88901D–10, oct 2013.

R. Stone. A comparison of digital centering algorithms. *Astronomical Journal*, 1989.

G. I. Taylor. The Spectrum of Turbulence. In *Proceedings of the Royal Society of London A: Mathematical, Physical and Engineering Sciences*, volume 164, pages 476–490, 1938.

S. Thomas, O. Lardiere, D. Gavel, and R. Conan. Study of centroiding algorithms to optimize Shack-Hartmann WFS in the context of ELTs. *1st AO4ELT Conference - Adaptive Optics for Extremely Large Telescopes*, 05004:05004, 2010.

S. J. Thomas, S. Adkins, D. Gavel, T. Fusco, and V. Michau. Study of optimal wavefront sensing with elongated laser guide stars. *Monthly Notices of the Royal Astronomical Society*, 387:173–187, 2008a.

S. J. Thomas, S. Adkins, D. Gavel, T. Fusco, and V. Michau. Study of optimal wavefront sensing with elongated laser guide stars. *Monthly Notices of the Royal Astronomical Society*, 387(1):173–187, 2008b.

A. Tokovinin. From differential image motion to seeing. *Publications of the Astronomical Society of the Pacific*, 114(800):1156–1166, 2002.

A. Tokovinin and V. Kornilov. Accurate seeing measurements with MASS and DIMM. *Monthly Notices of the Royal Astronomical Society*, 381(3):1179–1189, 2007.

J. T. Trauger, G. E. Ballester, C. J. Burrows, S. Casertano, J. T. Clarke, D. Crisp, R. W. Evans, I. Gallagher, John S., R. E. Griffiths, J. J. Hester, J. G. Hoessel, J. A. Holtzman, J. E. Krist, J. R. Mould, P. A. Scowen, K. R. Stapelfeldt, A. M. Watson, and J. A. Westphal. The on-orbit performance of WFPC2. *Astrophysical Journal*, 435(9):L3, nov 1994.

S. Van der Walt, S. C. Colbert, and V. Gaël. The NumPy array: a structure for efficient numerical computation. *Computing in Science and Engineering*, 13: 22–30, 2011.

F. Vidal, E. Gendron, M. Brangier, A. Sevin, G. Rousset, and Z. Hubert. Tomography reconstruction using the Learn and Apply algorithm. In *1st AO4ELT Conference - Adaptive Optics for Extremely Large Telescopes*, volume 07001, page 07001, Les Ulis, France, feb 2010. EDP Sciences.

N. Vinnichenko. *Turbulence in the free atmosphere*. Springer Science & Business Media, 2013.

T. A. Waldmann, T. Berkefeld, and O. von der Lühe. Measuring turbulence height profiles using extended sources and a wide-field hartmann-shack wavefront-sensor. In *Adaptive Optics: Analysis and Methods/Computational Optical Sensing and Imaging/Information Photonics/Signal Recovery and Synthesis Topical Meetings on CD-ROM*, page PMA3. Optical Society of America, 2007.

T. a. Waldmann, T. Berkefeld, and O. von der Lühe II. Turbulence profiling using wide field of view Hartmann-Shack wavefront sensors. In *Proceedings of SPIE*, volume 7015, pages 70155O–70155O–12, 2008.

R. W. Wilson. SLODAR: measuring optical turbulence altitude with a Shack-Hartmann wavefront sensor. *Monthly Notices of the Royal Astronomical Society*, 337(1):103–108, nov 2002.

R. W. Wilson and C. R. Jenkins. Adaptive optics for astronomy: theoretical performance and limitations. *Monthly Notices of the Royal Astronomical Society*, 278(1):39–61, jan 1996.

Q. Yang, J. Zhang, K. Nozato, K. Saito, D. R. Williams, A. Roorda, and E. a. Rossi. Closed-loop optical stabilization and digital image registration in adaptive optics scanning light ophthalmoscopy. *Biomedical Optical Express*, 5(9):3174–91, 2014.

A. T. Young. Seeing: Its cause and cure. *Astrophysical Journal*, 189:587–604, 1974.

A. Ziad, R. Conan, A. Tokovinin, F. Martin, and J. Borgnino. From the grating scale monitor to the generalized seeing monitor. *Applied Optics*, 39(30):5415–5425, Oct 2000.

Colophon

This thesis was typeset with LaTeX 2$_\varepsilon$. It was created using the *memoir* package, maintained by Lars Madsen, with the *madsen* chapter style. The font used is Latin Modern, derived from fonts designed by Donald E. Kunith.